Texas A&M University
J. Mike Walker '66 Department of Mechanical Engineering
Turbomachinery Laboratory

EXPERIMENTS ON A TILTING PAD, POROUS CARBON-GRAPHITE GAS BEARING: STATIC LOAD AND FORCE COEFFICIENTS

Report to the Turbomachinery Research Consortium

TRC-B&C-03-2020

by

Luis San Andrés

Mast-Childs Chair Professor

Principal Investigator

Rachel Bolen

M.S. Student, Mechanical Engineering

TRC Project #28-258124-00138

Table of Contents

List of Tables

List of Figures

Nomenclature

A	Projected area of pad normal to flow [m^2]
a_X, a_Y	Housing accelerations along X and Y directions [m/s^2]
D_{LOP}	Equivalent housing displacement relative to rotor in line with a pad [m]
D_X, D_Y	Housing displacements relative to rotor along X and Y directions [m]
d	Bearing bore diameter (nominal) [mm]
e	Eccentricity of bearing housing with respect to rotor geometric center [m]
F_a	Aerostatic load capacity (no shaft speed) [N]
F_{LOP}	Equivalent force on a pad [N]
F_P	Preload force from pivot on pad, set during bearing assembly [N]
F_X, F_Y	Forces applied along X and Y directions [N]
F_S	Static force [N]
F_t	Reaction force from bearing [N]
g	ratio of imaginary part to real part of dynamic stiffness
H	Complex dynamic stiffness (average) [MN/m]
h	Complex dynamic stiffness, one set of measurements [MN/m]
h_0	Cone height, single Belleville washer [mm]
K	Stiffness coefficient [MN/m]
K_a	Aerostatic stiffness of bearing while supplied with pressurized air and no shaft speed [MN/m]
K_b	Baseline stiffness from static load tests [MN/m]
K_F	Equivalent stiffness due to gas film at each pad location [MN/m]
K_P	Stiffness of pivot in contact with two Belleville washers [MN/m]
K_{SP}	Belleville washer stiffness [MN/m]
K_S	Stiffness of bearing operating with supply air and gas film from measurements of static load and bearing eccentricity while operating with shaft speed [MN/m]
K_U	Stiffness of assembled bearing structure, arrow designates load or unload condition [MN/m]
L	Bearing axial length [mm]
M	Baseline mass [kg]
M_B	Bearing mass [kg[
M_P	Pad mass [kg]
N	Number of pads
n	Number of samples
n_s	Number of sets used to calculate average complex dynamic stiffness
P_a	Ambient pressure [Pa]
P_S	Pressure of air supplied to a pad [Pa]
Q	Average flowrate [m^3/s]
Q_S	Flow into pad [m^3/s]
Q_2	Flow exiting pad [m^3/s]
R	Journal radius [m]
R_{PAD}	Pad radius [m]

S_1	Tilt displacement near pad leading edge [mm]
S_2	Tilt displacement near pad trailing edge [mm]
T	Pad temperature [℃]
T_a	Ambient Temperature [℃]
t	Belleville washer material thickness [mm]
t_p	Porous restrictor equivalent thickness [m]
t_R	Maximum thickness of porous layer [m]
U_C	Total uncertainty of bearing damping coefficient [kN·s/m]
U_K	Total uncertainty of bearing stiffness coefficient [MN/m]
w	Pad width [mm]
α_R	Coefficient of thermal expansion for rotor [m/(m·℃)]
α_P	Coefficient of thermal expansion for porous carbon pad [m/(m·℃)]
β	Bias error
Γ	Precision error
δ	Pad tilt angle [^{0}]
Θ_P	Pad arc length [rad]
κ	Permeability coefficient of porous pad material [m^2]
η	$F/((P_s-P_a)L\cdot d)$, Ratio of actual load capacity to predicted load capacity
μ	Gas viscosity, absolute [N·s/m^2]
μ_S	Viscosity of gas at supply condition [N·s/m^2]
φ	Attitude angle between bearing eccentricity vector and static load vector [^{0}]
ω	Excitation frequency [rad/s]
Ω	Operating shaft speed [1/s]
⬆	Increasing static load condition
⬇	Decreasing static load condition

ABBREVIATIONS

BW	Belleville washer (disc spring)
ECS	Eddy current sensor
ID	Inner diameter
Im	Imaginary component
LBP	Load between pad orientation
LOP	Load on pad orientation
LPM	Liters per Minute
OD	Outer diameter
PGB	Porous gas bearing
Re	Real component
RBS	Rotor bearing system(s)
TPJB	Tilting pad journal bearing
VI	Virtual instrument
VFD	Variable frequency drive

Abstract

Hydrostatic gas journal bearings with porous tilting pads enable shaft support with minute drag power losses. Yet, there is little archival information on the static and dynamic load performance of this bearing type. Thus, the report characterizes the static and dynamic load performance of a gas journal bearing (diameter D = 101.6 mm) with four porous Carbon-Graphite tilting pads, each L=76 mm in length. Each pad is supported by two nested Belleville washers (BW) acting on spherical pivots. First, experiments characterize the stiffness from the washers as a pivot support with K_P=20.6 MN/m during loading and 9.3 MN/m during unloading. Dry friction at the pivot-washer interface causes the difference in stiffness.

With the bearing installed in an existing high-speed facility, measurements from static load tests include bearing eccentricity and attitude angle, pad temperatures and pad tilt displacements. As the air supply pressure into the bearing pads increases, so does the bearing hydrostatic specific load capacity that equals 58% of the pressure difference (supply-ambient). Upon operation with shaft speed, and to avoid contact, there is a significant decrease in load capacity to ~43% of the hydrostatic load. Supplied with air at 7.8 bara, the bearing supported static loads up to ~172 kPa (300 lb_f) at 6 krpm (36 m/s) and ~117 kPa (203 lb_f) at 9 krpm (48 m/s). At ambient temperature 31°C -41°C, the bearing static stiffness K_S ~13.1 MN/m (75 klb_f/in) and independent of either shaft speed or static load.

Results of dynamic load tests acting on the bearing during operation with shaft speed at 6 krpm and 9 krpm, and for specific static loads up to 115 kPa and 101 kPa respectively, show frequency-independent stiffness and damping coefficients (K, C) model best the bearing dynamic forced response. Bearing stiffnesses (K_{XX} ~ K_{YY}) increase with static load and range from 13.6

MN/m to 32.7 MN/m (186 klb$_f$/in). The bearing damping coefficients (C_{XX} ~C_{YY}) are as large as 5.8 kN·s/m (34 lb$_f$·s/in), though with a large experimental uncertainty.

Introduction

The use of gas as a lubricant in a fluid film bearing requires consideration of the gas properties and lubrication type. Advantages of gas as a lubricant include no process fluid contamination, low power losses due to lubricant shear, and low-cost material (compressed air) with an ample supply. Since gases have a lower viscosity and density than more conventional lubricants (e.g. oil or water), gas film bearings require of minute radial clearances, typically 5 μm-20 μm, between the rotor and pad or bushing surface to support loads with an adequate stiffness [1]. The lubrication type, hydrodynamic, hydrostatic or hybrid, must also be considered, as it affects the bearing performance characteristics (e.g. load capacity, stiffness, etc.), ancillary equipment requirements (e.g. supply gas system), and the rotor system start-up and shut-down procedures. Hydrodynamic lubrication requires relative motion of surfaces to create a pressure field in a fluid film. Hydrostatic lubrication uses a restrictor, located between a supply of externally pressurized gas and the bearing inner diameter (ID), to push fluid into the film. Hydrostatic lubrication does not require motion of the surfaces to generate a pressure in the film. A hybrid bearing uses hydrostatic lubrication at low shaft speeds to prevent rotor-bearing contact and becomes a hydrodynamic bearing above a threshold shaft speed.

The restrictor in a porous gas bearing (PGB) is a layer of permeable material, often making the bushing wall or the pad. The permeability coefficient (κ) quantifies the resistance of the porous material to fluid flow. Many analytical studies, albeit mostly for porous bushings, provide design information (e.g. stiffness, load capacity, flow consumption) for a range of feeding parameters[1]

[1]A feed parameter in a porous gas bearing = $12\kappa R^2/(c^3 t_p)$ where the restrictor permeability is (κ), journal radius (R), bearing radial clearance (c), and restrictor thickness (t_p). The parameter compares the resistance to flow in the porous layer to that through the film land [2].

[2-5]. Obtaining PGB performance predictions requires knowledge of κ, often empirically determined. Magnitudes of κ for PGBs range from 10^{-14} m^2 to 10^{-15} m^2 [6, 7].

In a numerical study, Fourka and Bonis [6] compared gas bearings with porous surfaces to those with orifice type restrictors and showed a porous restrictor (with $\kappa \approx 10^{-14}$ m^2 and a film thickness of 12 μm) increases the bearing load capacity by 34% while doubling the bearing centering stiffness. However, Fourka and Bonis also found the PGB consumes more gas, and thus requires a larger source of pressurized gas. The comparison to orifice type restrictors indicated that a porous surface restrictor can increase the bearing stiffness.

The manufacturing industry developed PGBs to increase the support stiffness of precision machine spindles in order to reduce runout of the cutting tool. This application advanced PGBs for operation at moderate (e.g. 20.3 m/s [7]) surface speeds. Among the many lessons learned, Rasnick et al. [7] noted that a consistent pad permeability was essential for PGB operation without pneumatic hammer instability[2] at a static load (F) of 2224 N. Defining a specific load as load (F) divided by the projected area ($A=L\cdot d$, with bearing bore diameter (d) and axial length (L)), the corresponding specific load is ~58 kPa. Ref. [7] also described a simple procedure for verifying a uniform flow over the bearing pad surface and a procedure to adjust the local material permeability to avoid pneumatic hammer instability.

Research on porous pad-type gas lubricated journal bearings also extended to develop oil-free turbomachinery. In 1975, Shapiro et. al. [9] published the first experimental study on

[2] The pneumatic hammer instability arises in poorly designed hydrostatic bearings and is a phenomenon driven by a volume of lubricant trapped in a pocket that excites rotor vibrations at a natural frequency. The instability occurs when a change in gas film pressure lags a rapid change in film thickness (e.g. due to a load increment) [8]. Pneumatic hammer instability is uncommon to porous gas bearings because the micron-sized pores (small volume) do not trap significant amounts of lubricant gas.

elastically supported, tilting-pad PGBs for turbomachinery. Neither analytical nor numerical studies of porous tilting-pad bearings existed at the time to guide their design. Consequently, the authors used design curves generated from analytical results for fixed geometry, porous surface bushings. The lack of predictions for a segmented PGB design and the uncertainty in the estimated κ of their porous material motivated their experimental work. A three-pad PGB design for application into a cryogenic turboexpander, had a nominal bore diameter (d) of 12.7 mm and an axial length-to-bore diameter ratio (L/d) of 1. The bearing featured Belleville washers (BW) as spring supports with a stiffness of 175 kN/m. The bearing pads received 3.4 bara air at ~28 LPM, the rotor operated at a maximum speed of 65 krpm (surface speed $\Omega \times R \approx 43$ m/s), and the specific load on each bearing increased to a maximum load of 21 kPa. During operation, the maximum power loss was 20.5 W, and the rotor whirled with an amplitude of only a few microns [9]. Although the authors originally overestimated the porous pad thickness, drilling holes (diameter≈1.02 mm) in the pads sufficiently increased κ to demonstrate porous gas TPJB operation for a turbomachine with both load and speed.

The following experimental works on pad-type PGBs for turbomachine-type rotor-bearing systems (RBS) focused on measuring the bearing response to rotor imbalance. Devitt et. al [10] built a RBS with two five-pad PGBs spanning 2 m, a rotor (OD=100 mm, weight=3.12 kN) and squeeze film dampers. The RBS, when subjected to large imbalance forces (ranging 29-114% the rotor weight), survived a 23X amplification factor while crossing the first critical speed, but failed before reaching 10 krpm due to insufficient damping [10]. (API 2.6.1.2 categorizes amplification factors exceeding 2.5X as concerning for machine health, but note that the test bearings were prototypes, not commercial bearings [11]). System level tests by San Andrés et al. [12] reached higher operating speeds, up to 55 krpm, with a small, lightly loaded RBS (28.5 mm rotor OD),

subjected only to residual rotor imbalance and featuring 3-pad PGBs (72.5 kPa/bearing) with elastic supports. Ref. [12] reported the synchronous rotor response increased in amplitude with supply pressure, the drag coefficients were small for supply pressures ranging 5.1 to 7.8 bar and no subsynchronous responses. The studies above demonstrated that lightly loaded, segmented PGBs can sustain forces from small mass imbalances and that the gas bearings provided little viscous damping to the rotor bearing systems.

Zheng et al. [13] continued experiments on a RBS supported on two pad type PGBs to determine the system response to added imbalance masses. The RBS (100 mm rotor OD, 285 N rotor weight) was heavier than that in [12] and featured two five-pad PGBs with Belleville washer supports with pivot stiffness, $K_P \approx$14-19 MN/m [14]. The authors found that the measured amplitude of the rotor synchronous response was proportional to the applied imbalance mass (~186 g·mm, ~227 g·mm or ~373 g·mm) for shaft speeds up to 8 krpm (~42 m/s surface speed), yet large resonances at the first critical speed (~9 krpm) prevented further tests at higher rotating speeds [13]. Reference [14] noted that the added masses offset the rotor mass center more than that allowed for an ISO G2.5 grade balance (~19.2 g·mm for the test rotor). In addition, Zheng et al. found the supply air flowrate to the pads increased with supply pressure and attributed differences in pad flowrates to differences in surface wear [13]. Zheng et al. also estimated a permeability coefficient ($\kappa \approx 2.85 \times 10^{-15}$ m^2) for the test bearing porous pads from measurements of mass flowrate and supply pressure into the five pads [14].

Using the permeability coefficient (κ) in Ref. [14] and the five-pad PGB geometry in Refs. [13, 14], Feng et al. [15] developed a computational model of pad-type PGBs and predicted stiffness and damping coefficients over a range of excitation frequencies. For shaft speeds up to 20 krpm, the model predicted (synchronous shaft speed) direct stiffness coefficients and direct

damping coefficients. A steady-state analysis found that for a porous pad-type, hydrostatic gas bearing, the pressure distribution over a pad distorts and reduces with shaft speed. The pressure field distortion indicates a weakly supported leading edge and a reduced load capacity [15]. In a hydrostatic, porous surface, gas-lubricated bushing, the rotor drags externally pressurized air into a converging clearance, whereas in a pad-type bearing, the pressure of the air dragged into the leading edge is just atmospheric. The reduction in air film pressure under the leading edge of a pad (relative to the rest of the pad face) causes the leading edge of the pad to tilt towards the rotor and to induce pad-rotor contact. The model shows that hydrodynamic effects degrade the performance of segmented, hydrostatic PGBs. However, the literature lacks experimentally determined pad-type PGB force coefficients to validate the conclusions in Ref. [15]. Moreover, the predictions do not detail gas bearing dynamic performance for subsynchronous frequencies.

This report quantifies via experiments the static and dynamic load performance of a hydrostatic gas journal bearing with four porous-surface tilting pads supported on Belleville washers. Tasks accomplished are below.

Description of Tasks Completed

The measurements reported herein relate to two test rigs. Experiments to identify Belleville washer stiffness (Chapter 1) use Rig 1. Experiments involving the assembled bearing (Chapters 2-5) use Rig 2. Deliverables from measurements made with Rig 2 include bearing load capacity, dynamic force coefficients, and pad temperatures.

The tasks to quantify the static and dynamic load performance of the test bearing include the following:

1. Determine the stiffness (K_P) of the pad supports (i.e. the pivot assembly stiffness) from measurements of applied load and corresponding displacement. See Chapter 1.
2. Measure applied load and bearing housing displacement, with and without a gas film, and without shaft speed to estimate the bearing structural stiffness (K_U) and to assess the effect of supply air on the bearing structural stiffness. See Chapters 2-3.
3. For a range of applied static loads, measure pad temperatures and pad vibration during operation with shaft speed (6 krpm, 9 krpm). Note the bearing load capacity as the load causing a sudden increase in pad temperatures (indication of pad-rotor contact). Determine bearing attitude angle and bearing eccentricity. Estimate bearing static stiffness (K_S) from measurements. Chapter 4 discusses the results of this task.
4. For operation at two shaft speeds, excite bearing with dynamic loads along two orthogonal directions to assess cross-coupling forces (if significant) and to estimate the bearing dynamic force coefficients. Use information from Tasks 1 and 2 to interpret the results. Chapter 5 discusses the outcome of this task.

Test Bearing Description

Table 1 lists the test bearing geometry, and Figure 1 shows a photograph of the bearing featuring four, porous carbon-graphite, tilting-type pads with elastic pivot supports consisting of two nested Belleville washers. The nominal bearing bore diameter (d) is 101.6 mm. Each pad, 74^o in arc length, has an axial length equal to 76.2 mm (L/d = 0.75). The pivot locates midway along the pad arc; hence, its offset is 50%. The total mass of the bearing (M_B), including housing, pads, pivots and washers, is 20$\pm$0.2 kg. The mass of each pad (M_P) is 0.8 kg.

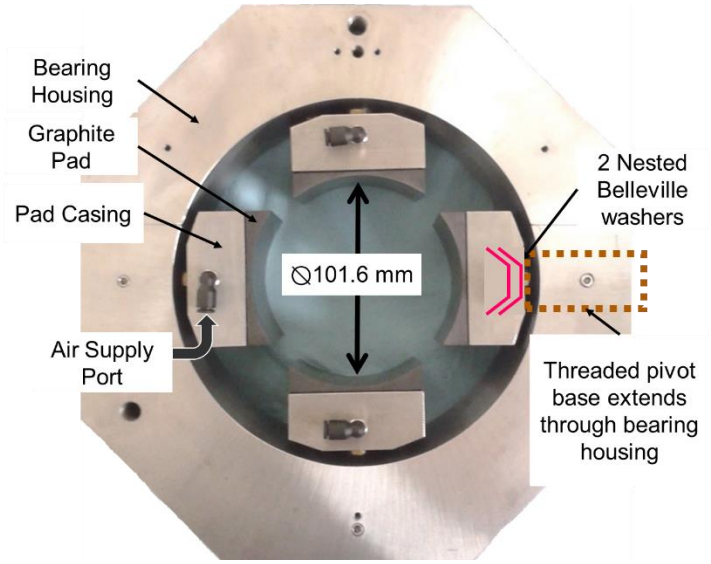

Figure 1: Photograph of bearing with porous carbon-graphite pads and schematic overlay view showing pivot-washer pad support

The split bearing housing assembles with four capscrews. On assembly, the pads rest against the rotor (101.59$\pm$0.003 mm diameter). The pads have no geometric pad preload, and they lift from the rotor when adequately supplied with pressurized air.

Table 1: Dimensions and physical properties of shaft, bearing housing, porous carbon-graphite pads, pad supports, and air.

ROTOR	Shaft Diameter	101.59 mm
	Shaft Material	AISI 4140
	Shaft Surface Finish	0.4 μm
	Thermal Expansion Coefficient, α_R [16]	12.2 μm/(m·°C)
BEARING	Nominal Bore Diameter, d	101.60 mm
	Number of Pads, N	4
	Mass of Housing, Pads and Pivots	20±0.2 kg
PAD	Pad Mass	0.82 kg
	Pad Axial Length, L	76.2 mm
	Pad Arc Length	74^0
	Pivot Offset	50%
	Pad Width	61 mm
	Pad Radius	50.4 mm
	Maximum Thickness of Porous Layer, t_R	15.24 mm
	Thermal Expansion Coefficient α_P, (Carbon Graphite) [17]	7-8.8 μm/(m·°C)
	Permeability Coefficient κ (Details in Appendix A)	3.7×10^{-15} m^2
PAD SUPPORT	Belleville Washer (BW) Material	1074 Carbon Steel
	BW Cone Height, h_0	0.30 mm
	BW Thickness, t	1.19 mm
	BW Cone Height to Thickness Ratio, h_0/t	0.255
	Stiffness of Two BWs and Pivot (Details in Chapter 1)	10.6-18.5 MN/m
AIR	Ambient Pressure, P_a	101 kPa
	Viscosity at 25.5°C, μ [18]	0.018 mPa·s

Figure 2 shows that a single pad consists of a porous carbon-graphite section epoxied to a steel case. Pressurized (P_S) gas enters the supply port on the pad casing; the porous carbon-graphite restricts the gas flow and reduces the gas pressure before the gas exits the pad surface facing the rotor. The material permeability (κ) and layer thickness (t_p) affect the local pressure and flow of

the air entering the film. The equivalent pad thickness (t_p) is 8.3 mm. Appendix A details the estimation of a pad permeability coefficient (κ) from experiments.

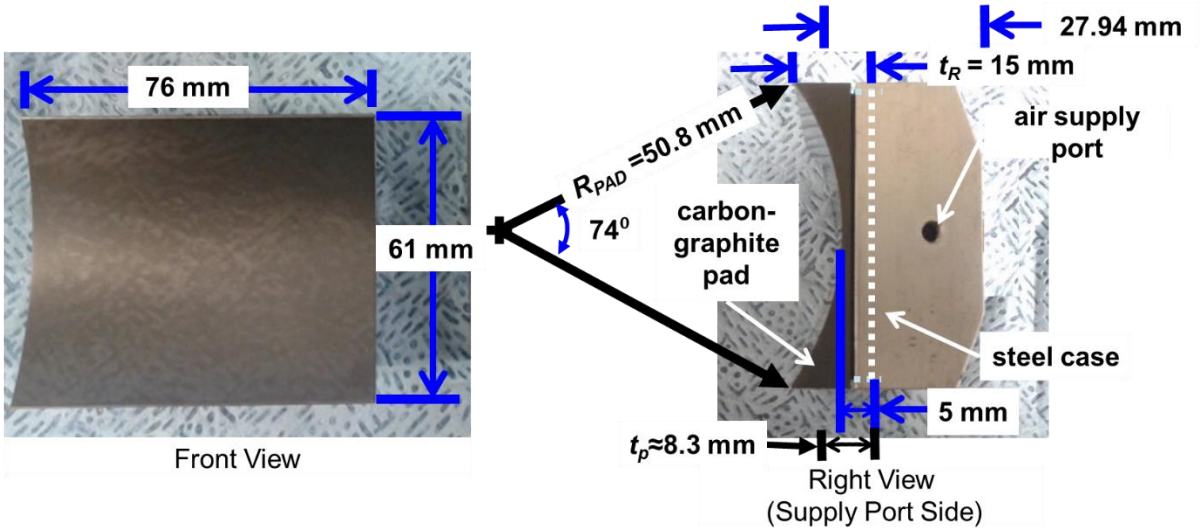

Figure 2: Photographs of a bearing pad (top and side views) with physical dimensions.

Figure 3 shows the back surface of a pad featuring a centered counterbore. The counterbore locating the pad on the pivot support houses two nested Belleville washers that separate the pad housing from the spherical pivot. Two of the pads feature targets for eddy current sensors to monitor pad vibration and measure pad tilt displacements (S_1 and S_2) during operation.

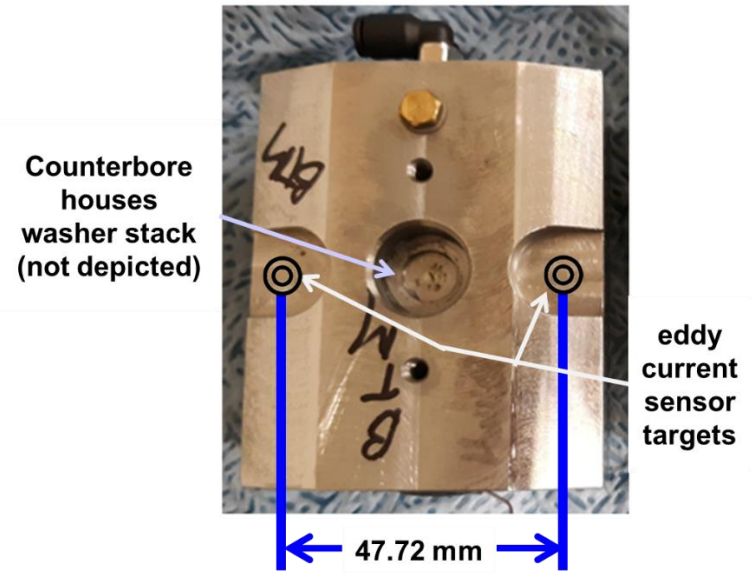

Figure 3: Photograph of a pad back surface showing counterbore to locate pivot support and locations of pad tilt displacement measurements.

Note that the tilting-pad supports of this bearing differ significantly from conventional pivot designs (e.g. rocker, integral flexure or spherical pivots). Figure 4 shows the pivot support and two nested Belleville washers (BW). The orientation and number of BWs set the maximum pad radial displacement. For two nested BWs, the maximum pad radial travel equals the distance to flatten a single washer (the cone height), 0.30 mm.

The spherical face of the pivot compresses the washer stack through an annular contact. The pivot features extra fine external threads that allow adjustment (~1.08 mm/full turn) of the radial location in the bearing housing to set the magnitude of the installation force pushing a pad against the rotor. A pivot is adjusted until a pad, when supplied with pressurized air (7.8 bara), lifts from the rotor a predetermined amount (~23 μm) that is measured with a dial indicator.

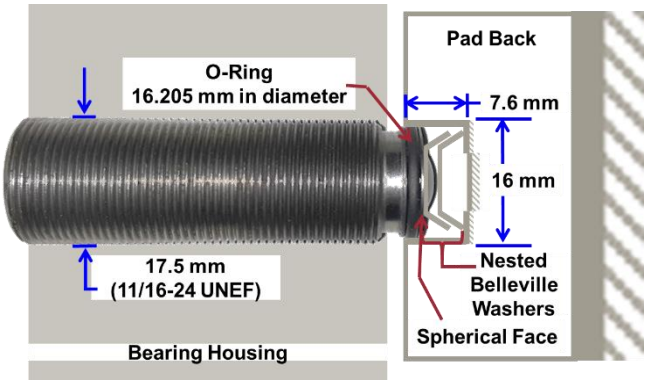

Figure 4: Schematic view of pivot pad support and two nested Belleville washers (not to scale)

As stated earlier, a pair of nested Belleville washers separate a pad from a respective pivot. Figure 5 shows a sketch of one BW cross-section, and includes the corresponding dimensions of the test BWs. Note the cone height ($h_0 \approx 0.30$ mm) and the washer thickness (t) labels. Again, the cone height quantifies the maximum distance the BW must deflect to flatten.

Figure 6 shows the force vs. deflection curves for a range of cone height-thickness ratios using a predictive tool in Ref. [19] and based on BW stiffness formulas in Ref. [20]. Notice that the BW stiffness (K_{SP}) becomes nonlinear as the cone height-thickness ratio $\left(\frac{h_0}{t} > 1\right)$ increases. The BWs are 1074 Carbon steel with $\frac{h_0}{t} \approx 0.255$, and the predicted K_{SP} is ~8.9 MN/m. Therefore, a linear regression of force and washer displacement measurements sufficiently models the stiffness of this washer geometry over the entire deflection range (i.e. from completely unloaded to completely flattened) of a single washer.

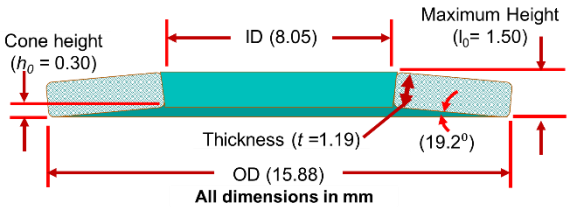

Figure 5: Schematic view showing Belleville washer cross-section to define cone height and thickness, (not to scale)

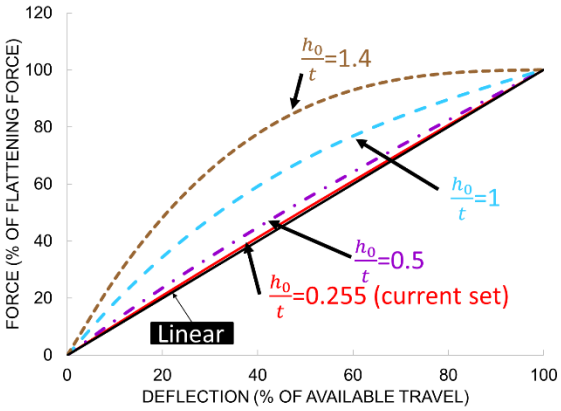

Figure 6: Applied force as a percentage of force to flatten vs. deflection for various cone-height to washer thickness ratios for a 1074 Carbon steel BW. Predictions based in analysis [19]

Chapter 1: Experiments to Identify the Stiffness of the Pivot Support

1.1: Pivot Support Stiffness

Figure 7 shows a schematic view of Rig 1 for quantifying the stiffness of a single Belleville washer. Test Rig 1 consists of a pneumatic cylinder (~2.7 kN maximum capacity) that applies loads to a test subject in compression. For this experiment, a single 1074 Carbon steel Belleville washer ($\frac{h_0}{t} \approx 0.255$) rests between two, flat steel surfaces. Refer to Figure 5 for other BW dimensions. A Bourdon type gauge (±0.14 bara) sets the pressure in the pneumatic piston and controls[3] the force applied to the washer. A dial indicator (±1.3 μm) measures the displacement of the piston face to determine the deflection of the Belleville washer. The setup assumes the measured displacement of the piston face equals the washer deflection under load.

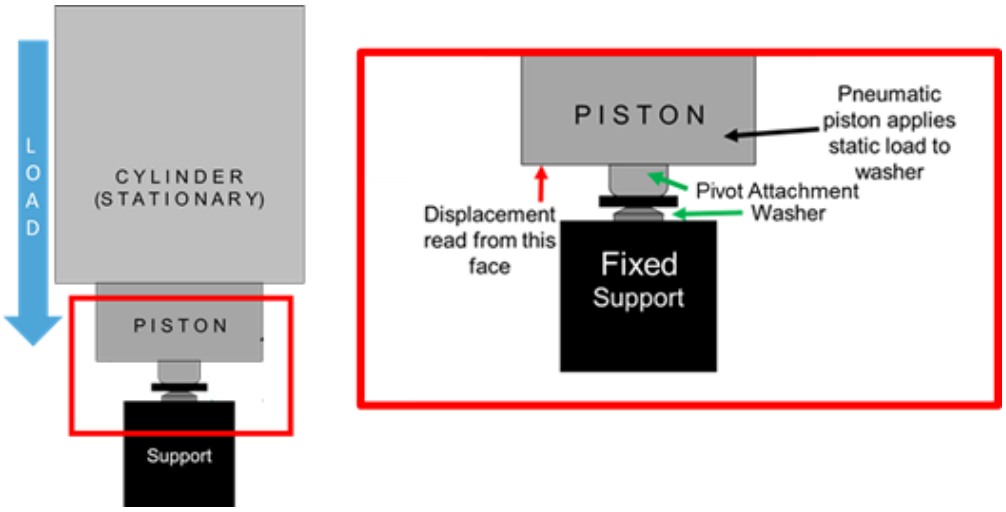

Figure 7: Schematic view (not to scale) of test rig 1 to quantify the stiffness of a single Belleville washer (BW).

Figure 8 shows the applied load and average deflection measurements for three separate trials. The inset schematic view shows the orientation of the BW relative to the fixed support and load direction. The maximum measured deflection at 274 μm is 90% of the nominal deflection to

[3] Prior to the washer-stiffness experiment, the piston applies static loads to a strain gauge load cell over a range of supply pressures to provide a reference of output force vs. air supply pressure.

flatten the washer (h_0 = 304 μm). A linear regression of the data gives K_{SP} of 9.3±0.1 MN/m. The BW predictive equation in Ref. [19] (see Figure 6) gives K_{SP} = 8.9 MN/m, which slightly underestimates the experiment result by 4.3%.

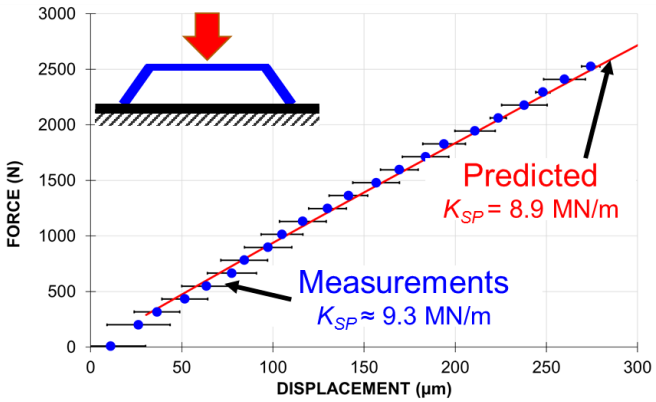

Figure 8: Applied load vs. deflection of single BW. Measurement and prediction based on Ref. [19].

The stiffness from compression tests of a single BW washer between two flat surfaces does not sufficiently characterize the pivot stiffness supporting each pad as there are two washers in contact with a spherical pivot. Therefore, the objective of the following experiment is to determine the stiffness of a stack of two nested washers, compressed between the spherical surface of the actual bearing pivot and a flat support surface emulating the base of the counterbore in the pad back.

Figure 9 shows a photograph of the setup to determine the stiffness of a stack of two nested Belleville washers when in contact with their actual pivot support. The experiment uses Rig 1 with two modifications. A bearing pivot[4] attaches to the pneumatic piston face and the test subject is a stack of two nested Belleville washers. A dial indicator displays the displacement of the piston

[4] A carbide tool cut the pivot easily in a manual lathe when making the features required to install the pivot in the piston face for the experiment. Thus, the pivot surface was not hardened.

face, which equals the deflection of the BW stack. Note the stacked washers are dry[5]. In later experiments, a nickel-based solid lubricant (Loctite® LB771) coats the washers' surfaces before installing them in a pad. The antiseize lubricant reduces friction between surfaces in contact.

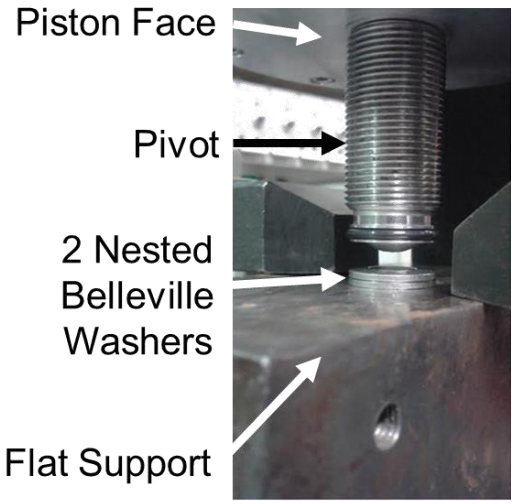

Figure 9: Photograph of Rig 1 configured to determine the stiffness of two, nested BWs when compressed with a pivot from the test bearing.

Figure 10 shows the average of three sets of measurements of applied load vs. BW stack deflection, with an inset schematic view depicting the washer stack orientation relative to the load direction and the rigid support surface. The deflection measurements show mechanical hysteresis and there is little variability (average standard deviation of ~1.4 μm) between the results of the three tests. Note that the maximum applied load (2.68 kN) does not flatten the washer stack. The maximum deflection measured is 151 μm, while the stack of nested washers should flatten at 304 μm. The slope of the trend line fitting the increasing load data approximates a stack stiffness of 20.6±2.2 MN/m as the deflection increases from 4 μm to 100 μm. The slope of the trend line for the decreasing load data gives a stiffness of 9.3±1.9 MN/m as the stack deflection reduces from

[5] No antiseize coating

109 µm to 1 µm. The washer stack still returns to zero deflection when the load is only the weight of the piston (~8 N without supply air).

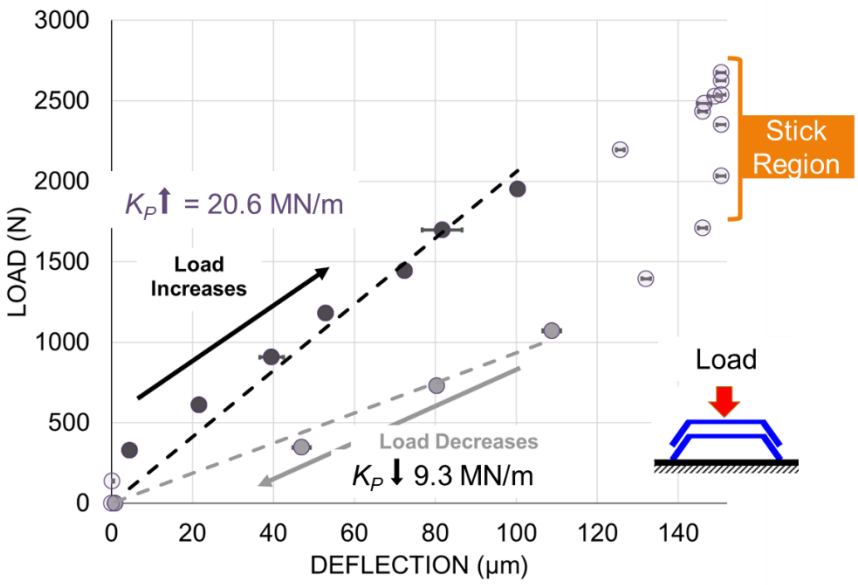

Figure 10: Static load vs. deflection of two nested BWs. (Average measurements from three tests and fit lines). Inset schematic view depicts load direction and two stacked washers.

Recall from Figure 8 that the stiffness of a single washer (K_{SP}) is ~9.3 MN/m. Under increasing load, the BW stack stiffness (K_P↑=20.6±2.2 MN/m) is ~2.2·K_{SP}, while when reducing the applied load, the BW stack stiffness (K_P↓=9.3±1.9 MN/m) equals K_{SP}. Petele [21] notes that N-nested washers have an equivalent stiffness equal to $N \cdot K_{SP}$. Sliding friction within the stack elements could cause a deviation from this prediction of ±4% to ±6% [21]. Thus, friction between the washers seems an unlikely explanation for the stack hysteresis seen in Figure 10. The mechanical hysteresis did not reduce by increasing the time increment to remove the load. The stack would eventually (in a few minutes) return to zero deflection after completely removing the load.

Instead, the large mechanical hysteresis is more likely due to the roughened region of the pivot surface contacting the top Belleville washer in the stack, which increased the contact area

and resulted in a larger friction force. Figure 11 shows an example of a shallow wear ring produced on a pivot face from contact stress with a Belleville washer during tests of the bearing assembly and an inset schematic to depict the contact. The wear preceded the washer stack experiment. The machinability of the pivot material and the visible gouge on the pivot surface render it unlikely that the pivots had any sort of heat treatment to reduce fretting wear from contact stress due to the Belleville washer. Nevertheless, the wear is not severe enough to create a difficulty separating the washer and pivot after applying a compressive load.

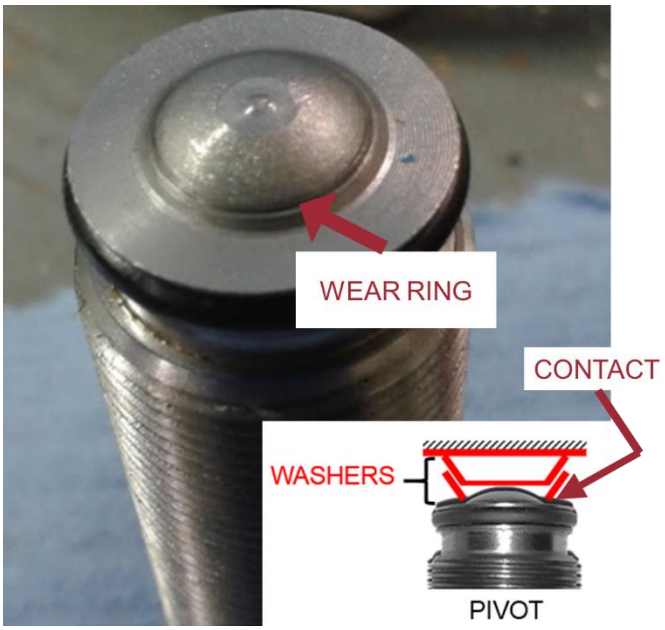

Figure 11: Photograph of wear ring on pivot spherical face from line contact with Belleville washer, with inset schematic showing washer-pivot contact.

Do realize that most of the knowledge provided in this section applies to large loads and displacements, whereas tests of the bearing assembly with shaft speed did not exceed loads of 890 N and displacements of ~90 μm (see later Chapters 2-5). Moreover, the experiment does not account for contact friction between a pivot-mounted O-ring and the counterbore wall in a pad housing. Thus, the process to identify the pivot stiffness assumes an O-ring adds little resistance

to a change in load because the contact area is small and does not contribute a significant friction force.

1.2: Pad Installation during Bearing Assembly

As the pivot screws into the bearing housing to push a pad against the rotor, the pivot sets a specific preload on a pad by compressing the BWs. The specific preload must allow the BW stack to deflect and the pad to lift sufficiently from the rotor surface when supplied pressurized air. Thus, it is important to avoid flattening the washer stacks when installing the pivots and pads in the bearing housing.

The specific preload equals the force (F_P) exerted on the pad divided by the projected area ($L \cdot w$) of one pad. Figure 12 shows the washer stack cannot deflect more than h_0 (0.304 mm) due to the net force acting on the stack. Figure 13 shows that upon assembly the pivot location sets the preload force and causes a stack deflection proportional to the force ($1/K_P\uparrow \approx 0.054$ μm/N).

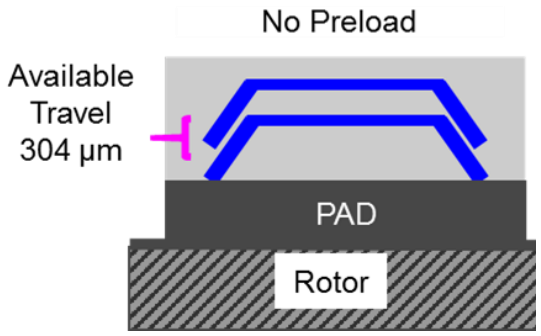

Figure 12: Schematic view, not to scale, of two nested BWs, pad and rotor surface to show that the BW stack cannot displace more than 304 μm

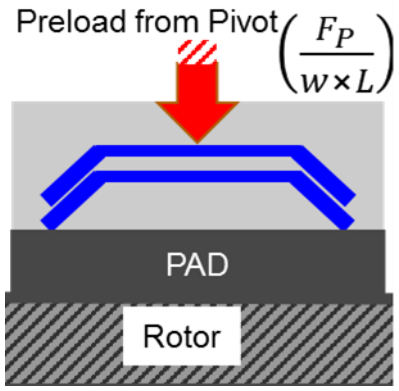

Figure 13: Schematic view, not to scale, of a BW stack, preload force from pivot, pad and rotor section, showing preload force can compress a washer stack

Chapter 2: Experiments to Characterize the Test Bearing Structure

2.1: Description of Test Rig

Figure 14 shows a schematic view of the rig (Rig 2) used to determine the static and dynamic load performance of a fluid film bearing. Chapters 2-5 describe experiments using the rig. The rig consists of stiff pedestals that support a rotor (OD 101.59 mm) via two angular-contact ball bearings. The ball bearings are oil-mist-lubricated, in a back-to-back configuration, and are ~457 mm apart. Three buffer seals attach to the pedestal walls to prevent oil mist from contaminating the test bearing.

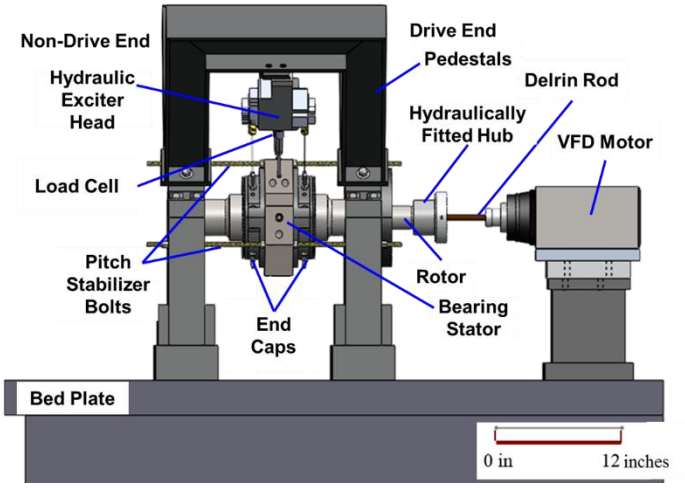

Figure 14: Front view of Rig 2 for bearing experiments

A 7.5 kW motor with a variable-frequency drive (VFD) provides power to the rotor through a thin Delrin® rod (OD 12.7 mm, length 108 mm). The opposite end of the rod is press-fit into a flanged fitting that connects to a hydraulically fitted hub on the rotor via six match-weighted bolts.

A test bearing installs atop the shaft midsection between the two pedestals. Six threaded rods (OD 9.5 mm), referenced as “pitch stabilizers”, secure the bearing housing to the outer walls of the pedestals. Tightly securing these rods to the pedestal walls restricts the angular tilt of the bearing without adding a sizeable lateral stiffness to the system.

Figure 15 shows a photograph of the side (axial) view of Rig 2 with a coordinate system (*X*, *Y*) overlaid. Stinger attachments connect electrohydraulic shakers (mounted to the pedestal top above the test bearing) to the test bearing housing. The shakers load the bearing along the coordinate axes.

A controlled supply of pressurized oil sent to a piston in the shaker head generates a static (nominal) load. Dynamic loading about the nominal load requires an externally supplied control signal, and the hydraulic shakers are capable of single or multi-frequency excitations. Strain gauge type load cells, rated to ~11,120 N, separate the housing from each shaker head and measure both static and dynamic loads. Dynamic loads applied to the gas-lubricated bearing target a maximum waveform amplitude of ±133 N (±30 lbf), with frequencies extending to 350 Hz in 10 Hz increments.

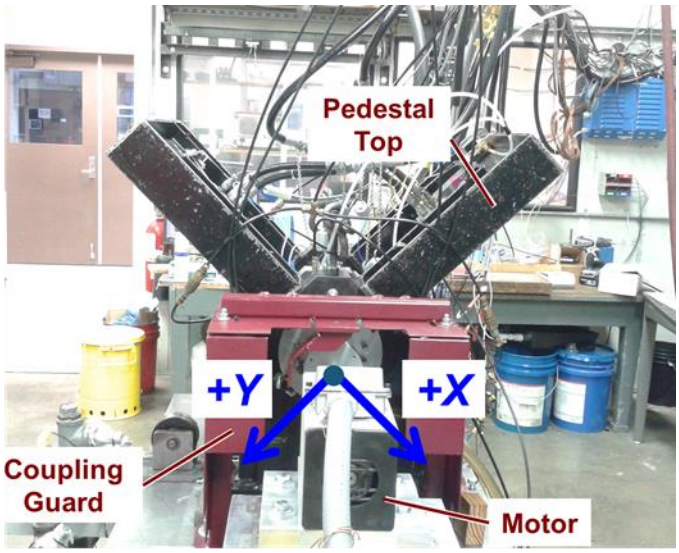

Figure 15: Photograph (axial view) of test rig with coordinate directions superimposed.

Figure 16 shows a photograph of the bearing (front view) installed in Rig 2. Notice that end caps attach to the drive and non-drive faces of the bearing housing. Two eddy current sensors mount orthogonally on each end cap to measure the housing displacement relative to the rotor in

the *X* and *Y* directions. An arithmetic average of the displacement measurements in the same direction from both sides (drive side and non-drive side) determines the radial displacement of the bearing housing. Piezoelectric accelerometers attach to the bearing housing exterior, on the face opposite the applied load, to record *X* and *Y* dynamic accelerations. A J-type thermocouple attaches to the non-drive side of each steel pad casing to record its temperature.

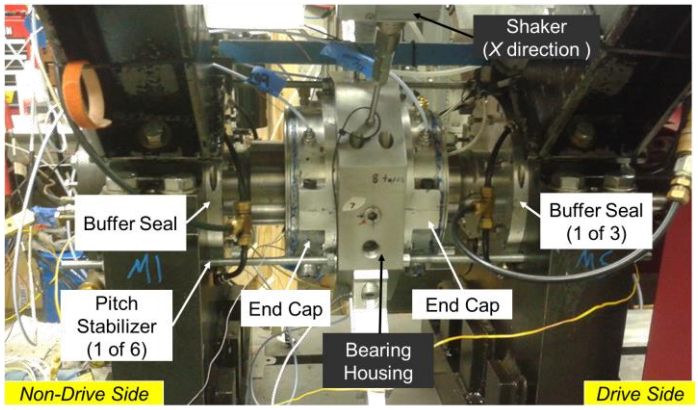

Figure 16: Photograph of bearing with end caps and pitch stabilizers in Rig 2.

Three Labview® virtual instruments (VI) form the data acquisition system. One VI records and displays temperature measurements of the pads and air film. The second VI records and displays steady state measurements that include the applied load, the operating shaft speed, two pad displacements (relative to housing), the housing displacement (relative to rotor), supply air flow rate, and air supply pressure into the pads. The third VI controls the shakers' excitation and records the applied dynamic forces, housing accelerations, and housing displacements (relative to rotor). The sampling frequency of the third VI is 10 kHz. A separate system, comprised of a ten-channel signal analyzer (IOtech® 652u) and software (eZ Analyst®), provides supplementary real-time, frequency spectra plots of both the bearing housing and two pads (one loaded, one unloaded).

Figure 17 is a schematic view of the bearing assembly with labels showing the shaft rotation direction and the coordinate system (*X*, *Y*). Although the pivot offsets and motor permit

clockwise and counterclockwise rotation, the following experiments use a left-handed coordinate system to be consistent with past work and analysis [22, 23]. The "upstream" and "downstream" labels describe the pad location relative to the applied static load and direction of shaft rotation. Three J-type probe thermocouples (approximately 0.51 mm from the rotor OD) measure the temperature of the ambient air near the leading edge of the upstream loaded pad (Pad 1 in Figure 17). Two eddy current sensors mounted on the bearing housing monitor the motion of two pads (Pads 2 and 4 in Figure 17).

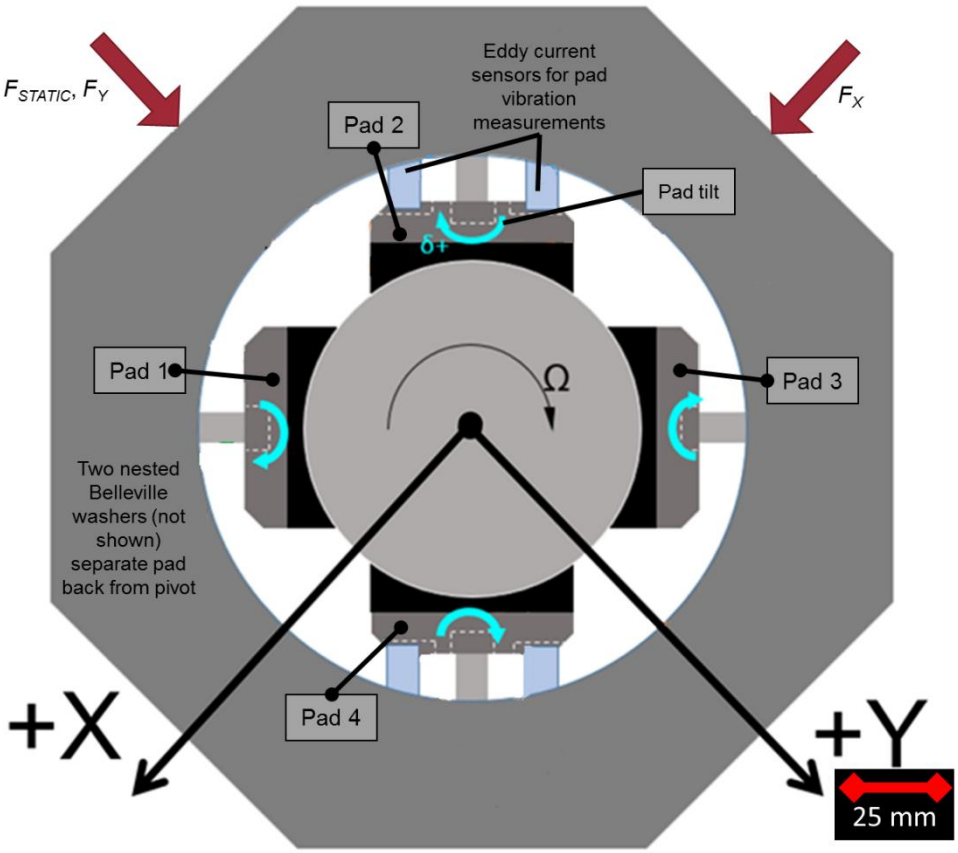

Figure 17: Schematic view of bearing assembly and coordinate system (not to scale) with pad locations relative to direction of applied static load and shaft rotation.

Results of a simple experiment (where the bearing pads attach to the housing exterior) verify that although the stiffnesses of the pitch stabilizers act in parallel with that of the test bearing,

the pitch stabilizers do not significantly affect the test bearing response to excitation forces. Applied forces and bearing housing displacements along the X and Y directions produce an isotropic baseline radial stiffness (K_b) of the pitch stabilizers as $K_b \approx 0.48 \pm 0.1$ MN/m. Appendix B contains more information on the results of the static load test. The baseline mass (M=20.2 kg) of the installed bearing is the sum of the masses of the bearing housing, its four pivots and four pads, two end caps and 38% of the pitch stabilizer masses[6].

The following three assembly steps finalize the test bearing installation in Rig 2:

1. Bearing Offset Relative to Rotor: During this step, the shaker heads do not attach to the bearing housing, and the pads rest on the rotor. A depth micrometer measures the distance between the housing exterior and the rotor. Adjustments to the pad pivots center the housing to the rotor within ± 0.025 mm vertical and ± 0.064 mm horizontal[7]. Figure 18 shows the reference surfaces for the bearing offset measurements. The housing split line bolts are preloaded to 70% of the bolt proof strength (torque = 53 N·m) before installing the pads to ensure the reference surfaces on the bearing housing are the same distance (127 mm) from the geometric center.

[6] The effective mass of a fixed-fixed beam is ~38% of the total mass [24].
[7] Note that once a pair of pads is positioned, those pads rest on the rotor, and it becomes hard to move the housing orthogonally to adjust Pad 1 and Pad 3. Hence, the tolerance is higher in the horizontal direction because the horizontal pads are set after the vertical pads.

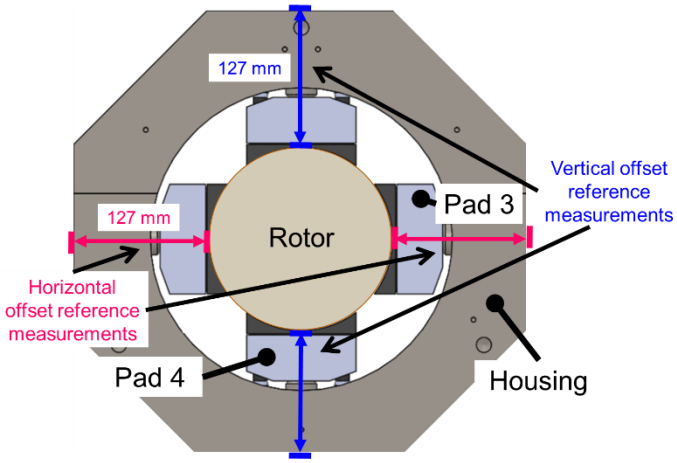

Figure 18: PGB and pads (axial view) with arrows showing reference measurements for setting the bearing horizontal and vertical offsets.

2. Bearing Angularity Relative to Pedestal: The left view in Figure 19a shows locations where an inside micrometer measures the distance from the non-drive side face of the bearing housing to the closest pedestal at three locations. The front view in Figure 19b shows the measurement locations on the bearing housing face. Adjusting the pitch stabilizers reduces the angular misalignment to $\pm 0.013^0$. This is achieved when the measurements, shown in Figure 19a near Pads 2 and 4, are within ~0.051 mm of each other and within ~0.025 mm of the measurement near Pad 3. Even then, the possible angular misalignment could cause a pad axial tilt that produces a lateral displacement of ~17 μm at the pad ends. Hence, the installed pads likely lift from the rotor more than ~17 μm when supplied with air. After operation with shaft speed there were no burnish marks on the carbon surfaces due to pad axial tilt, thus indicating the angularity tolerance was acceptable (and remained as such throughout testing).

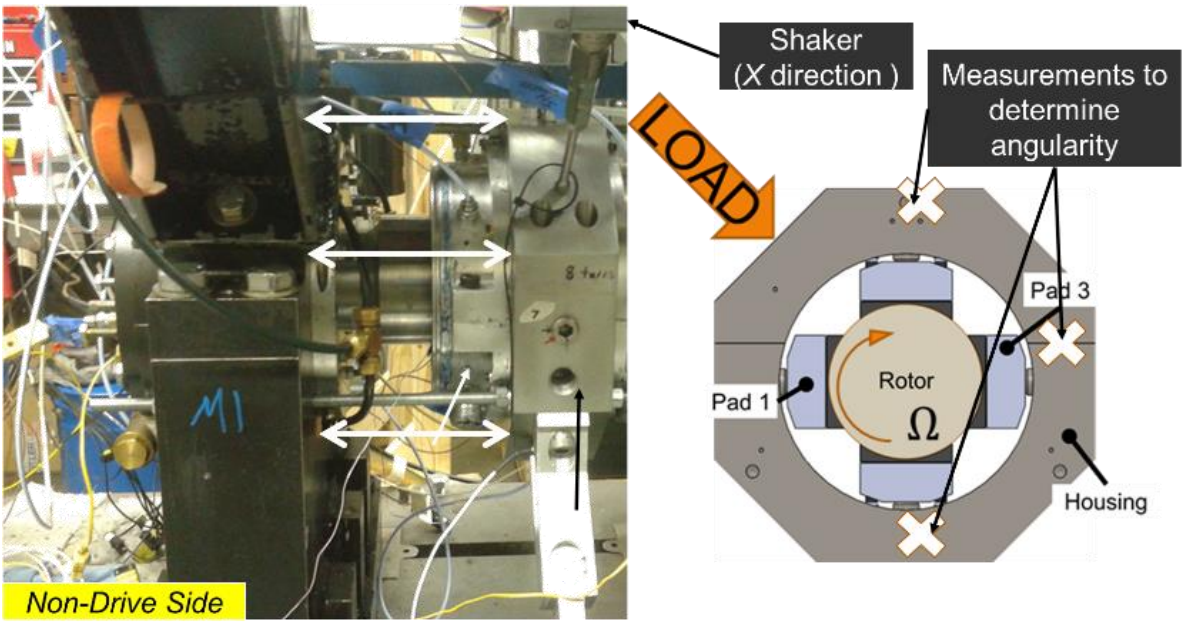

(a) (b)

Figure 19: (a) Photograph of test rig marked with distances measured from non-drive bearing face to adjacent pedestal and (b) locations of measurements on bearing face to determine bearing angularity during installation in Rig 2.

3. Pad Lift from Rotor Surface: A dial test indicator (±1.3 μm) on a shaft alignment fixture chained to the rotor presses against the back of a pad while the pad has no supply air. Figure 20 shows a photograph of this setup. The indicator measures the pad displacement relative to the rotor as the supply pressure increases to 7.8 bara maximum. The relative displacement is the nominal film thickness. The supply air switches on and off several times to ensure the pad lift is consistent. While setting a pad lift the adjacent pads do not receive pressurized air to isolate the targeted pad.

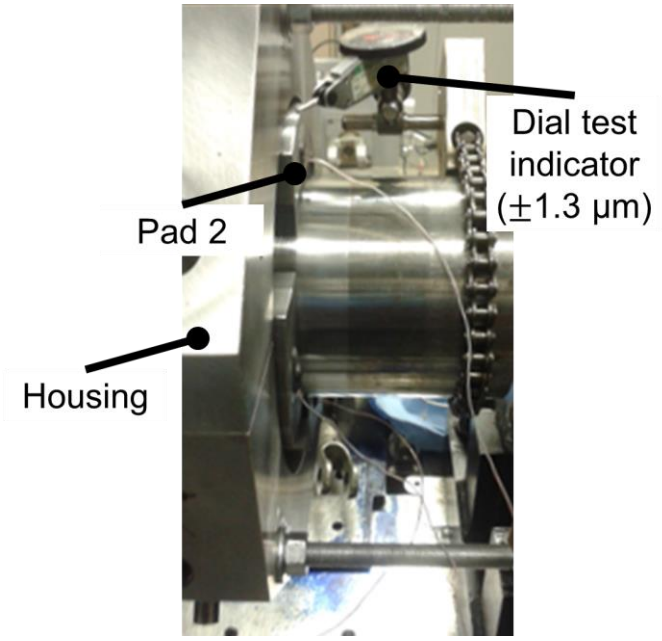

Figure 20: Test dial indicator setup to measure pad fly height.

Moreover, Figure 21 shows a schematic view (not to scale) where an opening force from the pressure field in the film causes the pad to lift while deflecting the washer stack. There was no access to measure the initial washer deflection from the pivot setting.

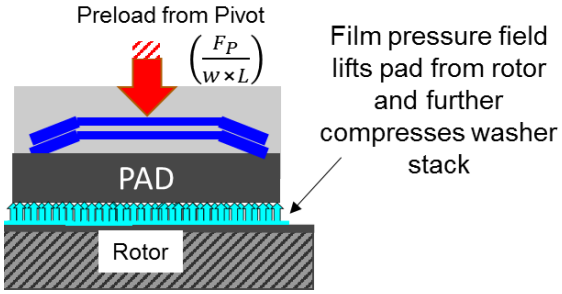

Figure 21: Schematic view of BW stack, pivot preload, rotor section, pad and film (not to scale).

The pivots are set such that the pads in the bearing assembly lift 23±1.3 μm from the rotor surface when supplied 7.8 bara air. This requires a partial turn (typically less than a ¼

revolution[8]) of the pivot compared to the coarser pivot adjustments used to first set the bearing offset. Note, the pivot turn increment is not measured precisely, because the dial indicator directly measures the pad lift after a pivot adjustment.

Figure 22 shows the displacements of Pad 2 and Pad 4 relative to the rotor vs. supply pressure while the shaft is stationary. Eddy current sensors measured the displacement of the pad backs (Figure 3) relative to the housing and the displacement of the housing relative to the rotor. The supply pressure first increased and then decreased during the test.

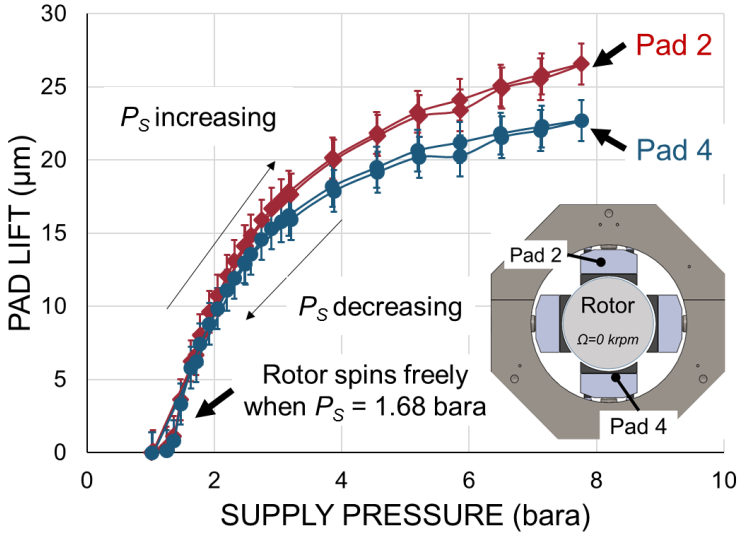

Figure 22: Pad lift vs. supply pressure from eddy current sensor measurements. No shaft speed.

Recall from Figure 10 that the displacement of the Belleville washer stack for an increasing and decreasing load showed mechanical hysteresis. The data in Figure 22 does not show mechanical hysteresis for the tests conducted with both increasing and decreasing supply pressures.

[8] A ¼ revolution corresponds to ~270 μm radial displacement, whereas the coarser adjustments used to set the bearing offset are full turns (~1.08 mm radial displacement/turn).

The pitch stabilizer rods and shaker head attachments help to support the weight of the bearing, and the pad radius closely follows that of the rotor over the pad arc length (74˚). The rotor freely spins by hand when the supply air pressure is ~1.68 bara. When P_S is 7.8 bara, Pad 2 lifts ~27±1.4 μm and Pad 4 lifts ~23±1.4 μm.

Once the pad receives pressurized air, an estimate for the resulting increase in pad preload force F_P (assuming the washer deflection equals the pad lift) is the product of $K_P\uparrow$=20.6 N/μm and the measured pad lift. Figure 23 shows this estimated increase in specific pad preload ($F_P/(L \cdot w)$) vs. supply pressure. For 7.8 bara supply air, the estimated increase in specific pad preload is 106 kPa for Pad 2 and 90 kPa for Pad 4.

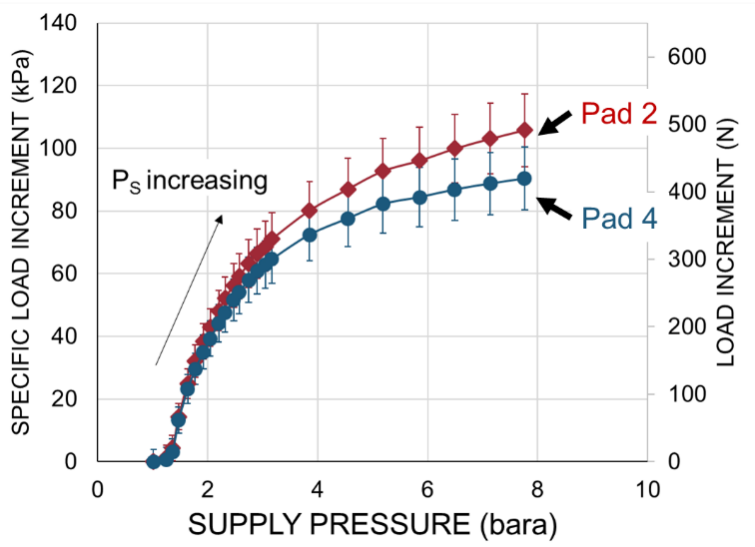

Figure 23: Increase in pad preload due to pad lift vs. supply pressure. No shaft speed.

2.2 Experiments to Determine the Test Bearing Structure Stiffness (No Gas Film, Pads in Contact with Stationary Rotor)

The purpose of the following set of experiments is to quantify the stiffness (K_U) of the bearing structure by measuring the housing displacements relative to the stationary rotor due to applied static loads for a condition where there is no air supplied to the pads. The slope of a trend line fitting the resulting force vs. displacement data estimates the structure stiffness and is useful as a base line reference to assess a change in bearing stiffness due to the gas film in later experiments.

The bearing installs in Rig 2 for the aforementioned tests. The pivot settings are such that the pads lift ~23 μm when air is supplied at P_S=7.8 bara (see Figures 20 and 22).

The hydraulic shaker head (*Y* direction) applies a static load to the assembly while the eddy current sensors measure the housing displacement relative to the rotor. During the experiment, the rotor is stationary and the pads do not receive a supply of pressurized air. Figure 24 shows the measured applied load (increasing and decreasing) vs. housing displacement. The bearing stiffness calculates from the data within the bearing displacement range occurring for the tests detailed in Chapter 5 (static and dynamic loads with shaft speed).

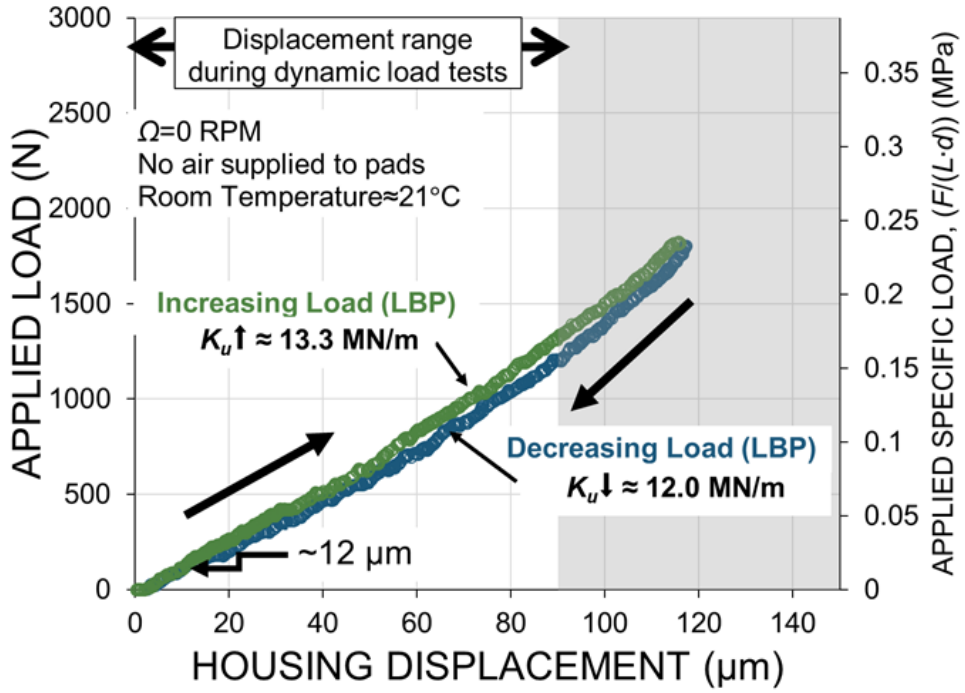

Figure 24: Applied static load vs. bearing housing displacement. Test at room temperature (*T*=21˚C). No shaft rotation. No pressurized air supplied to pads.

The bearing understructure stiffness (K_U) depends on the loading condition and does not include the stiffness of the pitch stabilizers. K_U↑ = 13.3±0.04 MN/m is from a linear regression of the increasing load data for housing displacements ranging from 0 µm to 90 µm. K_U↓ = 12.0±0.05 MN/m is from a linear regression of the decreasing load data for housing displacements ranging from 90 µm to 0 µm. The measurements evidence a minor mechanical hysteresis once the bearing structure displaces more than ~12 µm.

2.3: Experiment to Quantify the Stiffness of the Bearing Structure at a Higher Temperature (T=41˚C)

The next experiment determines the bearing structure stiffness (K_U) at a higher temperature to assess its effect on the applied load vs. bearing displacement results. The pads are in contact with the rotor since there is no supply air for these tests.

First, the air supply causes a pressure in the film to form and the pads to lift. Then, the rotor operates at 9 krpm with static load (not exceeding 100 kPa due to a ~780 N load) along the Y direction for the pads to reach an equilibrium operating temperature. The rotor stops, and the pad air supply disengages to measure applied loads and housing displacements at the higher temperature (~41°C). Figure 25 shows the measured applied static load (LBP) vs. the displacement of the bearing structure.

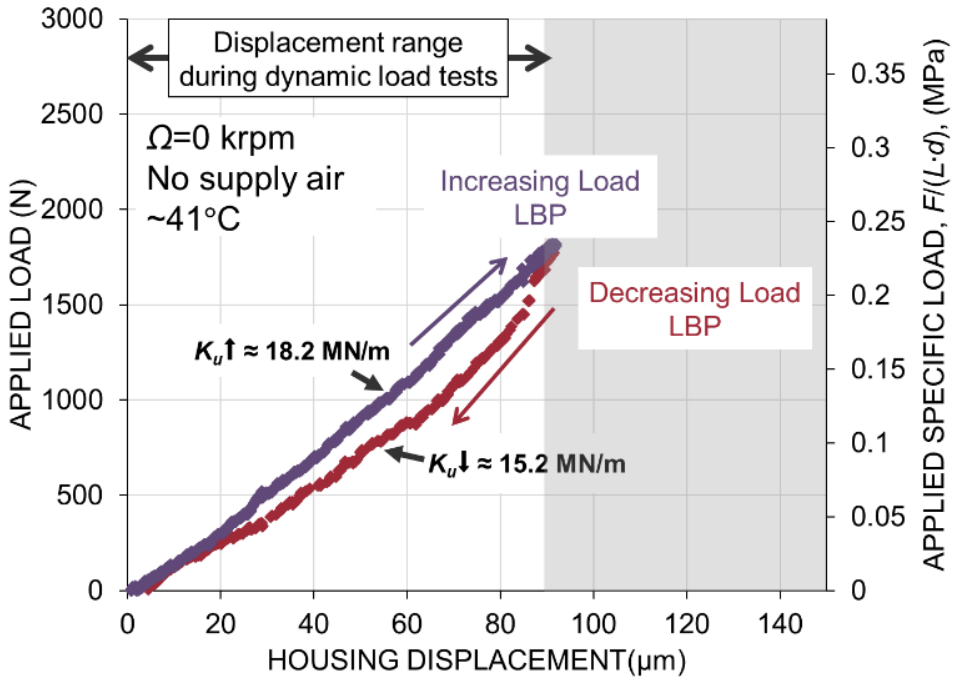

Figure 25: Applied static load vs. bearing housing displacement. Test at temperature T=41°C. No shaft rotation. No pressurized air supplied to pads.

The stiffnesses under load and unload conditions for deflections ranging from 0 μm to 90 μm are $K_U\uparrow \approx 18.2\pm0.08$ MN/m and $K_U\downarrow \approx 15.2\pm0.19$ MN/m, respectively. The results shown in

Figure 24 and Figure 25 are from one test each. Again, a minor mechanical hysteresis[9] occurs for bearing displacements larger than ~12 μm.

To summarize the results of the two experiments, Table 2 lists the bearing structure stiffness (K_U) under increasing (↑) and decreasing (↓) loads for each test and compares them against the pivot stiffness (K_P) for context. Recall that the pads are in contact with the rotor during the tests, there is no supply of air, and the shaft is stationary.

Table 2: Bearing structure stiffness (K_U) during loading and unloading for two tests (no film, no shaft speed). Stiffness of a washer stack (K_P) given for comparison.

Average Pad Temperature	Stiffness under Increasing Load ($K\uparrow$)	Stiffness under Decreasing Load ($K\downarrow$)	Maximum Deflection Used in Stiffness Estimate	Comments
[°C]	[MN/m]	[MN/m]	[μm]	
21	13.3±0.04	12.0±0.05	90	Bearing Structure, K_U
41	18.2±0.08	15.2±0.19	90	Bearing Structure, K_U
	20.6±2.2	9.3±1.9	109	K_P from a Pivot and Two Washers

The bearing stiffness from the static load test with the pad temperatures at 41°C is higher and changes more due to the load condition than the static load test at room temperature (see Figure 25 vs. Figure 24). There is not a direct explanation for the change in K_U between the two tests. The bearing structure stiffness (K_U) from the two tests does not exceed the range of K_P (from 9.3 MN/m to 20.6 MN/m).

The experiment results in Table 2 combined with the pad lift measurements from Figure 22 provide information regarding the influence of the nested Belleville washers (BW) on the bearing assembly. The results of the experiment to determine the pivot stiffness (K_P) show that

[9] Results of ten static load tests on the bearing (albeit while supplied with 7.8 bara air) with a stationary rotor showed the mechanical hysteresis was repeatable and did not diminish over time.

compressing and decompressing the BW stack will cause mechanical hysteresis in the system response (see Figure 10). The pad displacement vs. supply pressure measurements in Figure 22 show no evidence of mechanical hysteresis for a pad displacement of ~27 μm in line with the pivot axis. The bearing structure stiffness (K_U), from the data in either Figure 24 or Figure 25, shows a slight mechanical hysteresis occurring after the bearing displaces ~12 μm when the load orientation is between two pads (45˚ from each pivot axis). Moreover, the structure stiffness (K_U) remains constant for a load (increasing or decreasing) and temperature condition.

The results of the experiments to determine K_P and K_U do not correlate. Figure 26 is a schematic view of the bearing with radially distributed springs to represent the stiffness of each pivot assembly contributing to the structure stiffness. Two springs, each oriented 45˚ from the static load direction, contribute to the structural stiffness (K_U), if only the Belleville washer stacks behind the loaded pads (Pad 1 and Pad 2) affect the structural stiffness. For the schematic shown in Figure 26, the model predicts a structure stiffness equal to the stiffness of a single spring, ~K_P.

Figure 27 is a schematic view of the bearing structure representing the case where all four Belleville washer stacks have an initial deflection. If the stiffness (K_P) of a washer stack is correct, the model shown in Figure 27 does not represent the bearing during the structure stiffness tests (Figures 24 and 25) because the model predicts a structure stiffness much higher than that obtained from the data ($K_U\uparrow$=13.3 MN/m and $K_U\downarrow$=12.0 MN/m at T=21°C).

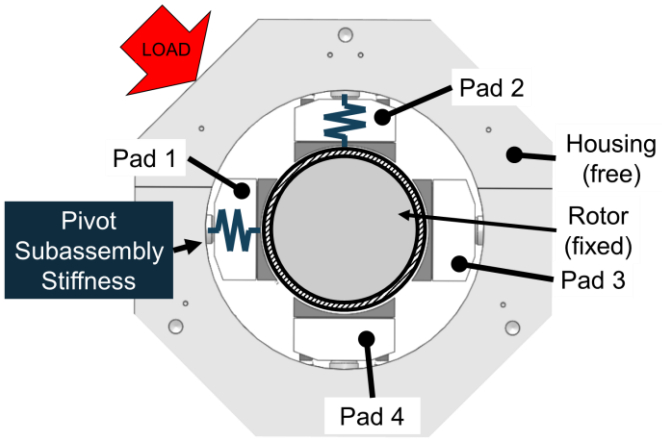

Figure 26: Schematic of bearing structure represented with a distribution of spring elements, with no initial deflection of the Belleville washers due to the pivot installation.

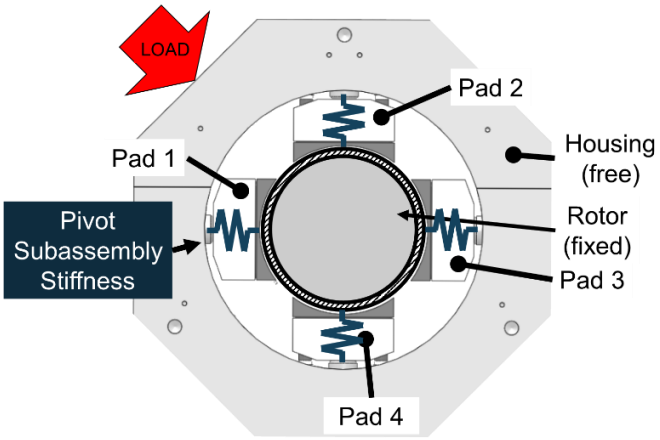

Figure 27: Schematic of bearing structure represented with a distribution of spring elements, where the Belleville washers have an initial deflection from the pivot assembly setting.

Chapter 3: Experiments to Characterize the Test Bearing Operating with Supply Pressure and No Shaft Speed

3.1 Bearing Stiffness (K_a) Considering Hydrostatic Effects and Pad Temperature, Stationary Shaft

The next set of static load experiments without shaft speed considers the bearing with air supplied to the pads at two distinct temperatures. For the two tests, the air supply pressure (P_S) is 7.8 bara. The supply pressure is well above the minimum pressure (~1.7 bara) required for a pad to lift from the rotor. Results are useful to estimate the bearing stiffness (K_a) due to hydrostatic effects.

For the first test, with the bearing installed in Rig 2, the *Y* direction shaker applies a static load, while the eddy current sensors in the end caps measure the housing displacement relative to the stationary (rigid) rotor. During this test, the bearing is at room temperature (T≈21°C-26°C).

Next, the bearing pads, still supplied with 7.8 bara air, heat to a representative operating temperature (T≈41°C) as the rotor spins at 9 krpm (surface speed of 48 m/s), and a light[10] static load is applied. Once the thermocouples attached to the pads achieve thermal equilibrium, the rotor is brought to a stop. Then for the second test, the hydraulic shaker applies a static (LBP) load while the bearing remains at ~41°C.

Figure 28 shows the measured applied load vs. housing displacement for P_S=7.8 bara when the bearing is at (a) room temperature (T≈21°C) and (b) a higher temperature (T≈41°C). Figure 28 also includes the measurements from experiments to determine the bearing structure stiffness

[10] The static specific load ($F/(L \cdot d)$) increases to no more than 100 kPa due to a ~780 N load.

where P_S=1 bara (Table 2). Arrows distinguish the data collected as the static load increases (⬆) from the data collected as the static load reduces (⬇).

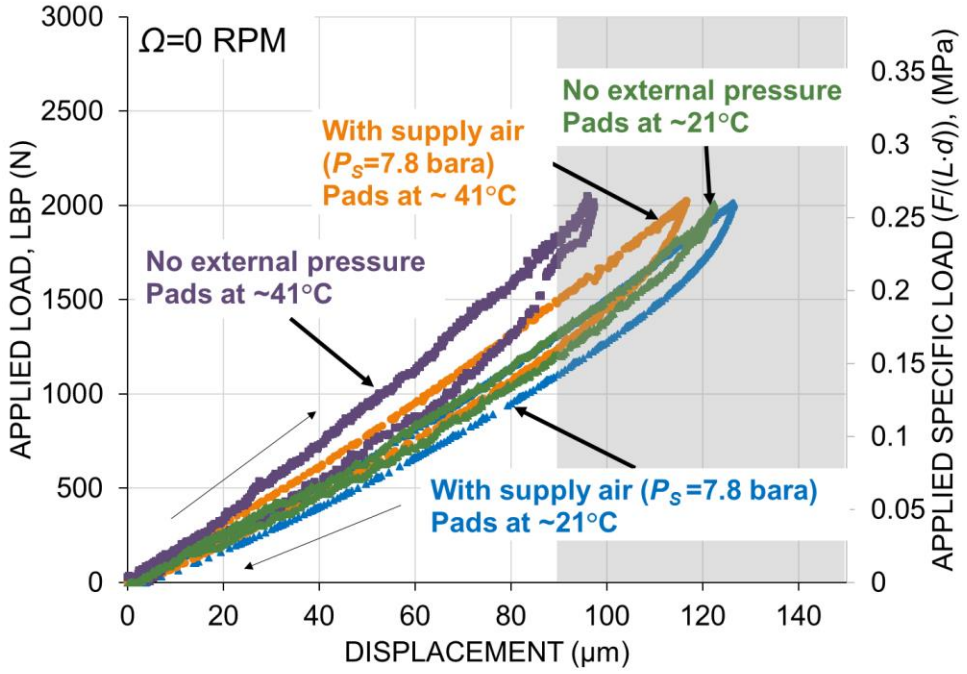

Figure 28: Applied load (LBP) vs. housing displacement relative to a stationary rotor. Tests with and without air supply pressure, and bearing temperature at ~21°C and ~41°C.

The data sets in Figure 28 indicate that for a given load, the bearing at room temperature displaces more than the bearing at ~41°C, regardless of whether or not there is a film. Thus, the increase in bearing stiffness with temperature is inherent to the structure. As discussed in Chapter 1, the mechanical hysteresis is from the pad supports (pivots and nested Belleville washers), not from the air film. The mechanical hysteresis shows immediately as the bearing displaces while supplied 7.8 bara air. Again, please notice the hysteresis is very small compared to that in Figure 10.

For large displacements, at a fixed load and fixed temperature, the aerostatic[11] bearing stiffness (K_a) is less than the structure stiffness (K_U). Table 3 shows the bearing stiffness derived from the load and displacement measurements. The results do not include the pitch stabilizer stiffness ($K_b \approx 0.48$ MN/m, as shown in Appendix B).

Table 3: Derived aerostatic bearing stiffness (K_a) for tests conducted at two average pad temperatures (21°C, 41°C) with bearing structure stiffness (K_U) for comparison. Displacements range 0 μm to 90 μm. No shaft speed.

Average Pad Temperature	Supply Air Pressure (P_S)	Stiffness from increasing load data	Stiffness from decreasing load data	Comment
[°C]	[bara]	[MN/m]	[MN/m]	
21	none	13.3±0.04	12.0±0.05	K_U, Table 2
41	none	18.2±0.08	15.2±0.19	K_U, Table 2
21	7.8	13.4±0.05	10.9±0.11	K_a
41	7.8	15.7±0.04	12.5±0.09	K_a

There is little difference between the aerostatic bearing stiffness (K_a) and the structure stiffness (K_U). For the higher temperature (41°C), Table 3 shows a slight decrease (13-18% of K_U) in the bearing stiffness from that of the structure due to the pressurized air. At room temperature, K_a differs no more than 9% of the structure stiffness. This indicates that the film stiffness is higher than that of the structure.

Figure 29 shows a schematic view representing the bearing with an air film as a distribution of spring elements for the equivalent stiffness due to the film under each pad (K_F) and the equivalent bearing structure stiffness (K_U) to explain the slight decrease in bearing stiffness due to the film. Note that K_U is in series with K_F and the overall housing displacement is small such that each spring displaces along its respective axis.

[11] Aerostatic in the sense that there is no shaft speed and the pads receive pressurized air

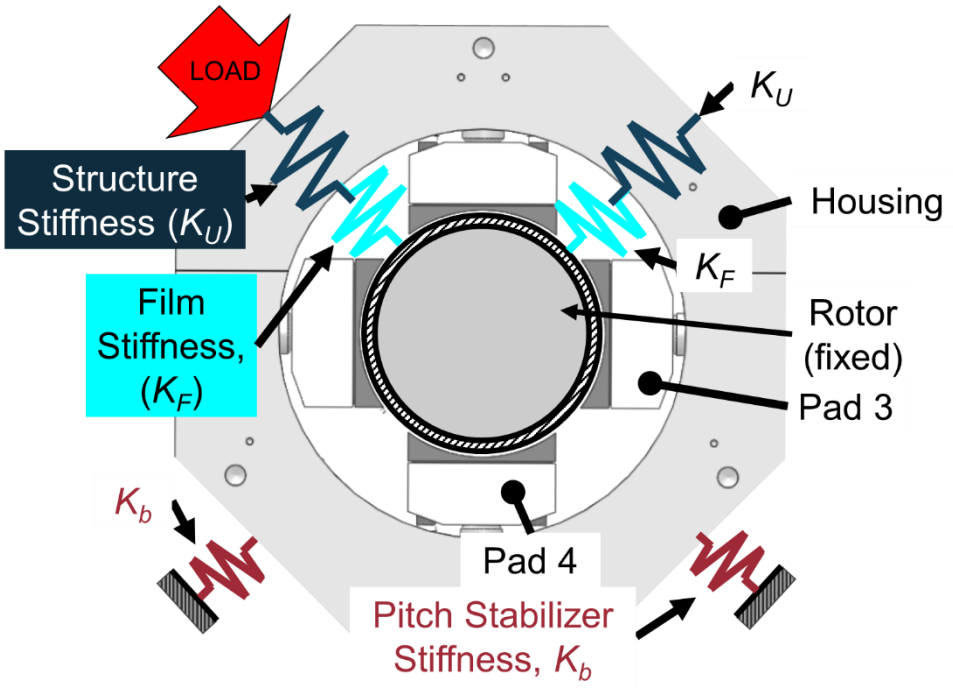

Figure 29: Schematic view of test bearing with springs representing equivalent film stiffness (K_F), equivalent bearing structure stiffness (K_U) and equivalent pitch stabilizer stiffness (K_b).

3.2 Determination of Bearing Stiffness with Supply Pressure, Static Loading Procedure with Impacts and Stationary Shaft

Another experiment with an alternative load procedure better estimates the stiffness of the bearing with its pads supplied with air at P_S=7.8 bara. Impacting the housing between load increments along the *X* and *Y* directions assists the bearing to overcome the mechanical hysteresis in the pivot assemblies prior to measuring the load and housing displacement relative to the rotor.

The bearing installs in Rig 2, and the pads receive pressurized air at P_S=7.8 bara. The rotor is stationary. The *Y* direction shaker head applies a static load (LBP) to the bearing, while the eddy current sensors in the end caps measure the housing displacement relative to the rotor. An initial test records the applied load and bearing displacement according to the original loading procedure. Then in a second test, before recording measurements at each load increment, a hammer delivers an impact load (independently along the *X* and *Y* directions) to a wooden stake held against the bearing housing to help the pads overcome the mechanical hysteresis.

Figure 30 shows the applied load vs. housing displacement for the bearing supplied with 7.8 bara air. For comparison, Figure 30 shows results for both tests (with and without impacts).

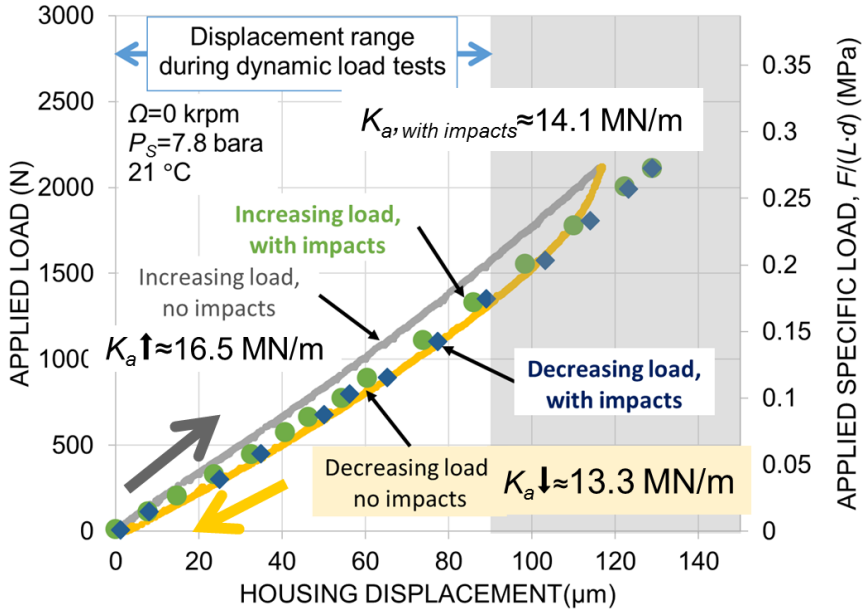

Figure 30: Applied load vs. bearing housing displacement obtained with and without impacts. Air supplied at 7.8 bara. Bearing at room temperature *T*=21˚C. No shaft speed.

Table 4 lists the bearing stiffness (K_a) obtained from each test. The results of the test with impacts between load increments show no mechanical hysteresis, and the bearing stiffness (for housing displacements ranging from 0 μm to 86 μm) equals 14.1± 0.7 MN/m. The stiffness of the room temperature bearing under increasing static load and without impacts is 16.5±0.01 MN/m for housing displacements from 0 μm to 90 μm, and the unload stiffness is 13.3± 0.04 MN/m for housing displacements from 90 μm to 0 μm. The results of the test without impacts show the mechanical hysteresis begins immediately[12] as the bearing (with supply air) displaces.

The results from the test using the original loading procedure are higher than those in Table 3 from an identical experiment. The test with impacts between load increments provides a useful estimate of the bearing stiffness (no mechanical hysteresis) at startup conditions (room temperature bearing, no shaft speed, P_S=7.8 bara).

[12] The bearing with supply air (7.8 bara) shows mechanical hysteresis for all static loads (without impacts between load increments). Note, the pressurized air causes the pads to lift and thus increases the preload on the washer stacks.

Table 4: Comparison of aerostatic bearing stiffness (K_a) obtained from static load tests with and without impacts between load increments for bearing temperature at ~21°C, 7.8 bara supply air and a stationary rotor.

Average Pad Temperature	Supply Air Pressure (P_S)	Stiffness under Increasing Load ($K_a\uparrow$)	Stiffness under Decreasing Load ($K_a\downarrow$)	Impacts Between Load Increments	Maximum Deflection Used in Stiffness Estimate
[°C]	[bara]	[MN/m]	[MN/m]		[μm]
21	7.8	16.5±0.01	13.3±0.04	N/A	90
21	7.8	14.1±0.7		YES	86

3.3 Determination of Bearing Aerostatic Load Capacity and Stiffness vs. Air Supply Pressure (Operation without Shaft Speed)

The next experiments determine the largest static load causing the aerostatic bearing pads to contact the stationary rotor for operation at several air supply pressures. The static load along the *Y* direction increases until the loaded pads contact the rotor; then, the load reduces. At the largest load, the rotor cannot spin freely by hand due to the contact.

Figure 31 shows the applied load (LBP) vs. aerostatic bearing displacement for operation at three supply pressures (P_S = 5.1, 6.4 and 7.8 bara). The bearing load capacity increases with supply pressure. Table 5 lists the derived bearing aerostatic stiffness (K_a) under both increasing and decreasing loads for each supply pressure condition. K_a depends on the load condition (increasing or decreasing). The bearing returned to the initial position for all but one test[13] with the pads supplied with air at 7.8 bara.

[13] These experiments preceded the experiments shown in Figure 24 and Figure 25.

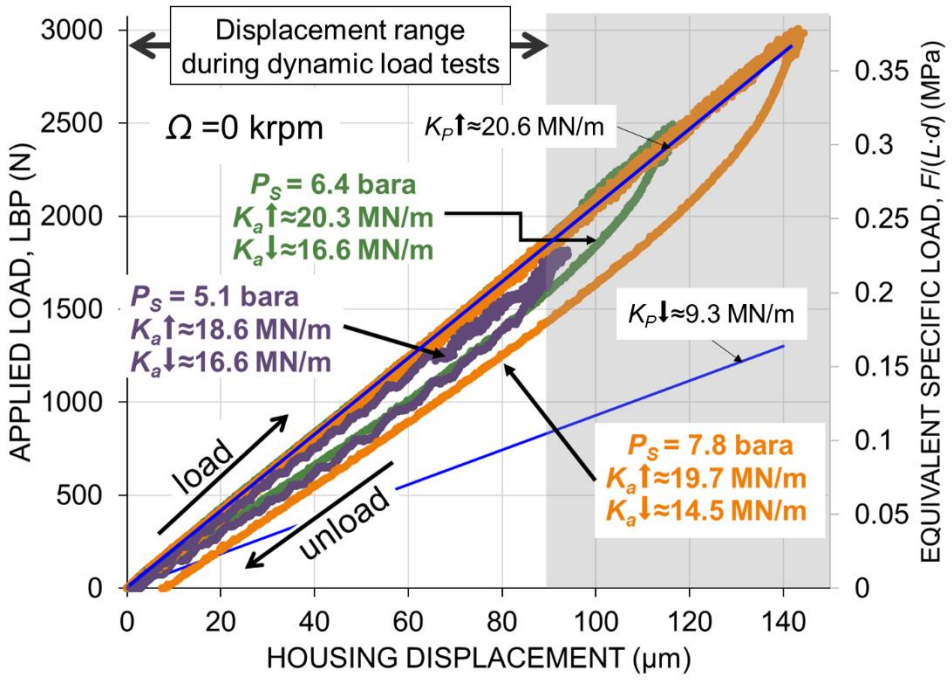

Figure 31: Applied load vs. housing displacement for three air supply pressures (P_S =5.1, 6.4 or 7.8 bara). No shaft speed, room temperature=21°C. Estimated loads derived from pivot stiffness (K_P↑ and K_P↓) included for comparison.

Table 5: Effect of supply pressure on bearing aerostatic stiffness (K_a) under increasing and decreasing static loads for housing displacements up to 90 μm. No shaft speed, room temperature =21°C.

Supply Pressure [bara]	Specific Increasing Load Range [kPa]	Bearing Aerostatic Stiffness (K_a↑) under Increasing Load [MN/m]	Specific Decreasing Load Range [kPa]	Bearing Aerostatic Stiffness (K_a↓) under Decreasing Load [MN/m]
5.1	[0, 223]	18.6 ±0.02	[215, 0]	16.6± 0.05
6.4	[0, 242]	20.3± 0.01	[207, 0]	16.6±0.03
7.8	[0, 236]	19.7± 0.02	[186, 0]	14.5± 0.07

Table 6 summarizes the bearing structure stiffness (K_U) and the bearing aerostatic stiffness (K_a) from static load tests without shaft speed (0 krpm). The bearing structural stiffness (K_U) ranges from 12.0 MN/m to 18.2 MN/m. The bearing aerostatic stiffness (K_a) for 7.8 bara supply air ranges from 10.9 MN/m to 19.7 MN/m. Thus, there is poor repeatability between tests and little difference between the stiffness of the bearing with pressurized air and the bearing underspring stiffness.

Nevertheless, the results of the static load tests (stationary rotor) indicate K_U and K_a are constants that do not depend on the applied static load or displacement.

Table 6: Summary of bearing structure stiffness (K_U) and bearing aerostatic stiffness (K_a) derived from static load tests (no shaft speed)

Average Pad Temperature	Supply Air Pressure (P_S)	Stiffness under Increasing Load ($K\uparrow$)	Stiffness under Decreasing Load ($K\downarrow$)	Maximum Deflection Used in Stiffness Estimate	Comments	Table Number
[°C]	[bara]	[MN/m]	[MN/m]	[μm]		
21		13.3±0.04	12.0±0.05	90	K_U, no shaft speed	2
41		18.2±0.08	15.2±0.19	90		2
41	7.8	15.7±0.04	12.5±0.09	90	K_a, no shaft speed	3
21	7.8	13.4±0.05	10.9±0.11	90		3
21	7.8	16.5±0.01	13.8±0.04	90		4
21	7.8	14.1±0.7		86	K_a, no shaft speed test with impacts	4
21	7.8	19.7±0.03	14.5±0.07	90	K_a, no shaft speed Figure 31	5
21	6.4	20.3±0.01	16.6±0.03	90		5
21	5.1	18.6±0.02	16.6±0.05	90		5

Figure 32 shows the maximum[14] hydrostatically supported load shown in Figure 31 obtained from tests at four air supply pressures. Table 6 includes results of a static load test for a pad supply pressure of 7.1 bara which were omitted in Figure 31 to more clearly distinguish the datasets. Notice the aerostatic load capacity (F_a) is proportional to the product of supply pressure (P_S) and bearing projected area ($L{\cdot}d$) by a constant ratio (η). From the results shown in Figure 32, $\eta \approx 0.58 \pm 0.02$. Results of static load tests with shaft speed detailed later (in Chapter 4) show that the safe bearing load capacity is lesser than F_a when operating with shaft speed.

$$F_a = \eta \cdot (P_S - P_a) \cdot L \cdot d \qquad [1]$$

[14] Static load where the rotor cannot turn by hand due to rotor-pad contact

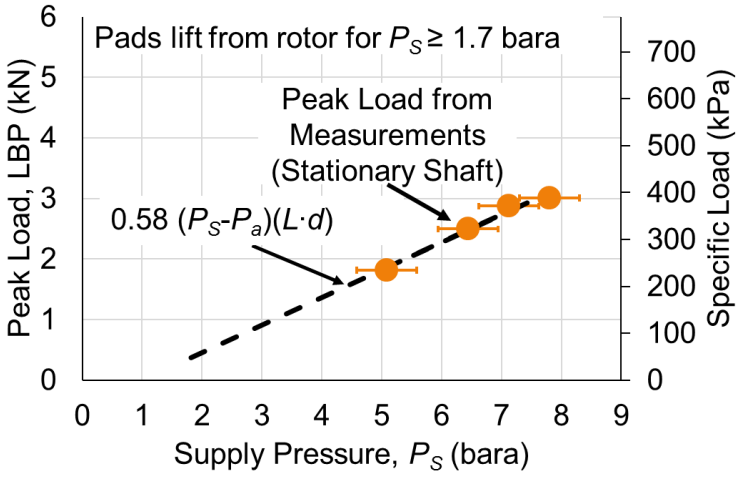

Figure 32: Peak static load (LBP) vs. air supply pressure for bearing operating without shaft speed and at room temperature = 21°C.

Chapter 4: Experiments with Shaft Speed and Static Load

4.1 Static Load Tests

This chapter aims to determine the static load causing a rapid increase in pad temperature when operating with shaft speed (6 krpm, 9 krpm). Upon reaching the desired operating speed, the static load (*Y* direction) increases (~222 N increment) until the loaded pad temperature measurements (discussed next) increase rapidly. The pad temperatures usually recovered and steadied after decreasing the static load by ~222 N.

Table 7 shows the specific static load causing the sudden temperature increase at each operating speed and the maximum specific static load used during dynamic load tests to follow in Chapter 5. The difference between the load causing the rapid temperature increase and the maximum static load for dynamic load tests is larger for the 6 krpm test than that for the 9 krpm test.

Table 7: Bearing static loads causing rapid change in pad temperatures and maximum static loads used in tests described later in Chapter 5 for operation with shaft speed (6 krpm, 9 krpm).

Rotor Speed	**Load Causing Temperature Increase**		**Static Load Selected for Dynamic Load Tests (Chapter 5)**	
(krpm)	Specific Load (kPa)	Load (N)	Specific Load (kPa)	Load (N)
6	172	1335	115	890
9	117	903	101	779

4.2 Bearing Eccentricity and Attitude Angle for Tests with Static Load and Shaft Speed

The bearing "eccentricity" (e) calculates from the measured housing displacements relative to the rotor along each of the X and Y directions (e_X and e_Y, respectively) and equals

$$e = \left(e_X^2 + e_y^2\right)^{0.5} \quad [2]$$

Figure 33 shows the bearing eccentricity (e) vs. specific static load ($F/(L{\cdot}d)$) for operation at shaft speeds of 0 krpm, 6 krpm and 9 krpm. The bearing eccentricity increases with the static load and shows a negligible dependence on shaft speed.

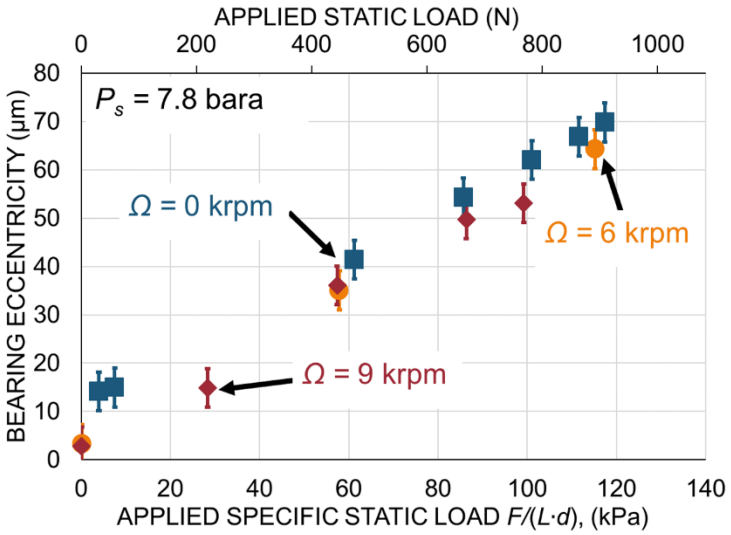

Figure 33: Bearing eccentricity vs. specific static load. Air supply pressure is 7.8 bara and operating speeds include 0 krpm, 6 krpm and 9 krpm.

The bearing attitude angle (φ) is the angle between the static load vector and the bearing eccentricity vector. (Recall that the static load is along the Y direction). Hence,

$$\varphi = \tan^{-1}\left(\frac{e_X}{e_Y}\right) \quad [3]$$

Figure 34 shows the attitude angle vs. specific static load for operation at shaft speeds of 6 krpm and 9 krpm. φ is small (less than ~11˚). Hence, the tilting pad geometry is effective in that there is not a significant cross-coupled displacement of the bearing with respect to the rotor for the applied load and speed conditions. Note, the attitude angle for a low specific load has a high uncertainty because the displacements are very small. Thus, Figure 34 omits those values.

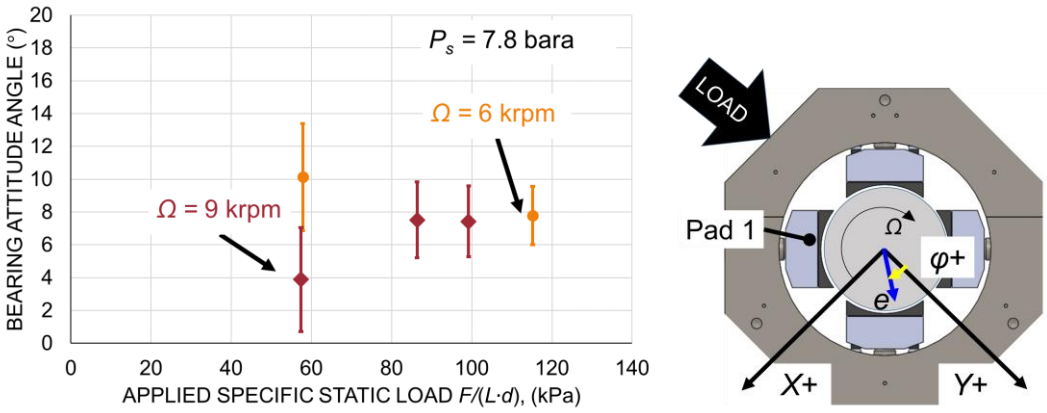

Figure 34: Bearing attitude angle (φ) vs. applied specific static load. Air supply pressure is 7.8 bara and operating shaft speed = 6 krpm, 9 krpm.

The bearing static stiffness (K_S) is the slope of the trend-line fitting the static load (F_S) vs. eccentricity data for the bearing operating with supply air and shaft speed such that

$$F_S = K_S \cdot e \qquad [4]$$

Table 8 lists the bearing static stiffness. The results are comparable to those from the static load tests to identify the bearing aerostatic stiffness[15] K_a from Chapter 3.

[15] Refers to the bearing operating without shaft speed and supplied with air at P_S = 7.8 bara. Recall from Chapter 3 that K_a from the test with impacts is 14.1±0.7 MN/m for a stationary rotor and 7.8 bara supply air.

Table 8: Bearing aerostatic stiffness (K_a) and static stiffness (K_S) for each operating speed from applied load and bearing eccentricity measurements. Air pressure P_S= 7.8 bara into bearing pads.

Operating Speed [krpm]	Static Load Stiffness [MN/m]
0	K_a = 12.6±1.1
6	K_S = 13.1±1.4
9	K_S = 13.2±1.5

4.3 Pad Temperature Measurements

Figure 35 shows a photograph of a thermocouple attached to a pad steel casing (on the non-drive side of a pad face) to measure the pad temperature without interfering with the film.

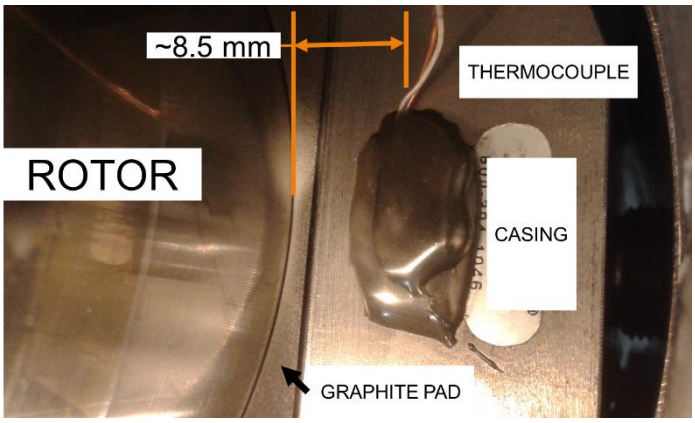

Figure 35: Photograph of thermocouple located on the non-drive face of a pad casing to measure pad temperature

A rapid increase in pad temperature may indicate pad-rotor contact. Figure 36 shows the pad temperature (T) measurements and ambient temperature (T_a) measurements vs. specific load for the upstream-loaded pad (Pad 1) and upstream-unloaded pad (Pad 3) vs. specific load and operating at two shaft speeds, 6 krpm and 9 krpm. Supplying the pads with P_S=7.8 bara air and ensuring the pad temperatures reach an equilibrium state warrants that a film of air separates the pad and rotor surfaces.

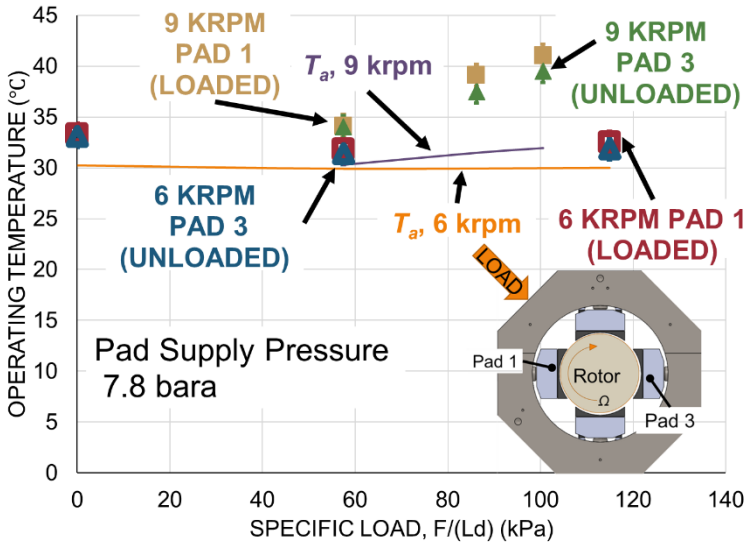

Figure 36: Pad temperature and ambient temperature (T_a) vs. specific load for loaded Pad 1 and unloaded Pad 3 for operation at two shaft speeds (6 krpm, 9 krpm). Inset shows pad locations relative to shaft rotation and load direction

At a single operating speed, the loaded and unloaded pad temperatures show little change with static load. The largest pad temperature change, relative to the pad temperature at 57 kPa static load, is no more than 7°C and occurs for operation at 9 krpm shaft speed. Note in Figure 36 that the ambient temperature increased for the 9 krpm test but was constant (T_a≈30°C) for the 6 krpm test. Differences in temperature between the loaded and unloaded pads are less than the measurement uncertainty (±1 °C). This indicates there is little heat generation due to fluid shear. Recall, however, that the temperature measurements are of the pad side casings, not the carbon-graphite surfaces. A more accurate pad temperature measurement would attach the thermocouple directly under the porous carbon-graphite surface as close to the rotor as possible.

Nevertheless, during testing a rapid increase in pad casing temperatures was still a good indicator of pad-rotor contact that could lead to seizure unless the static load reduced. A continuous pad temperature measurement vs. time was not recorded.

4.4 Pad Vibrations

Figure 37 shows the locations of eddy current sensors monitoring vibrations of Pad 2 and Pad 4. Figure 38 shows a vibration spectrum from eddy current sensor measurements of the back of Pad 4 (leading edge) during a static load experiment with 9 krpm shaft speed and 57 kPa specific static load (load=445 N).

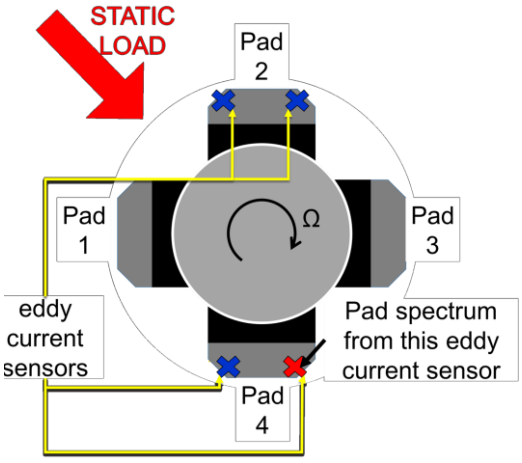

Figure 37: Schematic view of non-drive-side cross-section showing eddy current sensor locations to monitor Pad 2 and Pad 4 vibrations

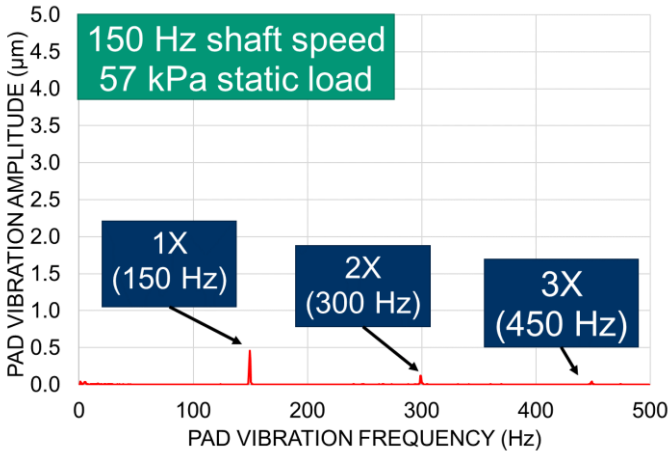

Figure 38: Pad vibration spectrum (Pad 4) for 9 krpm rotor speed and 57 kPa static load, 7.8 bara pad supply pressure

Pad 2 and Pad 4 showed similar spectra throughout the tests, with the largest amplitude of motion at a frequency = shaft speed (1X). As shown in Figure 38, the pad vibration amplitudes are small, far below the measurement uncertainty (±1 μm) of the eddy current sensors.

4.5 Pad Tilt

Figure 39 shows a schematic of a pad and pivot to illustrate the estimation of a pad tilt angle (δ) from the two eddy current sensors (ECS) measuring the pad location relative to the bearing housing upstream (S_1) and downstream (S_2) of the pivot. Recall that the pads have elastic supports (Belleville washer stacks). Thus, a load can cause the pivot to deflect.

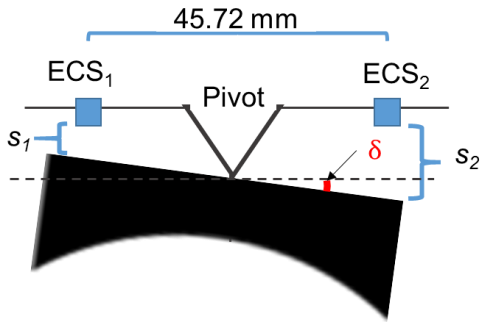

Figure 39: Schematic of pad cross-section and pivot to determine pad tilt angle from measurements S_1 and S_2 from two eddy current sensors (ECS) spaced 45.72 mm apart.

Figure 40 shows the measured "tilt displacements" (S_1 and S_2), for Pad 2 and Figure 41 shows S_1 and S_2 for Pad 4 while the bearing operates at 6 krpm and 9 krpm shaft speed. The baseline for the pad displacements is the pad location when supplied 7.8 bara air and without surface speed (0 krpm). A negative tilt displacement indicates motion towards the rotor relative to the baseline. A positive displacement indicates motion away from the rotor. At the largest eccentricity ($e \approx 64$ μm) for operation with shaft speed, the leading edge of unloaded Pad 4 displaces towards the rotor more than it lifted during assembly (23 μm). However, there was not pad rotor contact because the bearing eccentricity increases the gap between this pad and the rotor.

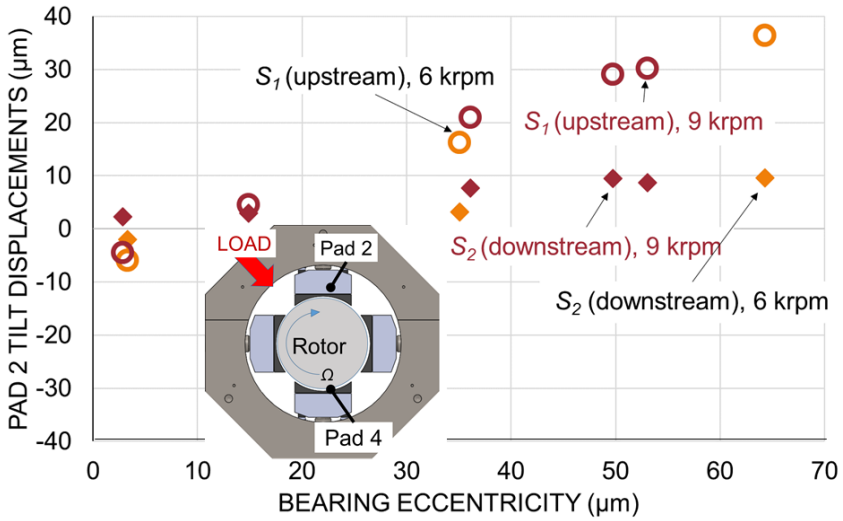

Figure 40: Pad 2 tilt displacements S_1 and S_2 vs. bearing eccentricity (e) for operation at 6 krpm and 9 krpm.

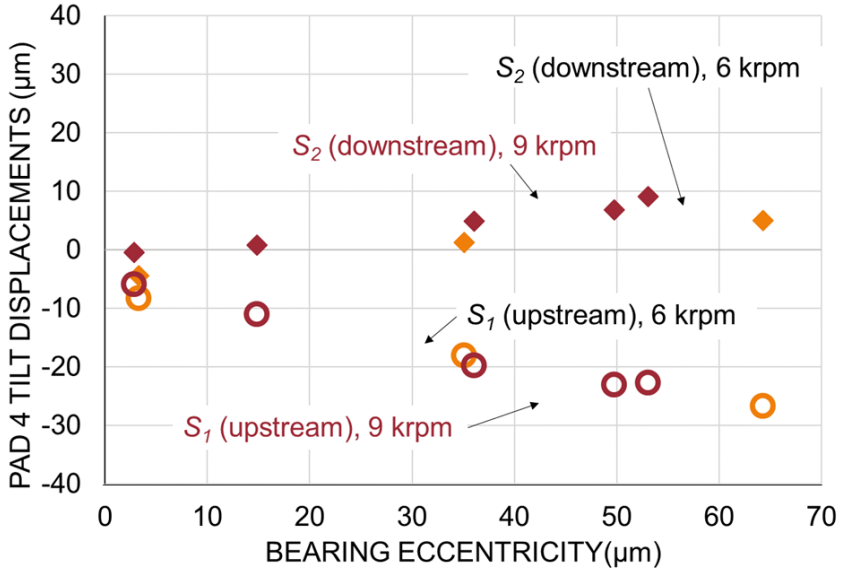

Figure 41: Pad 4 tilt displacements S_1 and S_2 vs. bearing eccentricity (e) for operation at 6 krpm and 9 krpm.

The pad tilt angle is

$$\delta = \tan^{-1}\left(\frac{S_2 - S_1}{45.72\ \text{mm}}\right) \approx \frac{S_2 - S_1}{45.72\ \text{mm}} \quad [5]$$

The effective tilt displacement (S_{LE}) at the pad leading edge is

$$S_{LE} = R_{PAD} \cdot \delta \cdot \sin\left(\frac{\Theta_P}{2}\right) \quad [6]$$

with pad tilt angle (δ), pad radius (R_{PAD}), pad arc length (Θ_P) and measured tilt displacements (S_1, S_2). The effective tilt displacement (S_{TE}) at the pad trailing edge equals -S_{LE}.

Figure 42 shows the effective tilt displacements at the leading edge (S_{LE}) of Pad 2 (loaded) and Pad 4 (unloaded) for operation with shaft speed equal to 0 krpm, 6 krpm and 9 krpm. The leading edge of Pad 4 tilts towards the rotor, while the leading edge of Pad 2 tilts away from the rotor as the static load on Pad 4 decreases and the static load on Pad 2 increases. The motion of the loaded pad (Pad 2) shows no shaft speed dependency and the edge displacements for the steady state static load tests with shaft speed do not exceed 23 µm in magnitude. The magnitude of S_{LE} for the unloaded pad (Pad 4) increases slightly with shaft speed.

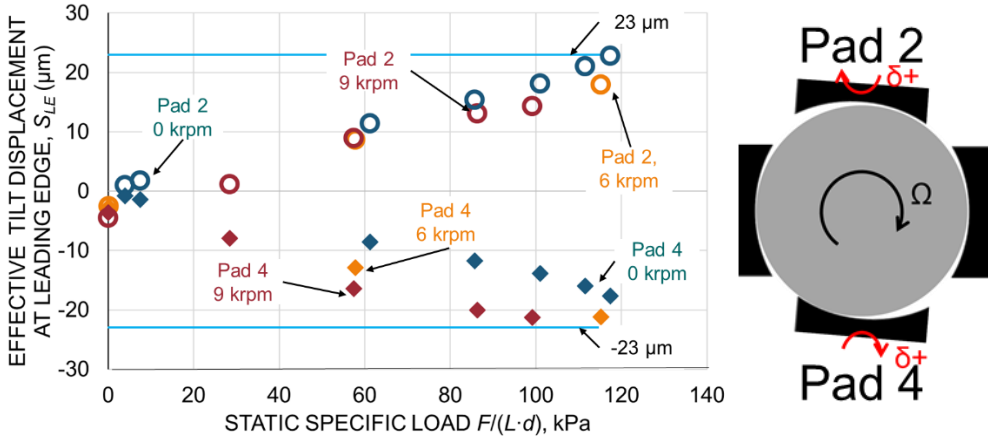

Figure 42: Pad 2 and Pad 4 effective tilt displacement at leading edge (S_{LE}) vs. static specific load for 0 krpm, 6 krpm and 9 krpm rotor speeds (7.8 bara pad supply pressure). Schematic view shows positive tilt angles.

Chapter 5: Experiments with Shaft Speed, Static Load and Dynamic Loads to Estimate Bearing Force Coefficients

5.1 Bearing Dynamic Stiffness[16]

Lund (1968) [25] derived a means to model the reaction forces generated by a tilting-pad gas bearing due to a small perturbation of the rotor from an equilibrium position by calculating equivalent bearing coefficients that characterize the bearing stiffness and damping force coefficients. Bearing force coefficients enable rotordynamic analyses of rotor stability, synchronous rotor response and natural frequency predictions.

Results of experiments, for example those in Ref. [26], to determine a gas bearing frequency response show a reduced order model can sufficiently quantify a tilting-pad type gas bearing reaction to dynamic loads.

The equation of motion along each of two directions (X and Y) of the test bearing under a dynamic load sets the sum of the applied excitation force ($\boldsymbol{F}$) and the test bearing reaction force ($\boldsymbol{F_t}$) equal to the product of the bearing mass (M) and bearing acceleration ($\boldsymbol{a}$) [26].

$$\boldsymbol{F} + \boldsymbol{F_t} = M \cdot \boldsymbol{a} \qquad [7]$$

The bearing is assumed as a linear system with stiffness ($\boldsymbol{K}$) and damping ($\boldsymbol{C}$) coefficients [25]. Thus, the reaction force $\boldsymbol{F_t}$ due to a small amplitude displacement ($\boldsymbol{D}=\begin{Bmatrix} D_X \\ D_Y \end{Bmatrix}$) from an equilibrium rotor position within the bearing bore is modeled as

$$\boldsymbol{F_t} = -\begin{bmatrix} K_{XX} & K_{XY} \\ K_{YX} & K_{YY} \end{bmatrix}\begin{Bmatrix} D_X \\ D_Y \end{Bmatrix} - \begin{bmatrix} C_{XX} & C_{XY} \\ C_{YX} & C_{YY} \end{bmatrix} \cdot \frac{d}{dt}\begin{Bmatrix} D_X \\ D_Y \end{Bmatrix} \qquad [8]$$

[16] The derivation of the equation of motion and use of a frequency domain analysis originates from Refs. [26-27].

where subscript *XY* represents a reaction force along the *X* direction due to rotor-bearing relative motion in the *Y* direction.

In the frequency domain, a complex dynamic stiffness (***H***) characterizes a bearing when the rotor[17] undergoes a small displacement from an equilibrium position and at a particular excitation frequency, (ω) [27]. The real part of ***H*** indicates the bearing dynamic stiffness, while the imaginary part is a quadrature stiffness and proportional to the bearing damping [26].

$$\boldsymbol{H}(\omega) = \boldsymbol{K}(\omega) + i\boldsymbol{C}(\omega) \cdot \omega \qquad [9]$$

The force equations for equilibrium (in the frequency domain) become

$$\begin{Bmatrix} F_X - M \cdot a_X \\ F_Y - M \cdot a_Y \end{Bmatrix} = \begin{Bmatrix} H_{XX} & H_{XY} \\ H_{YX} & H_{YY} \end{Bmatrix} \begin{Bmatrix} D_X \\ D_Y \end{Bmatrix} \qquad [10]$$

To solve Equation (10) for the four unknown complex dynamic stiffnesses (H_{XX}, H_{XY}, H_{YX}, H_{YY}), it is necessary to separately excite the bearing along two independent directions (1, then 2) to form a nonsingular displacement matrix [$\boldsymbol{D_1}$ $\boldsymbol{D_2}$].

In the component-level experiments herein, the test bearing is a nonstructural member. This setup enables tests over a range of static loads and the application of dynamic loads at multiple nonsynchronous speed excitation frequencies. The dynamic load experiments provide measurements of the applied loads (dynamic and static), the test bearing system accelerations, and the bearing displacements relative to the rotor.

During a dynamic load test, a virtual instrument records 327,680 data points per independent excitation for each instrument channel. A MATLAB® function divides the recorded measurements into n_s (n_s=16) sets. For analysis, a discrete Fourier transform converts the time

[17] For the component level tests described herein, the housing displaces from an equilibrium position instead of the spinning rotor. External shakers provide both the static and dynamic loads.

domain measurement of forces (F), housing displacements (D) relative to rotor, and housing absolute accelerations (a) into the frequency domain.

Transferring the time-domain measurements for two independent excitations to the frequency domain with a Fourier transform enables the estimation of the bearing dynamic stiffness at a particular excitation frequency as

$$\begin{Bmatrix} H_{XX} & H_{XY} \\ H_{YX} & H_{YY} \end{Bmatrix} = \begin{Bmatrix} F_{X1} - Ma_{X1} & F_{X2} - Ma_{X2} \\ F_{Y1} - Ma_{Y1} & F_{Y2} - Ma_{Y2} \end{Bmatrix} \begin{Bmatrix} D_{X1} & D_{X2} \\ D_{Y1} & D_{Y2} \end{Bmatrix}^{-1} \quad [11]$$

5.2 Baseline Dynamic Load Test

First, it is necessary to conduct a baseline dynamic load experiment to quantify the dynamic stiffness ($\boldsymbol{H_b}$) of the test rig attachments (e.g. pitch stabilizers, instrument wiring) for subtraction from the test results. Appendix B details the test setup and results. At the lowest frequency (ω=9.7 Hz), H_{bXX}= (0.47+$\mathbf{i}$0.01) MN/m and H_{bYY} =(0.40+ $\mathbf{i}$0.07) MN/m.

5.3 Dynamic Load Tests

Herein are results of dynamic load experiments to identify the dynamic force coefficients of the test bearing for excitation over a range of frequencies. The shaft surface speeds are 0 m/s, 32 m/s (6 krpm [100 Hz]) and 48 m/s (9 krpm [150 Hz]). Table 9 lists the shaft speed and specific static load $\left(\frac{F}{L \cdot d}\right)$ combinations for the test bearing. The pads receive 7.8 bara air during all of the dynamic load tests. The applied specific static loads differ between the two shaft speeds because the bearing load capacity with shaft speed was much less than the aerostatic loads presented in Chapter 3, and the tests at 6 krpm preceded those at 9 krpm. Thus, there was not a means to predict the load capacity with shaft speed.

Table 9: Specific static load $F/(L \cdot d)$ and shaft speed for dynamic load experiments

Load Case (LBP)	No Speed	Speed 1 (6 krpm)	Speed 2 (9 krpm)
No Load	0 kPa	0 kPa (0 N)	N/A
Specific Load 1	N/A	57 kPa (445 N)	57 kPa (445 N)
		N/A (*)	86 kPa (668 N)
		115 kPa (890 N)	101 kPa (779 N)

** Did not conduct dynamic test at comparable specific load.*

5.3.1 Dynamic Load Test Procedure

A dynamic load experiment begins once the bearing pad temperatures steady during operation at a particular shaft speed and under a specific static load. A data acquisition unit collects the measured excitation forces, housing displacements, and housing accelerations. Using a shaker to excite the bearing along each of two orthogonal directions (X and Y) yields two independent data sets to determine all four complex dynamic stiffnesses (H_{XX}, H_{XY}, H_{YX}, and H_{YY}).

Excitations along the X and Y directions use the same waveform containing 34 frequencies that range from 9.7 Hz to 341.8 Hz in 9.7 Hz increments. The waveform is a pseudo-random excitation as described by Childs and Hale in Ref. [28]. Note that the maximum excitation frequency is ~2.3 times the top operating shaft speed (150 Hz). The maximum dynamic force amplitudes range from 76 N to 184 N[18], which are approximately 9%-21% of the maximum static load applied (~890 N) but a sizeable portion of the 445 N static load. The peak bearing displacements range from 4 μm to 8 μm. Recall from Chapter 1 that the pads lift ~23 μm from the stationary rotor when supplied with 7.8 bara air. Hence, the amplitudes of motion are small in comparison. Recall that a linear force model only applies for small amplitude displacements.

[18] The load cells are the primary contributors to the bias error in the complex bearing dynamic stiffness. See Appendix D.

Appendix C shows the bearing cross-coupled dynamic stiffness are small in magnitude and have poor coherence. Thus, the analysis further neglects the cross-coupled measurements and decouples the dynamic stiffness matrix in Equation (11).

The direct complex dynamic stiffnesses of the system,[19] ($\boldsymbol{h_{XX}}, \boldsymbol{h_{YY}}$) from one set of $\boldsymbol{F}$, $\boldsymbol{D}$ and $\boldsymbol{a}$ measurements along the *X* and *Y* directions, follows as

$$\boldsymbol{h_{XX}} = \frac{\boldsymbol{F_X} - M \cdot \boldsymbol{a_X}}{\boldsymbol{D_X}} \quad \text{and} \quad \boldsymbol{h_{YY}} = \frac{\boldsymbol{F_Y} - M \cdot \boldsymbol{a_Y}}{\boldsymbol{D_Y}} \qquad [12]$$

The bearing complex stiffness (H) for each excitation frequency (ω) is the average of n_s dynamic stiffness (h) values along that direction minus the average baseline dynamic stiffness

$$H_{ii} = \frac{1}{n_s}\sum_{1}^{n_s} h_{ii} - \left(\frac{1}{n_s}\sum_{1}^{n_s} h_{ii}\right)_b \qquad ii = \{XX, YY\} \qquad [13]$$

5.3.2 Bearing Dynamic Stiffness Results

Figures 43, 44 and 45 show for the load cases listed in Table 9, the real part of the bearing complex dynamic stiffness, H_{XX} and H_{YY}, vs. excitation frequency (ω) for operation at shaft speeds of 0 krpm, 6 krpm (32 m/s) and 9 krpm (48 m/s), respectively. Note the pads receive P_S=7.8 bara air during the tests. The real parts of the complex dynamic stiffnesses (H_{XX} and H_{YY}) increase with static load and do not depend on the excitation frequency. Moreover, the coefficients are nearly isotropic (i.e. $H_{XX} \cong H_{YY}$) because the pads are symmetric about the static load direction [25].

[19] includes the baseline dynamic stiffness

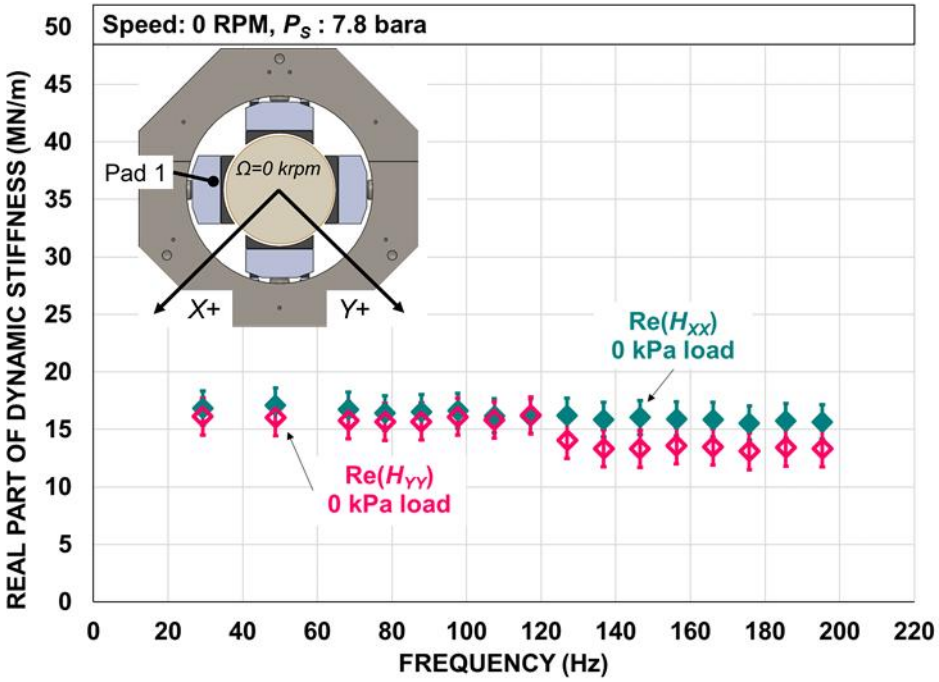

Figure 43: Real part of bearing complex dynamic bearing stiffnesses (H_{XX}, H_{YY}) vs. excitation frequency. Operating shaft speed = 0 krpm and static specific load = 0 kPa (P_S = 7.8 bara).

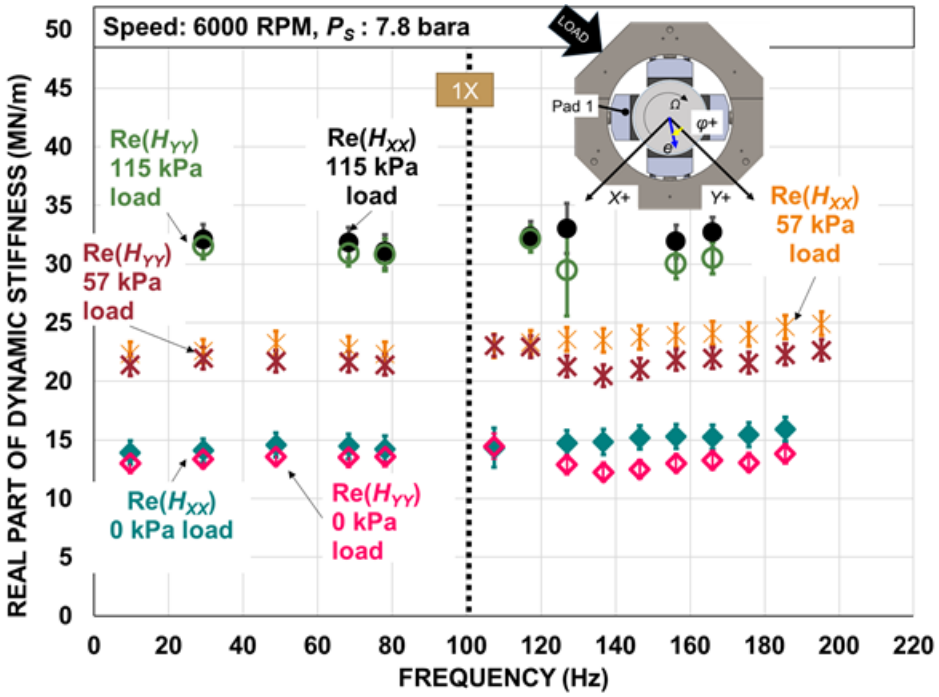

Figure 44: Real part of bearing complex dynamic bearing stiffnesses (H_{XX}, H_{YY}) vs. excitation frequency. Operating shaft speed = 6 krpm and static specific loads = 0 kPa, 57 kPa and 115 kPa (P_S = 7.8 bara).

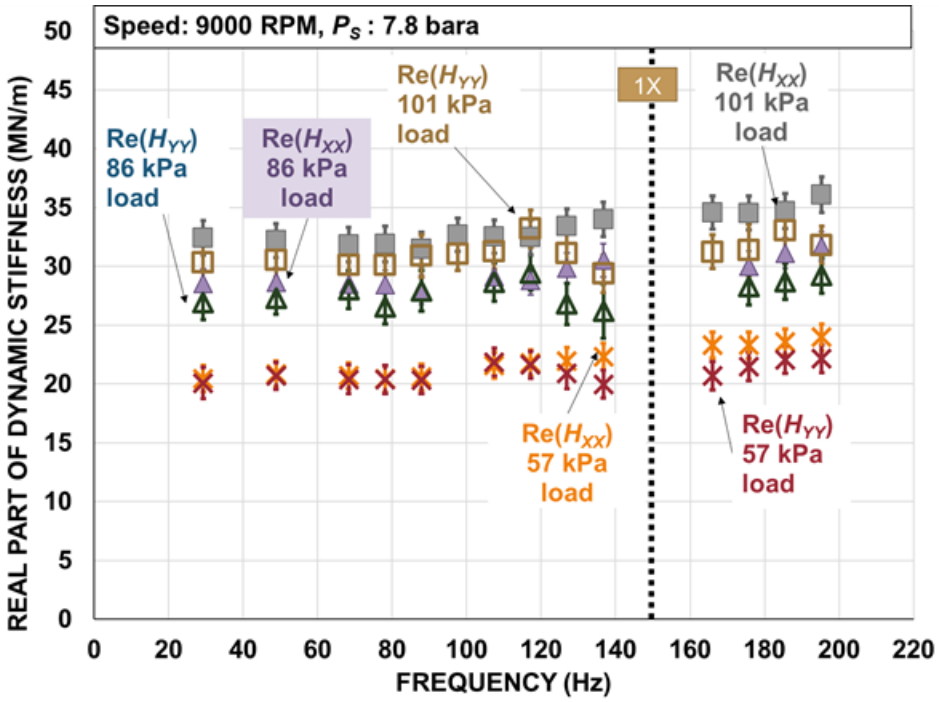

Figure 45: Real part of bearing complex dynamic bearing stiffnesses (H_{XX}, H_{YY}) vs. excitation frequency. Operating shaft speed = 9 krpm and static specific loads = 57 kPa, 86 kPa and 101 kPa (P_S = 7.8 bara).

Recall from Equation (9) that the real part of a complex dynamic stiffness produces the bearing dynamic stiffness coefficient. Table 10 lists the range of the real part of H_{XX} and H_{YY} from Figures 43, 44 and 45. Under 0 kPa or 57 kPa static load, Re(H) hardly changes due to shaft speed. The bearing stiffness increases more rapidly with static load when operating at the higher (9 krpm) surface speed than at the lower (6 krpm) operating speed.

Table 10: Maximum and minimum of the real part of the bearing complex dynamic stiffnesses (H_{XX}, H_{YY}) from Figures 43, 44 and 45.

			Static Load				
			0 N	445 N	668 N	779 N	890 N
			0 kPa	57 kPa	86 kPa	101 kPa	115 kPa
Rotor Speed	0 krpm	K_a (MN/m)	12.7 ± 0.6				
		$Re(H_{XX})$ (MN/m)	15.6-17.1				
		$Re(H_{YY})$ (MN/m)	13.1-16.2				
	6 krpm	K_S (MN/m)	13.3 ± 1.2				
		$Re(H_{XX})$ (MN/m)	13.9-15.9	22.4-24.9			31.0-33.0
		$Re(H_{YY})$ (MN/m)	12.3-14.5	20.5-22.9			29.5-32.1
	9 krpm	K_S (MN/m)	13.3 ± 1.6				
		$Re(H_{XX})$ (MN/m)		20.4-24.0	28.0-31.7	31.5-36.1	
		$Re(H_{YY})$ (MN/m)		20.0-22.1	26.2-29.4	29.4-33.2	

Since the real parts of the complex dynamic stiffness do not change significantly (variation of less than 5 MN/m) with frequency, let the bearing direct stiffness coefficient (K_{ii}) be the average of all the real components of $H_{ii}(\omega)$ for excitation frequencies up to just above synchronous speed.

$$K_{ii} = \frac{1}{n}\sum Re(H_{ii}(\omega)),\ i=\{x, y\} \qquad [14]$$

Figure 46 shows the bearing stiffness coefficients (K_{XX} and K_{YY}) bara versus specific static load for operation with supply air pressure P_S =7.8 bara and at shaft speeds of 0 krpm, 6 krpm and 9 krpm. Figure 45 also includes the bearing static stiffness (K_S) and the bearing aerostatic stiffness (K_a) at $T \approx 21$°C as references.

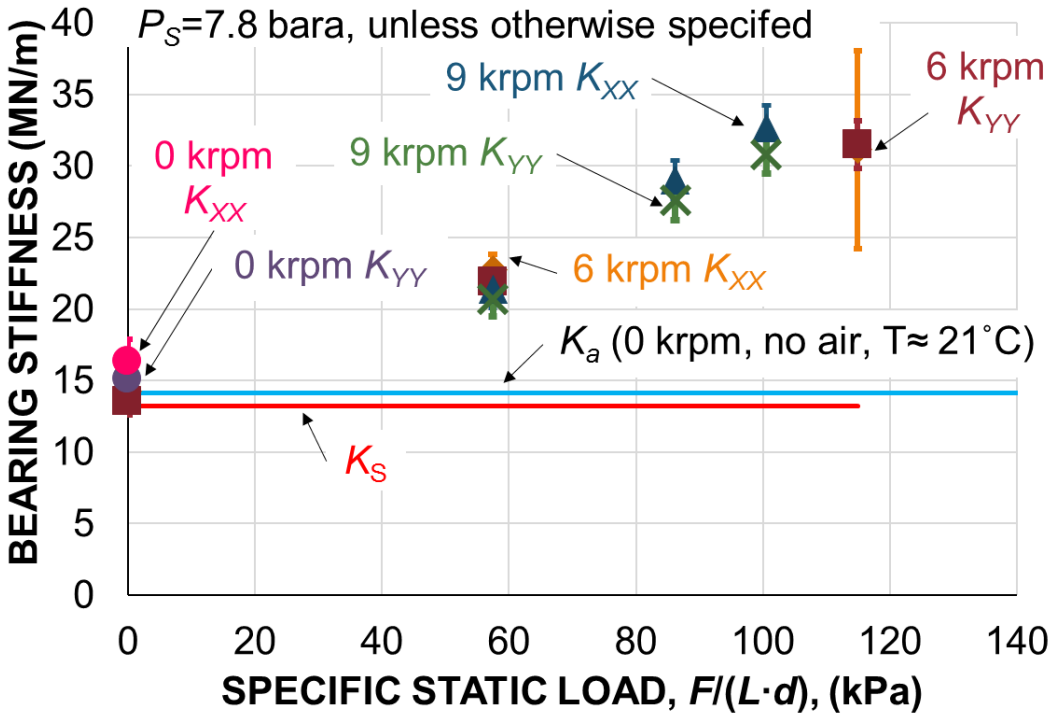

Figure 46: Bearing stiffness coefficients (K_{XX}, K_{YY}) vs. static specific load. Operation at shaft speed = 0 krpm, 6 krpm and 9 krpm. P_S=7.8 bara. Bearing aerostatic stiffness (K_a) and static stiffness (K_S) provided for reference. Bearing temperatures are those of Figure 36.

Figure 46 demonstrates that the bearing direct stiffness from the dynamic load tests increases with the static load and shows a negligible shaft speed dependency. The bearing static stiffness (K_S) and bearing aerostatic stiffness (K_a) agree with the bearing stiffnesses (K_{XX}, K_{YY}) from the dynamic load tests for the lowest load (0 kPa). K_S and K_a are constant over the range of static loads and derive from experiments with similar test procedures (differing only in whether there is shaft speed).

In sum, the bearing stiffnesses from the dynamic load tests increase with static load, while the bearing stiffnesses (K_a and K_S) from the static load tests are constant. Rationale for the noted difference is unknown.

Figures 47, 48 and 49 show the imaginary components of H_{XX}, H_{YY} vs. excitation frequency for shaft speeds = 0 krpm, 6 krpm and 9 krpm, respectively. Results demonstrate that Im(H) is proportional to excitation frequency. The error bars indicate the total uncertainty of the imaginary components of H and thus accounts for both the precision error and the bias error. The magnitudes of Im(H) are quite small relative to those of Re(H); hence, the uncertainty is high in comparison.

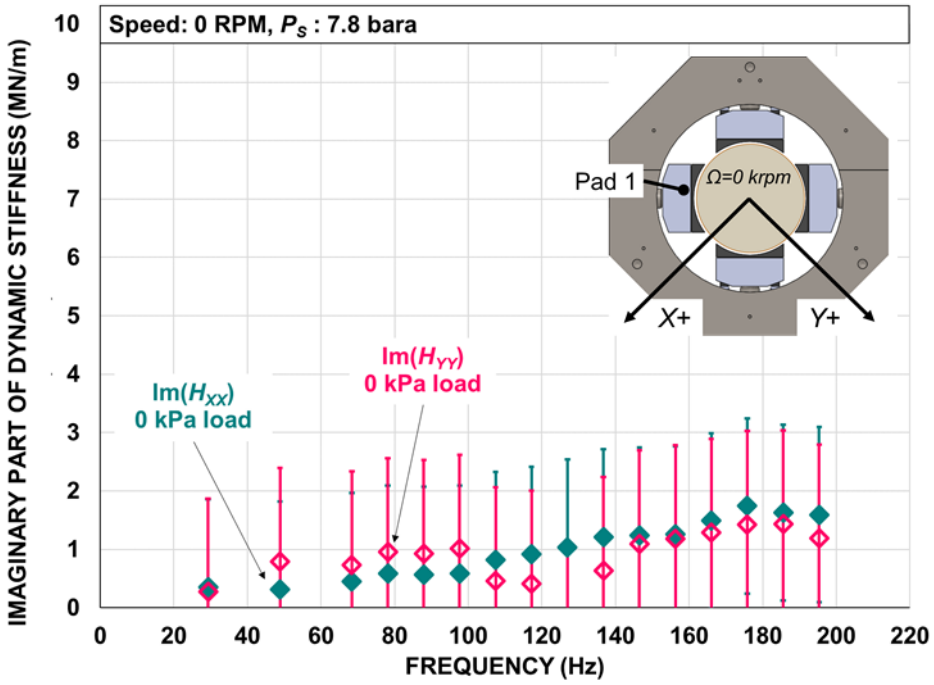

Figure 47: Imaginary part of complex dynamic bearing stiffnesses (H_{XX}, H_{YY}) vs. excitation frequency. Operating shaft speed = 0 krpm, static specific load = 0 kPa (P_S = 7.8 bara).

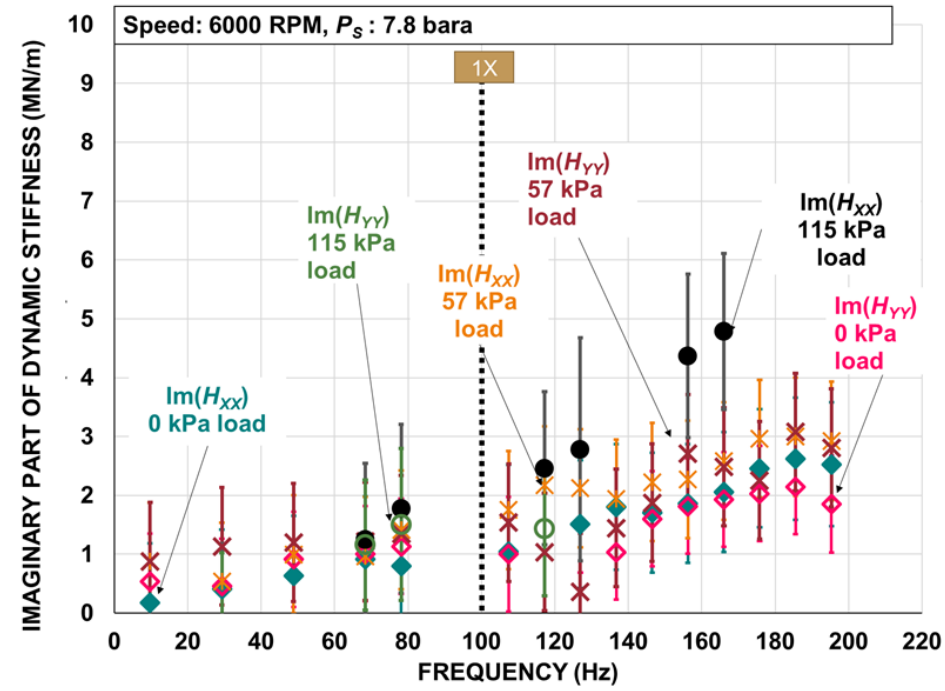

Figure 48: Imaginary part of complex dynamic bearing stiffnesses (H_{XX}, H_{YY}) vs. excitation frequency. Operating shaft speed = 6 krpm, static specific loads = 0 kPa, 57 kPa and 115 kPa (P_S = 7.8 bara).

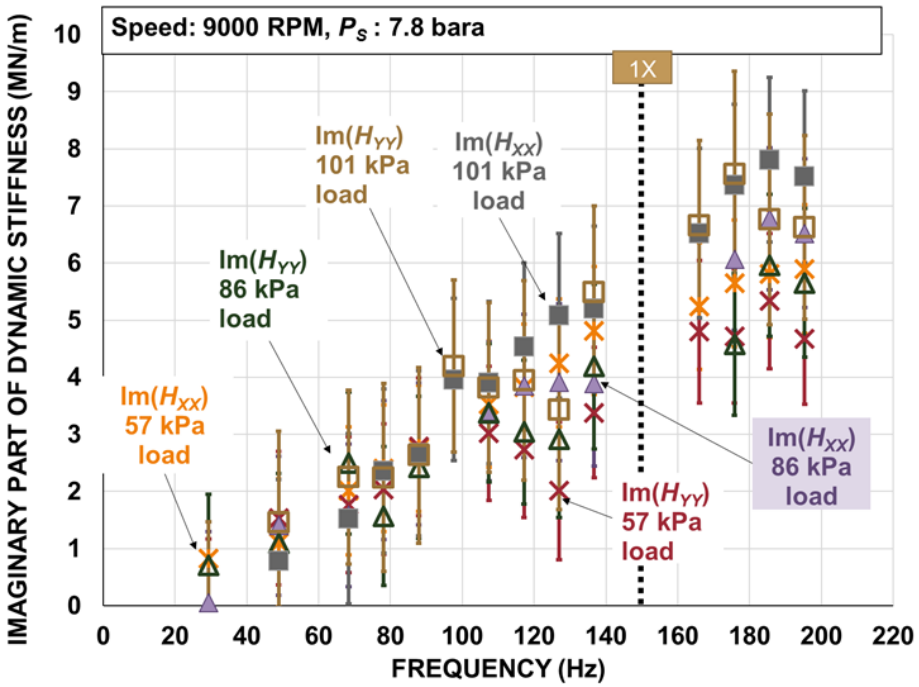

Figure 49: Imaginary part of complex dynamic bearing stiffnesses (H_{XX}, H_{YY}) vs. excitation frequency. Operating shaft speed = 9 krpm, static specific loads = 57 kPa, 86 kPa and 101 kPa (P_S = 7.8 bara).

Let g represent the ratio of the imaginary component of the bearing dynamic stiffness to the real component.

$$g = \frac{Im(H)}{Re(H)} \qquad [15]$$

Figures 50, 51 and 52 plot g vs. excitation frequency (ω) for the tests with the bearing at an operating shaft speed = 0 krpm, 6 krpm and 9 krpm, respectively.

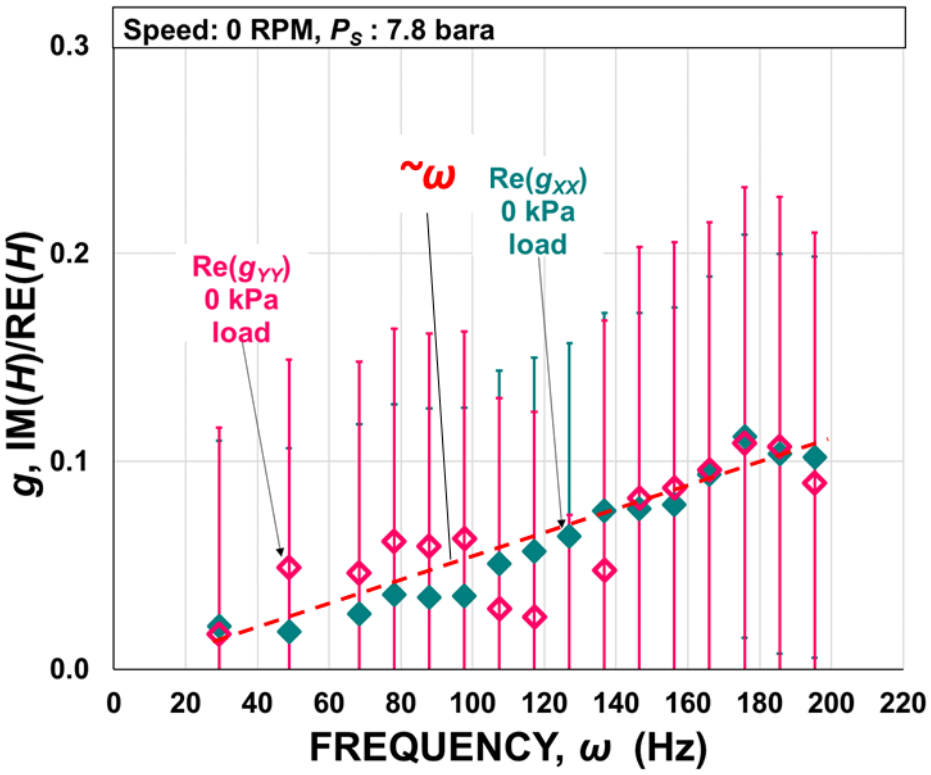

Figure 50: Ratio of imaginary part to real part of complex dynamic bearing stiffnesses (H_{XX}, H_{YY}) vs. excitation frequency. Operating shaft speed = 0 krpm, static specific load = 0 kPa (P_S = 7.8 bara).

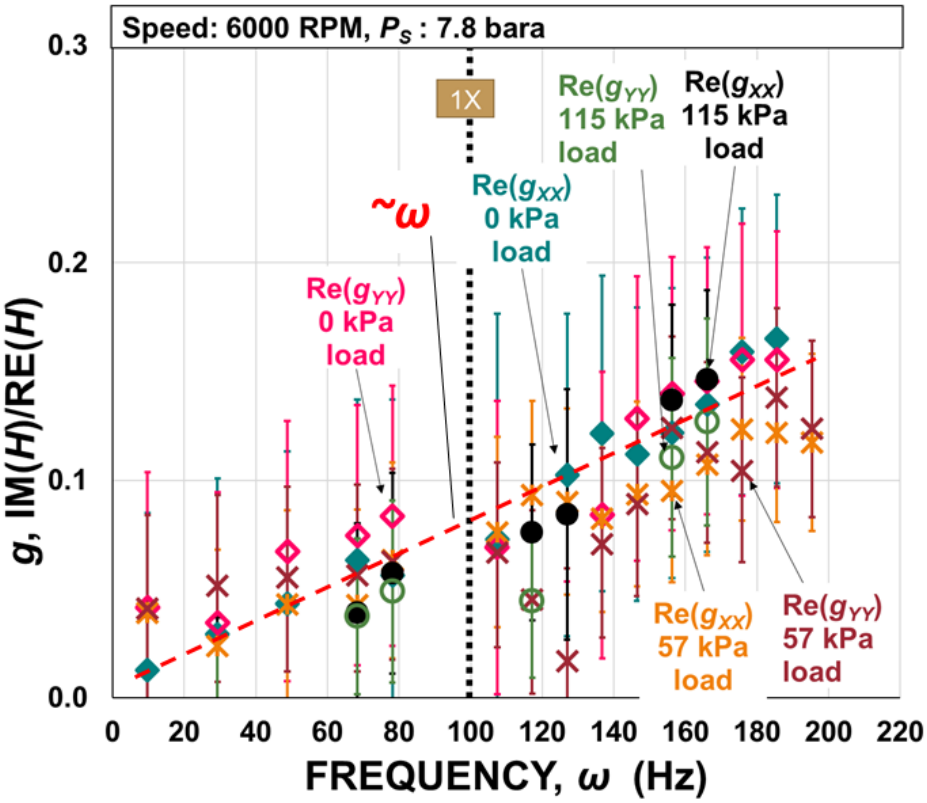

Figure 51: Ratio of imaginary part to real part of complex dynamic bearing stiffnesses (H_{XX}, H_{YY}) vs. excitation frequency. Operating shaft speed = 6 krpm, static specific loads = 0 kPa, 57 kPa and 115 kPa (P_S = 7.8 bara).

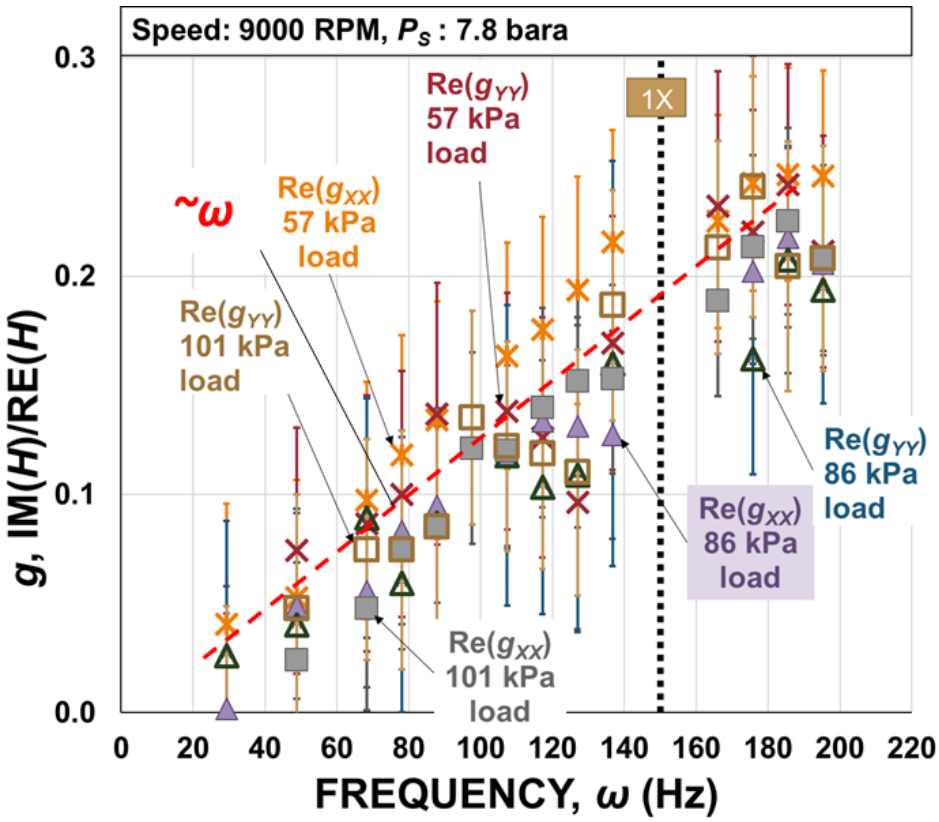

Figure 52: Ratio of imaginary part to real part of complex dynamic bearing stiffnesses (H_{XX}, H_{YY}) vs. excitation frequency. Operating shaft speed = 9 krpm, static specific loads = 57 kPa, 86 kPa and 101 kPa (P_S = 7.8 bara).

For the data shown in Figures 50, 51 and 52, Im(H) is less than 0.25 of Re(H), and g scales proportionally to the excitation frequency up to about 180 Hz. Therefore, frequency-independent force coefficients (K and C) do characterize the test bearing. If the damping was primarily Coulomb damping (due to the friction in the pad supports), its equivalent viscous damping coefficient should decrease with excitation frequency (e.g. Ref. [26]). Since the damping coefficient is frequency independent, the bearing damping is primarily viscous-type, not dry friction-type.

The bearing damping coefficient is the slope of the line fitting the imaginary components of the bearing dynamic stiffness Ima(H) vs. the frequency (to just above synchronous) for an operating condition (speed and static specific load). Figure 53 shows the bearing damping

coefficients (C_{XX} and C_{YY}) vs. static load for operation with shaft speed at 0 krpm, 6 krpm and 9 krpm. C_{XX} and C_{YY} increase slightly with both load and shaft speed. In general, the damping magnitudes are less than 5.8 kN·s/m.

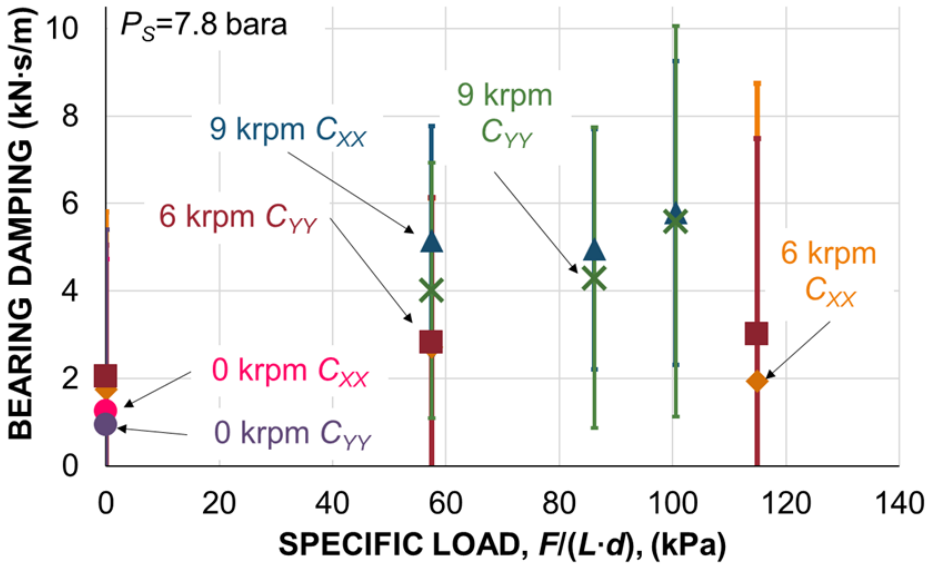

Figure 53: Bearing damping (C_{XX}, C_{YY}) vs. specific load. Operation at shaft speed = 0 krpm, 6 krpm and 9 krpm. P_S=7.8 bara.

5.4 Post-Test Inspection of Bearing Pads

During tests with shaft speed, the eddy current sensors monitoring the back of two pads indicated that at steady state conditions the leading edge of Pad 4 tilted toward the rotor. Figure 54 shows the condition of the pads after removal from the test rig. Upon disassembly, the leading edges of all four pads showed some wear. However, the loaded pads (Pads 1 and 2) showed more wear than the unloaded pads (Pads 3 and 4). Recall that for the steady state conditions shown in Chapter 4, the equivalent tilt displacements at the leading edges of both Pad 2 and Pad 4 did not indicate pad-rotor contact. Thus, the wear did not occur under those conditions.

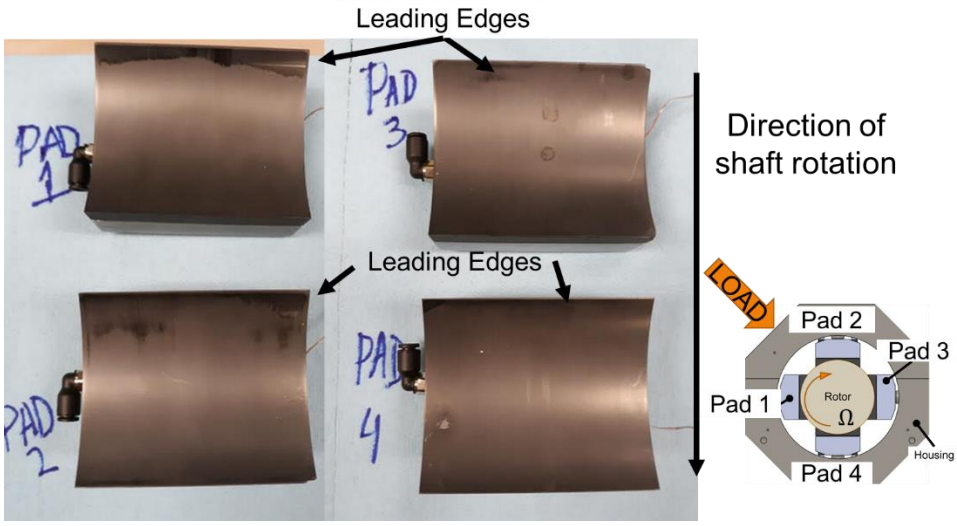

Figure 54: Condition of pads after operation with speed and static load.

Conclusion

Hydrostatic gas journal bearings with porous tilting pads enable shaft support with low drag power losses, no risk of process fluid contamination and with an enhanced stability compared to fixed geometry bearings [29]. This report characterizes the static and dynamic load performance of a radial gas bearing (ID 101.6 mm) with four porous Carbon tilting pads and elastic supports, i.e. Belleville washers (BW) on spherical pivots.

In Chapter 1, a static load experiment on a pivot in contact with two nested BWs characterizes a pad support stiffness (K_P). K_P is 20.6±2.2 MN/m during loading and 9.3±1.9 MN/m during unloading. The differences are due to dry friction at the pivot-washer interface.

Chapter 2 details static load experiments to determine the structure stiffness (K_U) of the assembled bearing. Results show a slight mechanical hysteresis and that K_U changes with pad temperature. At a pad operating temperature (T) of 41°C and ambient temperature (T_a) of ~32°C, K_U is 18.2±0.08 MN/m for increasing load and 15.2±0.19 MN/m for decreasing load. Chapter 3 experiments determine the aerostatic stiffness K_a=14.1±0.7 MN/m of the bearing operating with supply air and no shaft speed. The bearing hydrostatic load capacity (stationary rotor) increases with the gas supply pressure to the pads and equals 58% of the pressure difference (supply-ambient) times the projected bearing area ($L \cdot d$).

In Chapter 4, static load experiments on the bearing operating at shaft speed = 6 krpm and 9 krpm and supplied 7.8 bara air determine static load capacity, bearing eccentricity, attitude angle, static stiffness and pad temperatures. Upon operation with shaft speed, and to avoid pad-rotor contact, there is a significant decrease in load capacity to ~43% of the hydrostatic load (~172 kPa at 6 krpm and ~117 kPa at 9 krpm). Bearing eccentricity increases with static load and is independent of shaft speed. The attitude angle is less than 11˚. The test bearing static stiffness K_S

≈13.1±1.4 MN/m (75 klb_f/in). Pad temperatures from steady state static load tests range from 31°C to 34°C at 6 krpm shaft speed, and from 34°C to 41°C at 9 krpm shaft speed. The increase in pad temperature with shaft speed is due to an increased ambient temperature.

Chapter 5 details dynamic load (LBP) experiments on the bearing during operation with shaft speed at 0 krpm, 6 krpm and 9 krpm. For the tests with shaft speed (6 krpm, 9 krpm), the maximum specific static loads are 115 kPa and 101 kPa, respectively. The ratio of the imaginary to the real components of the complex dynamic bearing stiffnesses linearly increases with excitation frequency, indicating that frequency-independent stiffness and damping coefficients (K, C) model best the test bearing dynamic forced response. Cross-coupled dynamic bearing stiffnesses are low in magnitude and show poor coherence. The bearing direct stiffness coefficients (K_{XX}, K_{YY}) are independent of shaft speed and increase with static load from 13.6±1.0 MN/m to 32.7±1.5 MN/m (186±9 klb_f/in). The bearing stiffnesses (K_{XX}, K_{YY}) from the dynamic load tests increase with static load, while the bearing stiffnesses (K_a and K_S) from the static load tests are constant. Rationale for the noted difference remains to be found. Magnitudes of the bearing damping coefficients (C_{XX}, C_{YY}) increase slightly with load and shaft speed and are as much as 5.8±3.5 kN·s/m (34±20 lb_f·s/in). However, the total uncertainty of the damping coefficients is comparably high.

Recommendations regarding the use of gas bearings as rotating machinery supports include ensuring the resultant system has sufficient damping and simplifying installation (i.e. by improving alignment procedures). Research on gas bearings supplemented with external damping elements is useful to expand the range of machine types that benefit from the use of gas bearings. Note, the similarity in the bearing structure stiffness (K_U) and the bearing aerostatic stiffness (K_a) indicates that the bearing pad supports significantly influence the bearing performance. A useful

investigation is to determine safe surface speeds for various pad-operating clearances as a means to reduce assembly tolerances. Furthermore, upon installation in an actual machine, there may not be access to check pad lift with a dial indicator. Thus, the development of an alternative tool or procedure would be advantageous.

Acknowledgements

Thanks to the Turbomachinery Research Consortium and the U.S. Army Research Laboratory Research Associateship Program for financial support. Thanks to Jonathan Toner and Andy Alcantar for assisting with the experiments.

References

[1] Chen, W., Cheng K., Gao, Q., Lu, L., and Huo, D., 2019, "Aerostatic Bearings Design and Analysis with the Application to Precision Engineering: State-of-the-Art and Future Perspectives," *Tribology International*, **135**(2019), pp. 1-17.

[2] Lee, C., and You, H., 2009, "Characteristics of Externally Pressurized Porous Gas Bearings Considering Structure Permeability," *Tribology Transactions* **52**(6) pp. 768-776.

[3] Majumdar, B., 1975, "Analysis of Externally Pressurized Porous Gas Journal Bearings – I," *Wear*, **33**(1975), pp. 25-35.

[4] Rao, N., 1979, "Design of Externally Pressurized Porous Gas Bearings with Journal Rotation," *Wear*, **52**(1979), pp. 1-11.

[5] Su, J., and Lie, K., 2003, "Rotation Effects on Hybrid Air Journal Bearings," *Tribology International*, **36**(2003), pp. 717-726.

[6] Fourka, M., and Bonis, M., 1997, "Comparison Between Externally Pressurized Gas Thrust Bearings with Different Orifice and Porous Feeding Systems," *Wear*, **210**, pp. 311-317.

[7] Rasnick, W., Arehart, T., Littleton, D., and Steger., P., 1974, "Porous Graphite Air-Bearing Components as Applied to Machine Tools". Technical Report MRR74-02, Society of Manufacturing Engineers, Dearborn Michigan, pp. 1-41.

[8] Jacob, J., Yu, J., Bently, D., and Goldman, P., 2001, "Air-Hammer Instability of Externally Pressurized Compressible-Fluid Bearings," Technical Report, Bently Rotor Dynamics Research Corporation, Minden, Nevada, pp. 1-7.

[9] Shapiro, W., Decker, O., and Heller, S., 1971, "A Porous Hydrostatic Gas Bearing for Use in Miniature Turbomachinery", ASLE Transactions, **14**(*2*) pp. 144-155.

[10] Devitt, A., San Andrés, L., and Jeung, S., 2015, "Carbon-graphite Gas Bearings for Turbomachinery", *Proceedings of the 30th American Society for Precision Engineering Annual Meeting*, Austin, TX, November 1-6.

[11] American Petroleum Institute (API) Standard 617, 2002, "Axial and Centrifugal Compressors and Expander-Compressors for Petroleum, Chemical and Gas Industry Services," Seventh Edition. Chapter 1, pp. 12.

[12] San Andrés, L., Jeung, S., Rohmer, M., and Devitt, A., 2015, "Experimental Assessment of Drag and Rotordynamic Response for a Porous Type Gas Bearing," Extended Abstract, *STLE Annual Meeting and Exhibition*, Dallas, TX May 17-21, pp. 1-5.

[13] Zheng, Y., Cable, T., San Andrés, L., De Santiago, O., and Devitt, D., 2016, "Assessment of Porous Type Gas Bearings: Measurements of Bearing Performance and Rotor Vibrations," Proceedings of the ASME Turbo Expo, Seoul, South Korea, June 13-17, 2016, ASME Paper No. GT2016-57876

[14] Zheng, Y., and San Andrés, L., 2017, "A Computational Model for Tilting Pad Gas Bearings (Porous Type) and Performance Evaluation of a Carbon-Graphite Porous Type Thrust Seal", TRC-B&C-03-17, Annual Research Progress Report to the Texas A&M University Turbomachinery Research Consortium, May 31-June 2, 2017, College Station, TX, pp. 1-65.

[15] Feng, K., Wu, Y., Liu, W., Zhao, X., and Li, W., 2018, "Theoretical Investigation on Porous Tilting Pad Bearings Considering Tilting Pad Motion and Porous Material Restriction," *Precision Engineering*, **53**, pp. 26-37.

[16] Sunflex Metal Industries, 2019 "AISI 4140 Steel," Alloy Steel, https://www.sunflexmetal.net/alloy-steel-aisi-4140-steel-supplier-exporter/ (accessed November 22, 2019)

[17] Poco Graphite, 2015, *Properties and Characteristics of Graphite*, Decatur, TX, pp. 24 http://poco.com/Portals/0/Literature/Semiconductor/IND-109441-0115.pdf (accessed November 22, 2019)

[18] Kestin, J. and Whitelaw, J., 1964, "The Viscosity of Dry and Humid Air," *Int. J. Heat Mass Transfer*, **7**, pp. 1245-1255.

[19] Radigan, W., 2013, *Excel Belleville Spring Calculator*, Radigan Engineering, Albuquerque. https://radiganengineering.com/2013/11/excel-belleville-spring-calculator/, (accessed July 12, 2019).

[20] Schnorr Corporation, 2003, *Handbook for Disc Springs*, Hela Werbung, Heilbronn, Germany, pp. 11-22.

[21] Petele, M., 2003, *Springs*, MITCalc (Content), http://www.mitcalc.com/doc/springs/help/en/springs.htm, (accessed July 12, 2019).

[22] Childs, D., and Harris, J., 2009, "Static Performance Characteristics and Rotordynamics Coefficients for a Four-Pad Ball-in-Socket Tilting Pad Journal Bearing," *J. Eng. for Gas Turbines/Power*, **131**(6), pp. 1-11.

[23] Coghlan, D., 2014, "Static, Rotordynamic, and Thermal Characteristics of a Four Pad Spherical-Seat Tilting Pad Journal Bearing with Four Methods of Directed Lubrication," M.S. Thesis, Texas A&M University, College Station, TX, pp. 28.

[24] Lobontiu, N., 2010, *System Dynamics for Engineering Students: Concepts and Applications*, Academic Press, Burlington, MA, pp. 68, Chap. 3.

[25] Lund, J., 1968, "Calculation of Stiffness and Damping Properties of Gas Bearings," *J. Lubrication Technology*, **90**(4), pp. 793-803.

[26] Delgado, A., 2015, "Experimental Identification of Dynamic Force Coefficients for a 110 mm Compliantly Damped Hybrid Gas Bearing," Paper No. GTP-14-1526, *ASME J. Eng. Gas Turbines Power*, **137**(7), pp. 072502.

[27] Rouvas, C., and Childs, D., 1993, "A Parameter Identification Method for the Rotordynamic Coefficients of a High Reynolds Number Hydrostatic Bearing," *J. Vib. Acoust.*, **115**(3), pp. 264-270.

[28] Childs, D., and Hale, K., 1994, "A Test Apparatus and Facility to Identify the Rotordynamic Coefficients of High-Speed Hydrostatic Bearings," *J. Tribology*, **116**(2), pp.337-343.

[29] Waumans, T., Peirs, J., Reynaerts, D., and Al-Bender, F., 2011, "On the Dynamic Stability of High-Speed Gas Bearings: Stability Study and Experimental Validation," *Sustainable Construction and Design*, **2**(2), pp. 342-351.

[30] Crain, E., 1999, *Crain's Petrophysical Handbook*, published online at www.spec2000.net, Chap. 9: Core Permeability.

[31] Yoshimoto, S., Tozuka, H., Dambara, S., 2003, "Static Characteristics of Aerostatic Porous Journal Bearings with a Surface-Restricted Layer," *Journal of Engineering Tribology*, **217**(2), pp. 125-132.

[32] Aalborg, 2018, "Operating Manual: GFM Mass Flow Meters", Technical Data Sheet TD9411M, pg. 5.

[33] Niemczyk, M., Bolen, R., Private Conversation, 10/16/19.

[34] Yoshimoto, S., Kohno, K., 2001, "Static and Dynamic Characteristics of Aerostatic Circular Porous Thrust Bearings (Effect of the Shape of the Air Supply Area)," *Journal of Tribology*, **123**(3), pp. 501-508.

[35] Majumdar, B., Saha, N., 2002, "Study of Externally-Pressurized Gas-Lubricated Two-Layered Porous Journal Bearings: A Steady State Analysis," *Journal of Engineering Tribology*, **216**(2), pp. 151-158.

[36] Otsu, Y., Miyatake, M., Yoshimoto, S., 2011, "Dynamic Characteristics of Aerostatic Porous Journal Bearings with a Surface Restricted Layer," *Journal of Tribology*, **133**(1), pp.125-132.

[37] San Andrés, L., Cable, T., Zheng, Y., De Santiago, O., and Devitt, D., 2016, "Assessment of Porous Type Gas Bearings: Measurements of Bearing Performance and Rotor Vibrations," ASME Paper GT2016-57876, *Proceedings of ASME Turbo Expo 2016*, June 13-17, Seoul, South Korea, pp.1-34.

[38] Kreyszig, E., 2011, *Advanced Engineering Mathematics*, Wiley, Hoboken, NJ, pp. 1107, Chap. 25-9.

[39] Kreyszig, E., 2011, *Advanced Engineering Mathematics*, Wiley, Hoboken, NJ, pp. 1071, Chap. 25-3.

Appendix A: Experimental Estimation of Pad Permeability Coefficient

Hydrostatic gas bearings typically use orifices or a porous material to regulate the flow of the lubricant supplied to the rotor-bearing clearance. For porous-type restrictors, the material permeability affects the pressure of the fluid supplied to the bearing radial clearance.

Darcy's law relates the volumetric flowrate (Q) of the gas through a porous layer of thickness (t_p) to the difference in entrance (P_S) and exit (P_a) pressures, the fluid viscosity (μ_S), and the area (A) normal to the direction of flow [30].

$$Q = \frac{\kappa\, A\, (P_S - P_a)}{\mu_S\, t_p} \qquad \text{[A-1]}$$

where (κ) is a permeability coefficient.

Reference [9] illustrates the importance of this information with an example where an overestimation of the permeability coefficient (κ) for a porous pad-type restrictor material required design modifications of the pad to generate sufficient hydrostatic pressure to lift the rotor. Further, a permeability coefficient (κ) determined from experiments provides boundary conditions for numerical models [15]. Thus, this appendix records a practical method for empirically determined permeability coefficients and results for the test bearing porous carbon-graphite pads.

Measurements of the flowrate entering the pad and the supply air pressure enable estimation of the pad material permeability. Table A-1 lists the instrument models and measurement error for the experiment.

Table A-1: Instrument Models and Capabilities

Measured Value	Instrument	Measurement (Equivalent) Error
Supply Pressure	Bourdon Pressure Gauge	±0.14 bara
Flowrate[20]	Aalborg GFM37(1)	±0.5 SLPM
Lengths	Caliper	±25 µm

Figure A-1 shows the air supply system to a pad, and Figure A-2 shows another view of the overall setup.

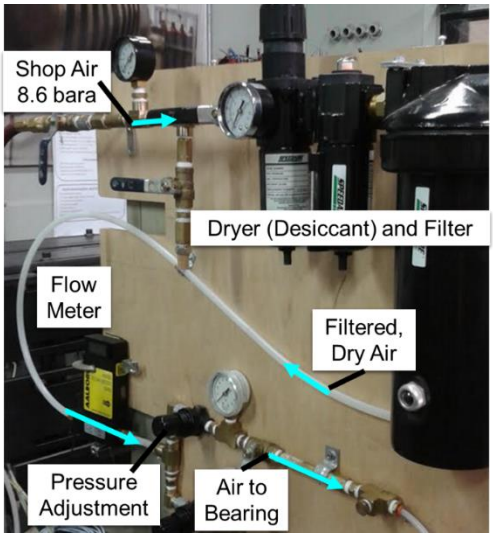

Figure A-1: Air supply to porous pad for permeability experiment

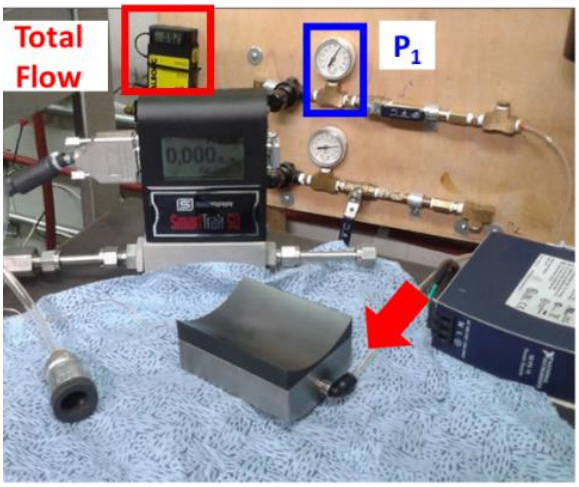

Figure A-2: Pad permeability experimental setup for measuring inlet air flowrate (red box) and supply pressure (blue box)

The thickness (t_p) of a porous pad for the test bearing herein is not constant. Figure A-3 shows an equivalent thickness representing the sample of interest and labels the fluid inlet (*S*) and exit (*2*) surfaces. The maximum and minimum thickness are 15.24 mm and 5.08 mm, respectively.

[20] This mass flowmeter relates the heat transfer of the flowing gas to a sensor circuit resistance and outputs volumetric flowrate in standard conditions [32]. Converting from flowmeter outputs to mass flowrates requires only multiplying the result by the standard density. The standard density is the standard pressure divided by the product of the standard temperature and gas constant. Aalborg instruments define standard conditions as 21.1° C (70° F) and 101.3 kPa (14.7 psia), reporting flow in LPM relative to these conditions [33]. SLPM(1) denotes the raw mass flowmeter output units to avoid confusion with SLPM, which refers to different standard conditions.

The cross section area of the porous carbon layer in Figure A-3 is 507.80 mm^2. The equivalent pad thickness (t_p) is the pad cross section area divided by the pad width (w) and equals 8.33 mm.

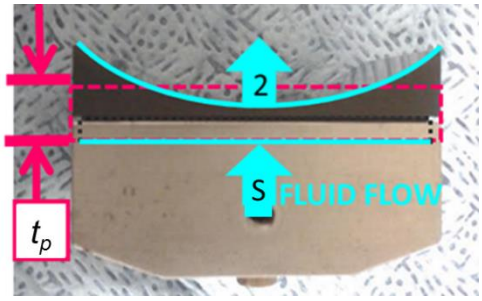

Figure A-3: Equivalent thickness over entire pad width for recessed porous pad with fluid inlet (*S*) and exit (*2*) surfaces

Figure A-4 shows the air flowrate supplied to a bearing pad vs. gauge supply pressure (P_S-P_a) for four pads.

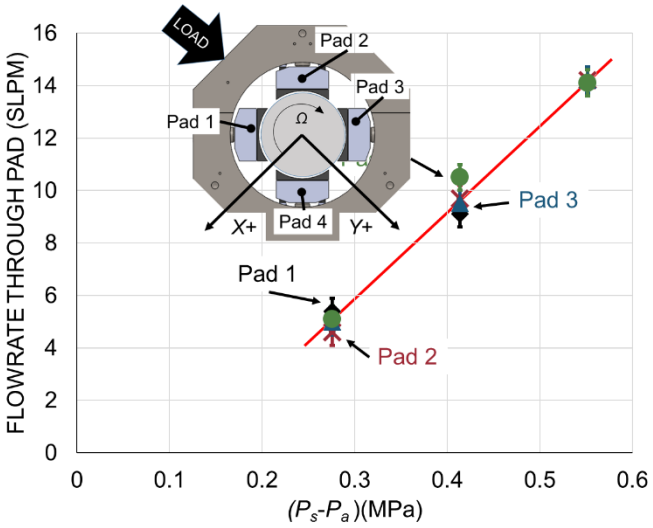

Figure A-4: Measured supply air flowrate vs. gauge pressure measurements for four pads.

Table A-2 lists the measured air flowrates supplied to each bearing pad (separately) with the supply air at a fixed pressure.

Table A-2: Recorded gas flowrates (SLPM(1)) for four pads supplied at 3.7, 5.1 and 6.4 bara supply pressures

	SUPPLY PRESSURE	FLOWRATE
	[bara]	[SLPM(1)}
PAD 1	3.7±0.14	5.4±0.5
PAD 2		4.6±0.5
PAD 3		5.0±0.5
PAD 4		5.1±0.5
PAD 1	5.1±0.14	9.1±0.5
PAD 2		9.7±0.5
PAD 3		9.5±0.5
PAD 4		10.5±0.5
PAD 1	6.4±0.14	14.1±0.5
PAD 2		14.2±0.5
PAD 3		14.2±0.5
PAD 4		14.1±0.5

The pad permeability estimates from the exit flowrate (Q_2) and supply pressure (P_S) measurements as

$$\kappa = \frac{2\, Q_2\, \mu\, t_p\, P_a}{A\, (P_S^2 - P_a^2)} \qquad \text{[A-2]}$$

At a temperature of 21°C, the assumed air viscosity (μ) is 1.79×10^{-5} Pa·s and the exit pressure (P_a) is 101.3 kPa. The pad surface area ($A=R_{PAD}\cdot\Theta_P\cdot L$) is 0.005 m^2.

Figure A-5 shows the permeability coefficients for four porous carbon pads from the measurements of supply air flowrate and pressure, with an average permeability of $\kappa=3.7\pm0.2\times10^{-15}$ m^2.

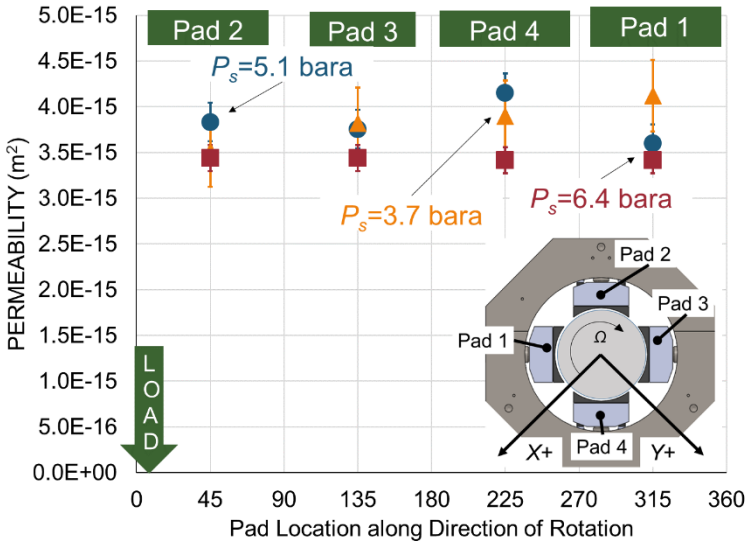

Figure A-5: Estimated pads permeability (*κ*) from flow measurements for porous carbon pads versus pad location during operation relative to static load.

Reference [9] notes that the random nature of the pore distribution leads to significant variations in the permeability of graphite blanks, even for blanks purchased from the same manufacturer. Published permeability coefficients for porous graphite used in gas bearings span 10^{-12} to 10^{-16} m^2. Table A-3 summarizes experimentally determined permeability coefficients, with the reference and publishing year for comparison to the results from this work.

Table A-3: Published permeability coefficients for comparison to those from this work

Permeability Coefficient, κ	Year	Reference
$10^{-12} - 10^{-14}$	1997	[6]
6.6×10^{-15} m^2, 9.2×10^{-15} m^2	2001	[34]
3.1×10^{-15} to 8.4×10^{-15}	2002	[35]
4.3×10^{-15} m^2	2003	[31]
6.5×10^{-16} m^2	2011	[36]
1.2×10^{-15} m^2	2016	[37]
2.85×10^{-15} m^2	2017	[14]
$3.7\pm0.2\times10^{-15}$ m^2	2019	Current Work

The most recent permeability coefficient reported is from Ref. [14] for a gas bearing with five carbon graphite pads and is 23% smaller than the average permeability of the test bearing pads herein. Note also that the permeability coefficient of the test bearing is similar to that found by Yoshimoto et. al. in 2003 for a porous Carbon graphite bushing [31]. The spread of the results indicates the importance of experimental verification for quality control and realistic modeling.

Appendix B: Experiment to Determine Baseline Stiffness, K_b

It is necessary to identify the stiffness of the bearing attachments to distinguish the stiffness of the bearing assembly from the attachment mechanisms (e.g. pitch stabilizers). Figure B-1 shows the setup to meet this objective. The bearing installs in Rig 2. However, this time, the pads are affixed to the housing exterior to preserve the total assembly weight without pad-rotor contact restricting housing movement. The rotor is stationary as the shaker heads excite the housing along the *X* direction, and then along the *Y* direction.

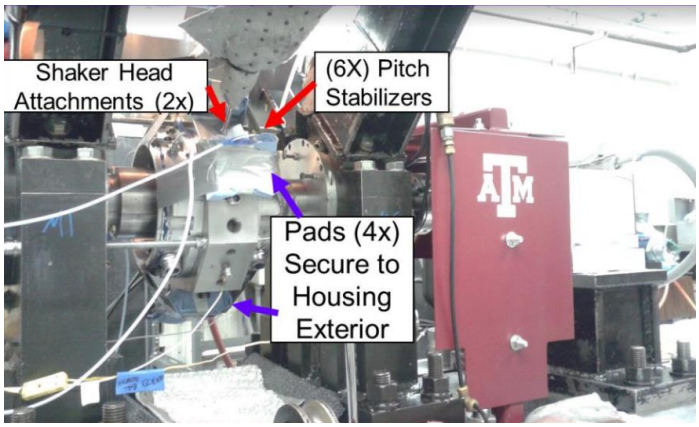

Figure B-1: Modified setup in Rig 2 to conduct baseline shakes and to determine the structure stiffness

The dynamic stiffness uses measurements where the acceleration and displacement coherences with respect to the applied load are equal to or higher than 0.9. Figure B-2 shows the real component of the baseline dynamic stiffness and Figure B-3 shows the imaginary component. The magnitudes are small, but $\text{Im}(H)_b$ is similar in magnitude to that of the bearing[21] $\text{Im}(H)$ for shaft speed = 6 krpm (100 Hz). This means that the quadrature stiffness of the rig is comparable to the quadrature stiffness of the bearing at that excitation frequency.

[21] Does not include the baseline $\text{Im}(H)_b$

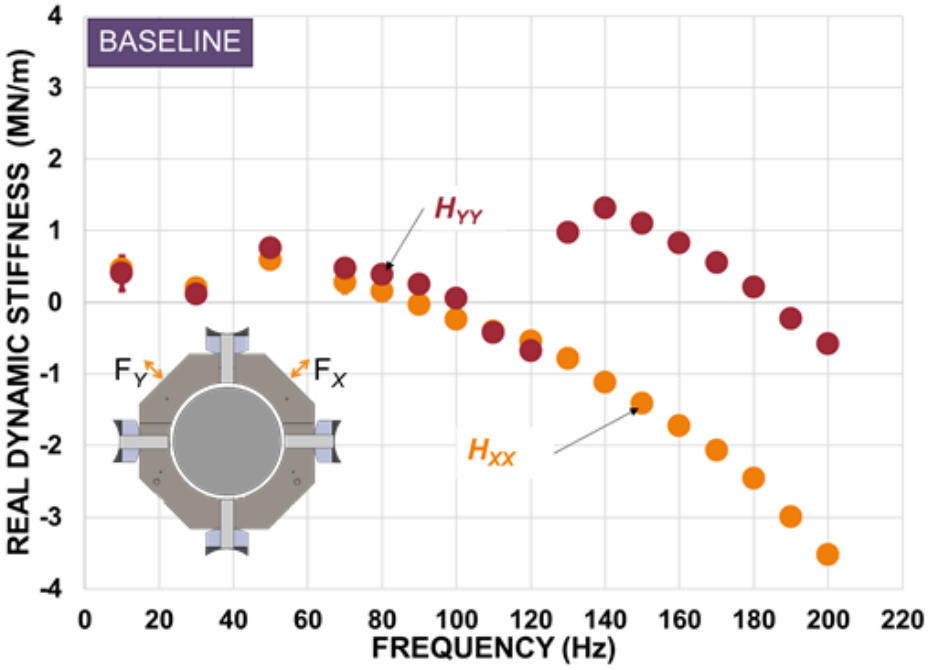

Figure B-2: Real part of baseline dynamic stiffness

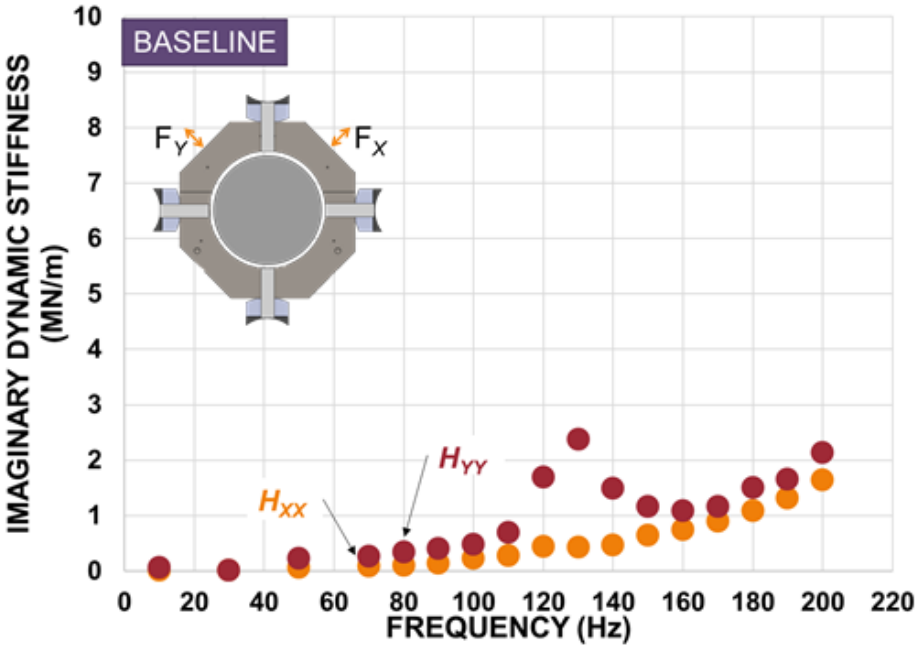

Figure B-3: Imaginary part of baseline dynamic stiffness

The results of a static load test are comparable to the low frequency real components of the baseline dynamic stiffness. Figure B-4 shows the measurement of applied load vs. direct displacement along the *X* and *Y* directions. The measurements indicate the lateral stiffnesses (K_{YY}^{b}=0.49 MN/m, K_{XX}^{b}=0.47 MN/m) of the pitch stabilizers is very low compared to the bearing stiffness. Therefore, the pitch stabilizers do not significantly affect the bearing stiffness from measurements of applied load and housing displacement. Nevertheless, the bearing stiffnesses reported from the static load tests do not include the pitch stabilizer stiffness.

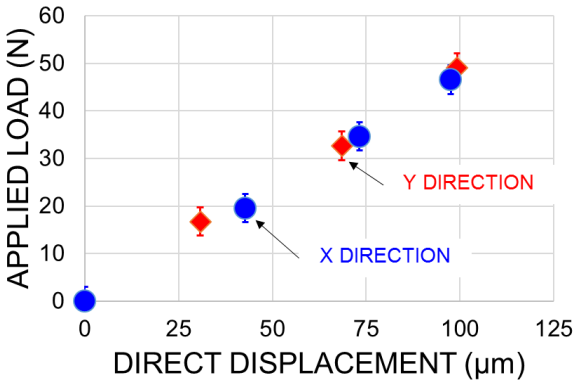

Figure B-4: Measurements of applied load vs. housing displacement (pads affixed to housing exterior to prevent contact with rotor) to determine effect of pitch stabilizer stiffness (K_b) on Rig 2 data, no shaft speed.

Appendix C: Cross Coupled Dynamic Stiffness

Figures C-1 and C-2 show the real part of the dynamic cross-coupled stiffnesses (H_{XX}, H_{YY}) for the system vs. excitation frequency for operation at 6 krpm and 9 krpm, respectively. The magnitudes of H_{XY} and H_{YX} are very small. When the sign of Re(H_{XY}) is opposite that of Re(H_{YX}) the resultant cross-coupled forces are destabilizing. Although they are similar in magnitude to Im(H_{XX}) and Im(H_{YY}) the coherence of Re(H_{XY}) and Re(H_{YX}) is much poorer.

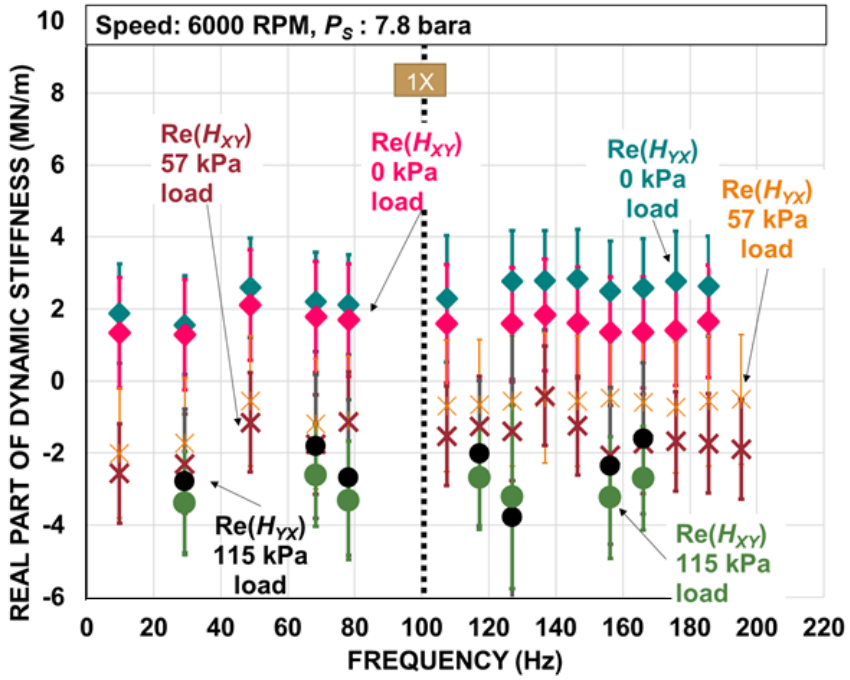

Figure C-1: Real part of cross-coupled dynamic stiffnesses (H_{XY}, H_{YX}) vs. excitation frequency. Operation at shaft speed = 6 krpm and static specific loads = 0 kPa, 57 kPa and 115 kPa (P_S = 7.8 bara).

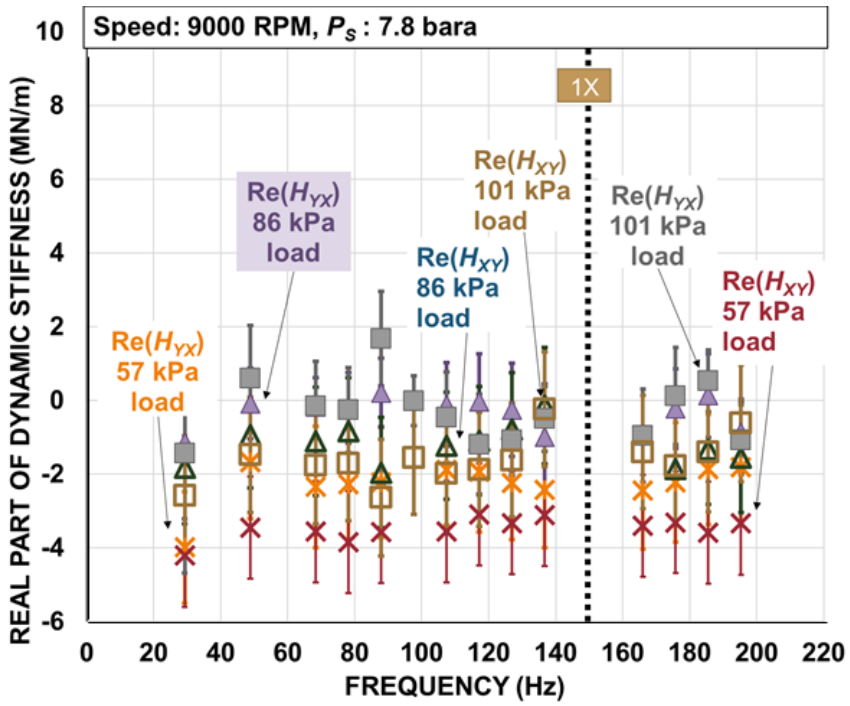

Figure C-2: Real part of cross-coupled dynamic stiffnesses (H_{XY}, H_{YX}) vs. excitation frequency. Operation at shaft speed = 9 krpm and static specific loads = 57 kPa, 86 kPa and 101 kPa (P_S = 7.8 bara).

As an example, Figures C-3 and C-4 plot the coherence magnitudes comparing the excitation force to the cross-coupled bearing acceleration vs. excitation frequency for operation at 9 krpm with 86 kPa static load. The bearing dynamic load experiment results show low coherence (less than 0.9) amongst the off-diagonal terms (F_{XY}, a_{XY}, D_{XY}), (F_{YX}, a_{YX}, D_{YX}) for most of the subsynchronous excitation frequencies.

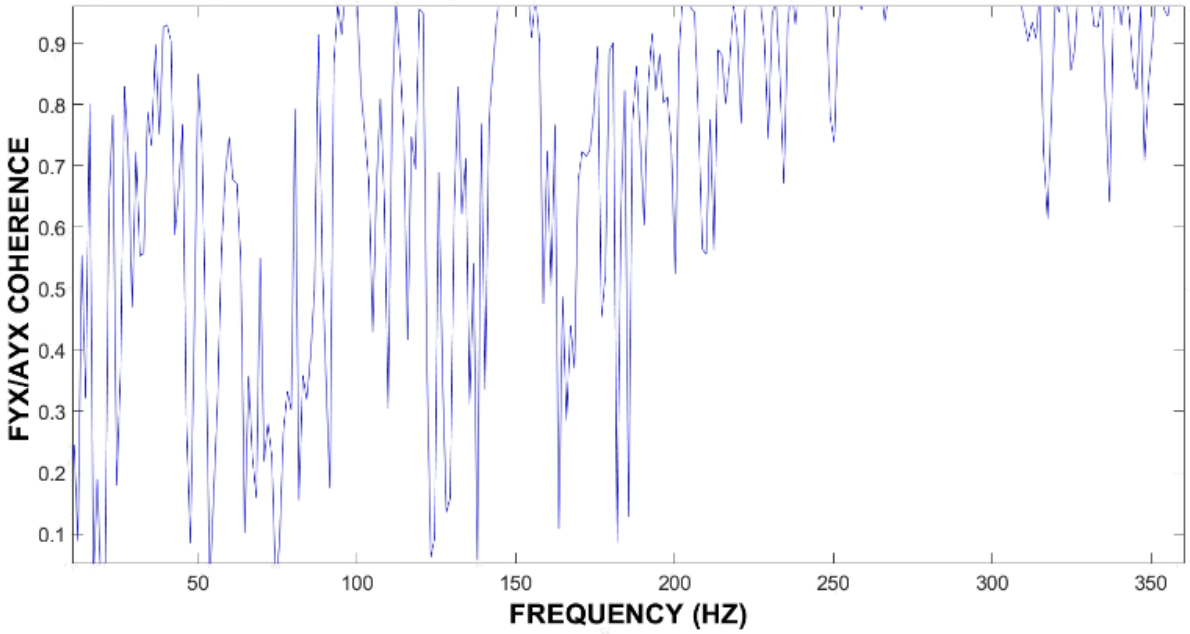

Figure C-3: Coherence magnitude vs. excitation frequency for cross coupled dynamic stiffness *Hyx* for operation at 9 krpm (150 Hz) and 86 kPa static load.

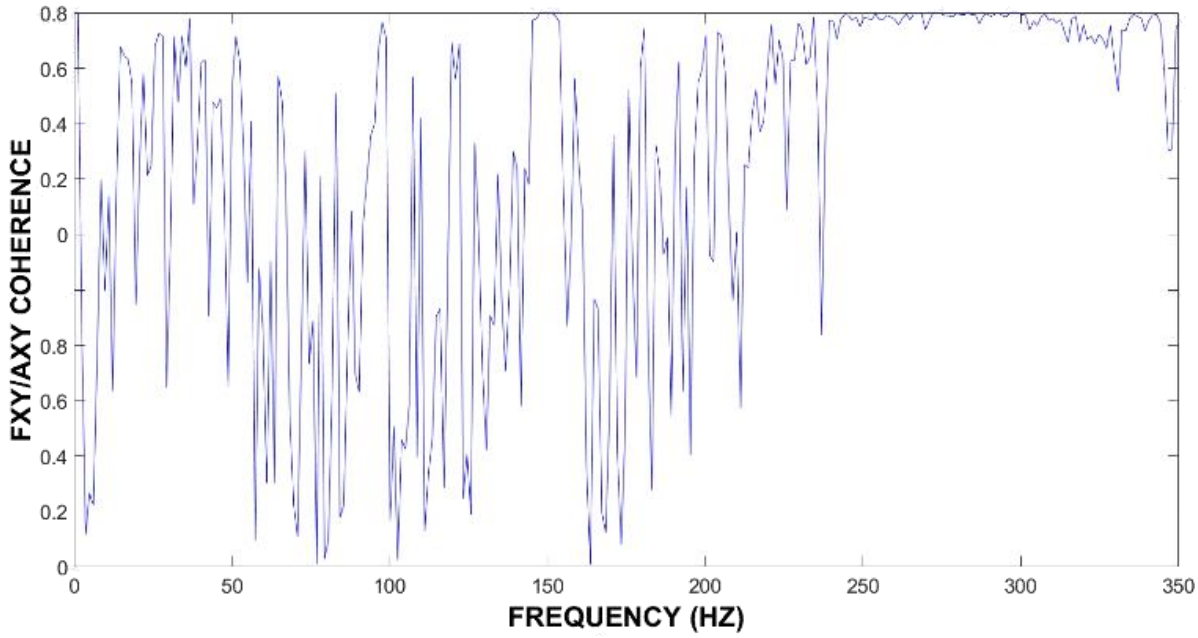

Figure C-4: Coherence magnitude vs. excitation frequency for cross coupled dynamic stiffness *Hxy* for operation at 9 krpm (150 Hz) and 86 kPa static load.

Appendix D: Uncertainty Analyses

Uncertainties of Belleville Washer Stiffness (K_{SP}), Pivot Stiffness (K_P), Bearing Structural Stiffness (K_U) and Bearing Stiffness (K) from Static Load Tests in Report Chapters 1-4

The equations and procedure to determine the uncertainty of the stiffnesses (load and unload) from the static load test data follow from Ref. [38]. The estimates for Belleville washer stiffness (K_{SP}), pivot stiffness (K_P), bearing structural stiffness (K_U) and bearing stiffness (K) are from measurements of applied static force (F) and bearing displacement (D). The least squares method determines a stiffness as the most probable slope of a line (F^*=-K·D) fitting the force and displacement data, consisting of n points.

$$K = \frac{\sum_{i=1}^{n} D_i F_i - \frac{1}{n}\sum_{i=1}^{n} D_i \sum_{i=1}^{n} F_i}{\sum_{i=1}^{n} D_i^2 - \frac{1}{n}(\sum_{i=1}^{n} D_i)^2} \qquad \text{[D-1]}$$

The slope estimate is windowed by a 95% confidence interval that is given by

$$(K - U_K) \leq K \leq (K + U_K) \qquad \text{[D-2]}$$

where the standard error U_K of the slope of the trend line fitting n measurements of D and F, (with $\bar{z}$ symbolizing the sample mean of variable z) calculates as

$$U_K = \lambda \sqrt{\frac{\frac{1}{n-2}(\sum_{i=1}^{n}(F_i - \bar{F})^2)^2}{\sum_{i=1}^{n}(D_i - \bar{D})^2}} \qquad \text{[D-3]}$$

and λ from a t-distribution table corresponding to n-2 degrees of freedom, where n is the number of samples.

Bias Error in Bearing Dynamic Stiffness (H_{XX} and H_{YY})

Table D-1 lists the instrument and corresponding measurement accuracy for the measurements used to determine the bearing dynamic stiffness.

Table D-1: Dynamic load test instrument model and measurement accuracy

	Instrument Model	Measurement Accuracy
Excitation force, U_F	Strain gauge load cell (Xcite® 2522)	$\pm$5 N
Housing displacement relative to rotor, U_D	Eddy current sensors (Bentley Nevada® 3300 series)	$\pm$1 μm
Baseline mass, U_M	Scale	$\pm$0.1 kg
Housing acceleration, U_a	Piezoelectric accelerometers (PCB® 352C33)	$\pm$0.01 g

The bias error (β_H) in the bearing dynamic stiffness (H) is

$$\beta_H = \left(\left(\frac{\partial H}{\partial F} U_F \right)^2 + \left(\frac{\partial H}{\partial M} U_M \right)^2 + \left(\frac{\partial H}{\partial a} U_a \right)^2 + \left(\frac{\partial H}{\partial D} U_D \right)^2 \right)^{0.5} \quad [D\text{-}4]$$

where

$$\left(\frac{\partial H}{\partial F} = \frac{1}{D} \right), \ \left(\frac{\partial H}{\partial M} = -\frac{a}{D} \right), \ \left(\frac{\partial H}{\partial a} = -\frac{M}{D} \right) \text{ and } \left(\frac{\partial H}{\partial D} = \frac{(-F + Ma)}{D^2} \right) \quad [D\text{-}5]$$

Equation (D-4) evaluated is

$$\beta_H = \left(\left(\frac{1}{D} U_F \right)^2 + \left(\frac{-a}{D} U_M \right)^2 + \left(\frac{-M}{D} U_a \right)^2 + \left(\frac{Ma - F}{D^2} U_D \right)^2 \right)^{0.5} \quad [D\text{-}6]$$

The bias error (β_H generally ~1 MN/m) calculated with Equation (D-6) dominates the total uncertainty of the dynamic stiffness (H) for the gas bearing experiments. Results in Chapter 5 showed the magnitude of the imaginary part of the bearing dynamic stiffness (H) is small (also on the order of 1 MN/m) to measure using Rig 2 outfitted with the instruments listed in Table D-1. Reducing the bias error to ~0.3 MN/m improves the accuracy particularly of the imaginary component of the dynamic stiffness (influencing the damping coefficient). Hence, this section

identifies the modifications to Rig 2 required to reduce the bias error to better characterize gas bearings.

Figure D-1 shows the effect of each measurement error on the bearing dynamic stiffness bias error (β_H) for the current measurement accuracy and for two instrumentation upgrades. With the current instrumentation, the primary contributor $\left(\frac{\partial H}{\partial F} U_F\right)$ to the bias error is the load cell measuring the applied dynamic force, and the secondary contributor $\left(\frac{\partial H}{\partial a} U_a\right)$ is the accelerometer measuring the bearing acceleration. It is important to note that the applied dynamic loads, bearing accelerations and bearing displacements are an order of magnitude less than those used to conduct a dynamic load test on an oil bearing with Rig 2. Thus, some of the gas bearing dynamic load test instrumentation does not require as large a full scale output but does require higher accuracy.

Table D-2 lists the instrumentation changes for two solutions to reduce the bias error. Solution A reduces the error in the load cell measurement, which reduces the bias error by ~39%. Solution B achieves a more satisfactory reduction in error (~69%) by reducing the error in both the load cell measurement and the accelerometer measurement. For Solution B, the displacement measurement becomes the primary source of error. Further reducing the bias error beyond the improvements offered in Solution B requires a more accurate displacement measurement than eddy current sensors, and it could become challenging to distinguish the bearing motion from the surface roughness of the rotor. Thus, Solution B offers a significant reduction in bias error achievable via practical accuracy requirements for two instruments (Table D-2).

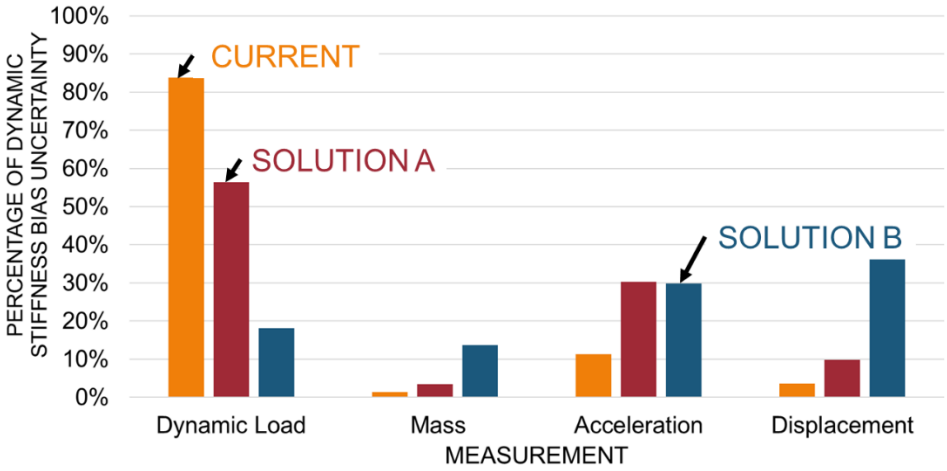

Figure D-1: Measurement uncertainty effect on bias error of Rig 2

Table D-2: Instrumentation accuracy required for Solutions A and B with reduction in dynamic bearing stiffness bias error (relative to bias error using Rig 2 current instrumentation).

	Load Cell Accuracy Requirement	Accelerometer Accuracy Requirement	Reduction in Bias Error (%)
Solution A	±0.76N	0.01 g	39%
Solution B	±0.76 N	0.005 g	69%

Figure D-2 shows the improvements Solutions A and B offer in reducing the current dynamic stiffness bias error.

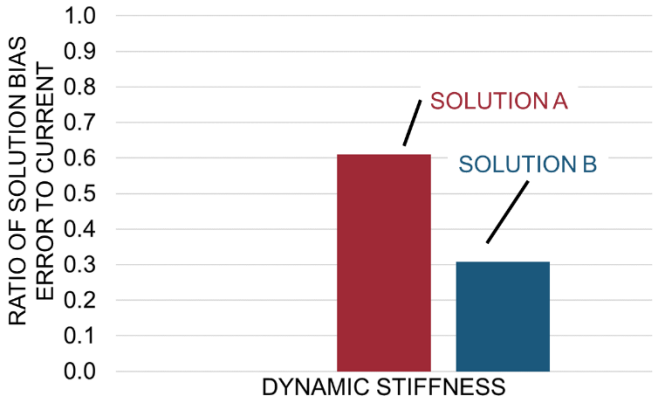

Figure D-2: Ratio of solution dynamic stiffness bias error to current dynamic stiffness bias error for Solutions A and B

Uncertainty of Bearing Stiffness Coefficient (*K*) from Dynamic Load Tests

The bearing stiffness (*K*) for a given speed and static load combination, is the average of the real components of the dynamic stiffness for excitation frequencies up to just above

synchronous speed. The limits (Γ_K) of a 95% confidence interval for *K* quantify the precision error and evaluate from the solution (λ) from a t-distribution table (for *n*-1 degrees of freedom), the corresponding sample variance (*s*) and the number of samples, *n* [39].

$$\Gamma_{K,dynamic} = \lambda \frac{s}{\sqrt{n}} \qquad \text{[D-7]}$$

The total uncertainty combines the bias error with the precision error (95% confidence intervals) as

$$U_{K,dynamic} = \sqrt{{\Gamma_K}^2 + {\beta_H}^2} \qquad \text{[D-8]}$$

Table D-3 lists the stiffness coefficient from the dynamic load data, the number of points used to calculate *K* and the total uncertainty. In general, the uncertainty magnitudes for *K* are acceptable.

Table D-3: Uncertainty (U_K) in the bearing stiffness coefficients as the average of the real components Re(*H*) of the dynamic bearing stiffness

Speed	Specific Load	Frequency Range		K_{XX}	K_{YY}	Number of Points Used	U_{KXX}	U_{KYY}
(RPM)	(kPa)	(Hz)	(Hz)	(MN/m)	(MN/m)		(MN/m)	(MN/m)
0	0	29.3	156.3	16.4	15.1	12	1.5	1.8
6000	0	9.8	107.4	14.3	13.6	6	1.0	1.0
	57	9.8	107.4	22.7	21.9	6	1.1	1.1
	115	29.3	107.4	31.2	31.5	5	6.9	1.6
9000	57	29.3	166.0	21.4	20.7	10	1.3	1.2
	86	29.3	175.8	29.0	27.6	10	1.3	1.4
	101	29.3	166.0	32.7	30.8	11	1.5	1.4

Uncertainty of Bearing Damping Coefficient (C) from Dynamic Load Tests

The imaginary components of the bearing dynamic stiffness increase with excitation frequency. The bearing damping coefficient (*C*) for a given speed and static load combination, is

the slope of the line fitting the data (Im(H) vs. excitation frequency ω) to excitation frequencies just above synchronous using the least squares method.

$$C = \frac{\sum_{i=1}^{n} Im(H)_i \omega_i - \frac{1}{n}\sum_{i=1}^{n}\omega_i \sum_{i=1}^{n} Im(H)_i}{\sum_{i=1}^{n}\omega_i^2 - \frac{1}{n}(\sum_{i=1}^{n}\omega_i)^2} \quad \text{[D-9]}$$

The limits (Γ_C) of a 95% confidence interval for a C (calculated from n samples) is the product of the solution (λ) from a t-distribution table (for n-2 degrees of freedom) and the slope standard deviation (s_C). Γ_C quantifies the precision error for C.

$$s_C = \sqrt{\frac{S_{yx}^2}{S_{xx}}} = \sqrt{\frac{\frac{1}{n-2}\left(\sum_{i=1}^{n}\left(Im(H)_i - \overline{Im(H)}\right)^2\right)^2}{\sum_{i=1}^{n}(\omega_i - \bar{\omega})^2}} \quad \text{[D-10]}$$

$$\Gamma_C = \lambda \cdot s_C \quad \text{[D-11]}$$

The bias error (β_C) for the damping coefficient is half the difference in the maximum and minimum slopes of the trend line fitting the Im(H) vs. ω data.

The total uncertainty (U_C) of the damping coefficient combines the bias error with the 95% confidence intervals as

$$U_C = \sqrt{{\Gamma_C}^2 + {\beta_C}^2} \quad \text{[D-12]}$$

Table D-4 lists U_C for the bearing damping coefficients determined from the dynamic load experiments. The bias error dominates the total uncertainty of the damping coefficient. The damping coefficients are not quantifiable from the measurements at 6 krpm operating speed.

Table D-4: Uncertainty (U_C) in the bearing damping coefficients as the slope of the imaginary components Im(H) of the dynamic bearing stiffness

Speed	Specific Load	Frequency Range		C_{XX}	C_{YY}	Number of Points Used	U_{CXX}	U_{CYY}
(RPM)	(kPa)	(Hz)	(Hz)	(kN·s/m)	(kN·s/m)		(kN·s/m)	(kN·s/m)
0	0	29.3	156.3	1.3	0.9	12	3.8	4.1
6000	0	9.8	107.4	1.7	2.0	6	4.1	3.0
	57	9.8	107.4	2.7	2.8	6	3.4	3.3
	115	29.3	107.4	1.9	3.0	5	6.8	4.5
9000	57	29.3	166.0	5.2	4.0	10	2.6	2.9
	86	29.3	175.8	5.0	4.3	10	2.7	3.4
	101	29.3	166.0	5.8	5.6	11	3.5	4.5

Appendix E: Static Load Test to Determine Bearing Structure Stiffness Following Dynamic Load Tests

The test bearing underwent a static load test the day after undergoing dynamic load tests to determine whether the load orientation[22] affected the stiffness of the bearing structure (no pad supply air, stationary rotor, $T \approx 21°C$). Aligning the load with the pad and pivot was an attempt to reduce the slight mechanical hysteresis in the results due to offset loading.

The test hydrostatic TPJB was not reconfigurable to apply loads directly through the pivot supports to determine the assembly pivot stiffness. However, applying equal loads ($F_X = F_Y$) along the X and Y directions (45^0) simulated a load-on-pad condition. The load (F_{LOP}) is simply

$$F_{LOP} = \sqrt{F_X^2 + F_Y^2} \qquad \text{[E-1]}$$

and the housing displacement (D_{LOP}) is

$$D_{LOP} = \sqrt{D_X^2 + D_Y^2} \qquad \text{[E-2]}$$

where D_X and D_Y are the average (drive end and non-drive end) housing displacement measurements along the X and Y directions respectively.

During this experiment, the pads are at room temperature and not supplied with pressurized air. Figure E-1 shows the applied load (F_{LOP}) on Pad 2 (refer to Figure 17 for numbering scheme) vs. the housing direct displacement (D_{LOP}) for both an increasing and a decreasing load.

[22] Previous use of the test rig to characterize oil bearings determined the pivot stiffness of a TPJB by reconfiguring the test bearing to apply a static load on a pad (LOP) instead of applying the load between pads (LBP) [23].

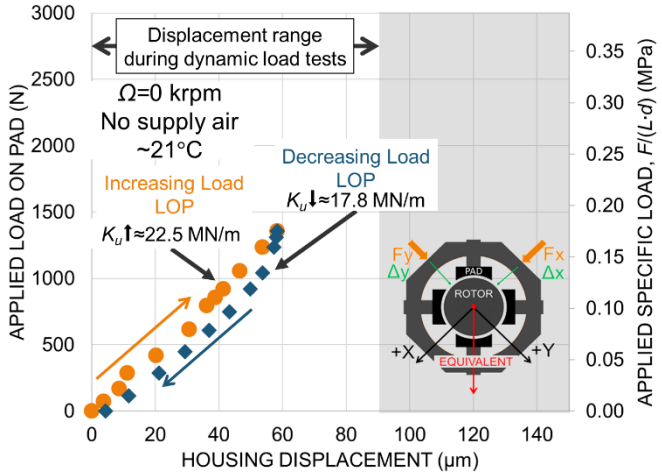

Figure E-1: Applied load (LOP) on bearing vs. housing displacement for increasing and decreasing loads. No shaft speed, no supply air, room temperature pads.

A linear regression fits the load vs. deflection data in Figure E-1 for housing displacements from 0 μm to 53 μm. The slope of the line estimates the stiffness of the bearing under increasing load as 22.5±0.7 MN/m. The same method applies to the decreasing load data for housing displacements from 53 μm to 0 μm. The bearing stiffness under decreasing load is 17.8±1.5 MN/m.

The LOP bearing structural stiffness (T≈21˚C) estimates are higher than those for the bearing in the LBP orientation at room temperature in Chapter 2. For increasing load, the stiffness of the bearing in the LOP orientation is similar to that of the pivot subassembly. Moreover, the LOP experiment results show an increase in mechanical hysteresis, compared to the results in Chapter 2. The average load ratio for the LOP test (F_X/F_Y) is 1.0, but the average displacement ratio (D_X/D_Y) is 0.8. This indicates that during the LOP test, the housing displacement was offset the load line by an angle of about 6˚.

Table E-1 lists the bearing structure stiffness under increasing and decreasing load calculated from the LOP equivalent applied force and housing displacements, from the X direction

data and from the *Y* direction data. The results show that the bearing structure stiffness is independent of the applied load orientation.

Table E-1: Bearing structure stiffness (K_U) after test with speed and dynamic loads

	from F_{LOP} and D_{LOP}	from F_X and D_X	from F_Y and D_Y
$K_U\uparrow$ (MN/m)	22.5±0.7	23.2±1.0	21.8±0.4
$K_U\downarrow$ (MN/m)	17.8±1.5	19.6±1.1	16.4±2.0